Tailoring III-nitrides and 2D boron nitride semiconductors for next generation of optoelectronic devices.

Suresh Sundaram

Memoire pour l'obtention du diplôme d'habilitation à diriger des recherches

Tailoring III-nitrides and 2D boron nitride semiconductors for next generation of optoelectronic devices.

Presenté par

Dr. Suresh Sundaram

Georgia Tech Europe et GT-CNRS-IRL2958

Ecole doctorale: Chimie-Mécanique-Materiaux-Physique

Université de Lorraine

Memoire Soutenue publiquement à Metz devant le jury composé de

Prof. Eva Monroy	INAC/SP2M, CEA Grenoble	Reporter
Prof. Maria Tchernycheva	Directrice, C2N-CNRS, Palaiseau	Reporter
Prof. Guillaume Cassabois	Professeur, Université de Montpellier	Reporter
Prof. Bernard Gil	Professeur, Université de Montpellier	Examiner
Prof. Dave Rogers	Founder & Director, Nanovation	Examiner
Prof. Germano Montemezzani	Professeur, Université de Lorraine	President & Examiner
Prof. Jean Paul Salvestrini	Director, IRL2958 Georgia Tech-CNRS	Examiner
Prof. Abdallah Ougazzaden	Professeur, Georgia Tech, USA	Parrain & Examiner

6 Décembre 2022

INDEX

1. Introduction

Consolidating more than a decade of research in a few tens of pages is a delicate exercise that requires choices. I have decided to present in this dissertation a summary of my research activities between August 2010 and July 2021 since completion of my PhD thesis. During this period, in addition to conventional heteroepitaxy I have gained considerable expertise on new and emerging metal organic vapor phase epitaxy (*MOVPE) epitaxial growth technologies such as selective area growth, nanoheteroepitaxy and van der Waals epitaxy. This manuscript describes the important results that contributed to a better understanding of these growth technologies and the evolution of related materials. The purpose of this first chapter is to provide to the reader a framework for my nitrides research and an explanation of the value of MOVPE growth for this type of material. Following that, I will justify the choices made regarding the contents of this document and its organization.*

1.1. Motivation and background

Modern semiconductor devices are sub-microscopic technologies that have driven many of the past few decades of developments. At present, they are utilized in nearly all aspects of modern technologies from lighting to communication, computing, transportation and artificial intelligence (AI). Previous decades were solely dominated by silicon. Silicon is not the highest-performing transistor material known to mankind, but we use silicon because it's affordable, easy to work with, and doesn't have any enormous flaws that limit its usefulness in any particular application.

Silicon has almost reached its fundamental limits in terms of range of operation and functionality. Importantly, because of its indirect bandgap silicon is not an efficient

light emitter and hence, is not used in optoelectronics as an active material. However, III-V compound semiconductors have a direct bandgap and are widely used in the manufacture of devices such as microwave frequency integrated circuits, monolithic microwave integrated circuits, infrared light-emitting diodes, laser diodes, solar cells and optical windows [Mos87].

Natural evolution of this class of elemental and compound semiconductors is nitride-based compound semiconductors. This class of materials has extended the use of semiconductors, for example, solid state lighting (blue, green and white LEDs and lasers), new communications spectra and adoption of renewable power sources. Although 95% of the market is still dominated by elemental and III-V semiconductor technologies, the nitride-based semiconductor market is quickly growing. We rely on this class of compound semiconductors for comfort, speed, safety and sustainability.

Considering the needs of not only the current but also of the next generation, the growth of this new semiconductor domain is set to revolutionize the future with better smart functionalities and energy saving solutions. For example, as the elemental transistor size shrinks down with Moore's law hitting the fundamental quantum limit, as shown in the figure 1, the industry seeks a complete change of paradigm. The most radical idea is to use quantum-mechanical phenomena, where information is transported using the wave nature of matter, such as interference and coherence effects, similarly to light. New emerging/tailored compound semiconductor materials are at the forefront of this revolution. Intense efforts have been made to understand and control growth technologies related to this class of materials that may lead to further innovation and exploitation thereby creating next generation technologies and devices for future, especially wide bandgap III-nitrides and ultra-wide bandgap boron nitride (BN).

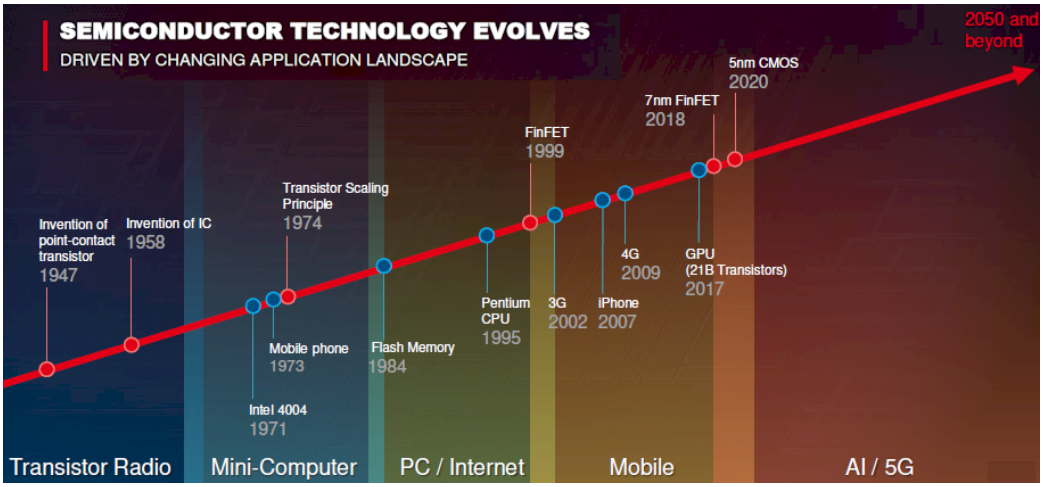

Figure 1. Evolution of semiconductor transistor technology as per the application landscape. Source: TSMC, Taiwan.

1.2. Introduction to III-nitrides

III-nitrides are one of the most futuristic compound semiconductor material systems. They are composed of sp^3 bonded wurtzite crystals such as GaN, InN and AlN that have a direct bandgap with bandgap values of 3.4 eV, 0.7eV and 6.2 eV respectively. This material system also features sp^2 bonded hexagonal layered BN crystals that have an indirect bandgap of around 6 eV as illustrated in the figure 2.

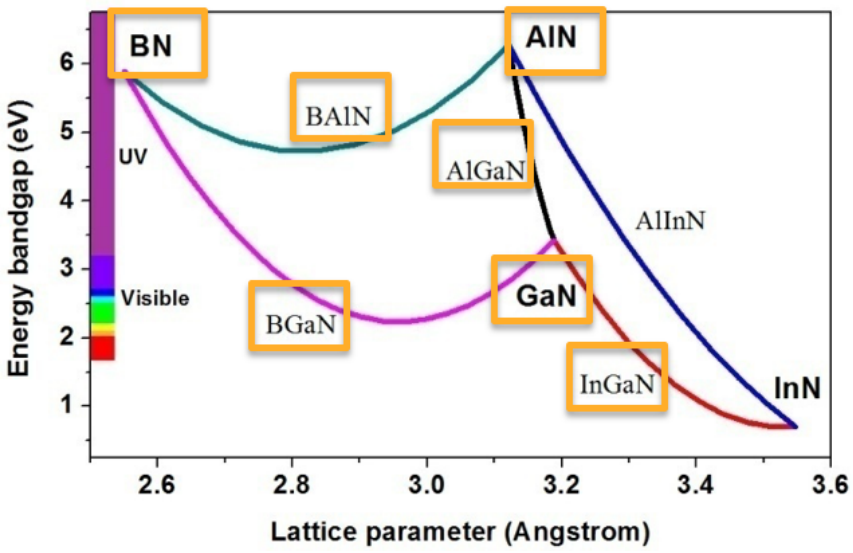

Figure 2: Bandgap energy versus in-plane lattice parameter diagram for III-nitride material system

The effort to develop nitride semiconductors, in particular GaN, was first reported in the sixties and seventies due to the potential light emitting properties of this material and its alloys for the manufacture of LEDS in the spectral ranges of blue and ultraviolet (UV). In 1969, Maruska and Tietjen [Mar69] developed GaN for the first time by hydride vapor phase epitaxy (HVPE). Shortly thereafter, GaN was synthesized by metal organic vapor phase epitaxy (MOVPE) [Man71] and by molecular beam epitaxy (MBE) [Yos75].

The advancement of nitride technology has been stunted by many problems. First, there was no GaN compatible substrate, so the material had to be deposited on high lattice mismatch substrates, such as sapphire, SiC and Si (111). This heteroepitaxial GaN was very conductive due to impurities and crystal defects. This residual n-type conductivity, combined with the high activation energy of the acceptors, made it difficult to fabricate p-n junctions. Despite these problems, Pankove et al. [Pan71] presented in 1971 the first light emitting diode (LED) based on GaN, a diode which consisted of a metal-insulator-semiconductor structure. In 1983, Yoshida et al. [Yos83] demonstrated that the use of an intermediate AlN layer between the sapphire substrate and the GaN epitaxial layer significantly increased the luminescence of the material. Another major advance in research on nitride semiconductors was made in 1989 by Amano et al. [Ama89]: These demonstrated that highly resistive Mg doped GaN could become p-type conductive after exposure to an electron beam in a scanning electron microscope. This discovery made it possible to manufacture the first nitride LED with a p-n junction. Sometime later, Nakamura et al. were successful in activating the acceptor Mg by annealing at 700 ° C in an N2 atmosphere [Nak92].

The development of InGaN-based quantum wells by Nakamura made it possible to significantly improve the performance of LEDs [Nak93, Nak94a, Nak94b], progress which culminated in November 1993 with the announcement of the massive production and marketing of blue LEDs manufactured by Nichia Chemical Industries. Reports of the first blue laser diode operating continuously at room temperature was published by Nichia in 1997 [Nak97].

More than three decades of study has taken a material system that was a research curiosity in 1970's to commercialization of III-nitride semiconductors centered around alloys of binary GaN. The fabrication of highly efficient blue and green light emitting diodes (LEDs) and laser diodes (LDs) is driving the development of gallium nitride alloys-based technology towards industrial maturity. This tremendous progress has been accompanied by increasing penetration of blue and white LEDs into new applications and larger markets, starting with backlighting of LCD displays in mobile phones, computer screens, and TVs, followed by automotive and street lighting, and finally conquering lighting applications in all places. Therefore, it is only fitting that in 2014 the Royal Swedish Academy of Sciences awarded the Nobel Prize for Physics to Isamu Akasaki, Hiroshi Amano, and Shuji Nakamura "for the invention of efficient blue light emitting diodes which has enabled bright and energy-saving white light sources".

Further, the robust and versatile properties of gallium nitride such as its high electric field strength and electron mobility make it an excellent candidate for high speed and high-power electronics. Currently, High-voltage (HV) gallium nitride (GaN) 650-950 V field-effect transistors (FETs) are becoming the next standard for power conversion [Jon16]. Interest in gallium nitride and its alloys has exploded in the past

decade, leading to an expansion of its potential applications for example as ultraviolet light emitters and efficient solar cells. Although the efficiencies and power levels of emerging devices today are still modest, compared to other devices from this material alloys, another paradigm shift in the area of semiconductor-based UV sources is just around the corner. Without doubt the efficiencies will continue to improve over the coming years.

Recently, hexagonal boron nitride (hBN) has emerged as an important multifunctional material system that adds the much-needed functionalities like performance boost and easy lift-off and integration into a flexible platform or other low-cost templates to overcome the above-mentioned cost issues. It also can detect neutrons and because of its ultra-wide bandgap, it can also be utilized as UV detectors. As the performance improves over time it is clear that many more application areas will follow. This broad spectrum of emerging applications has led some to predict that III-nitride alloys will eventually become the third most important semiconductor system, behind GaAs and Si.

1.3. MOVPE growth of III-nitrides

There are several types of growth technologies that have been used to grow III-nitrides including metal organic vapor phase epitaxy (MOVPE) [Den98], molecular beam epitaxy (MBE) [Wan04] [Hoo04] [Raj04], hydride vapor phase epitaxy (HVPE) [Mol99], pulsed laser deposition (PLD), and physical vapor deposition (PVD) on different substrates. The two most promising are molecular beam epitaxy (MBE) and metal organic vapor phase epitaxy (MOVPE). MBE is capable of more uniform layers with abrupt transitions between layers, whereas MOVPE has similar properties and in

addition it is faster, can handle several wafers per run and generally scalable and low in cost. The MBE molecular beam epitaxy technique has faced technical challenges such as nitrogen cell stability and uniformity issues or the high growth temperatures required to achieve crystal quality comparable to MOVPE material. For GaN based LEDs in solid state lighting applications and High electron mobility transistors (HEMT) devices in power conversion applications, MOVPE is the dominant technology owing to the cost advantages. Today all commercial nitride components are synthesized by MOVPE.

MOVPE growth occurs in an inductively or radiantly heated growth chamber with a cold-wall. A highly reactive precursor vapors, typically organometallics are introduced into the chamber where the active ingredients get "pyrolysed" by the hot substrate and react to form the desired compound. Temperatures in the range of 500–1300 °C are used for growth of these III-nitride alloys. For GaN growth, the precursors are ammonia (NH_3) for nitrogen and trimethyl-gallium (TMG) for Ga. For Al in AlGaN growth, the precursors are trimethyl-aluminum (TMA) or triethyl-aluminum (TEA). For In in InGaN, the precursors are trimethyl-indium and triethyl-gallium. In addition to the precursors, carrier gases such as H_2 and N_2 are used to enhance mixing and control of the laminar gas flow within the chamber. The precursors are stored in stainless steel bubblers that are maintained at a constant temperature. The carrier gas (nitrogen or hydrogen) flows into the bubblers, get saturated with vapor of the source molecules and pushed into the growth chamber (reactor). The schematic of III-nitride epitaxial growth is illustrated in Fig. 3.

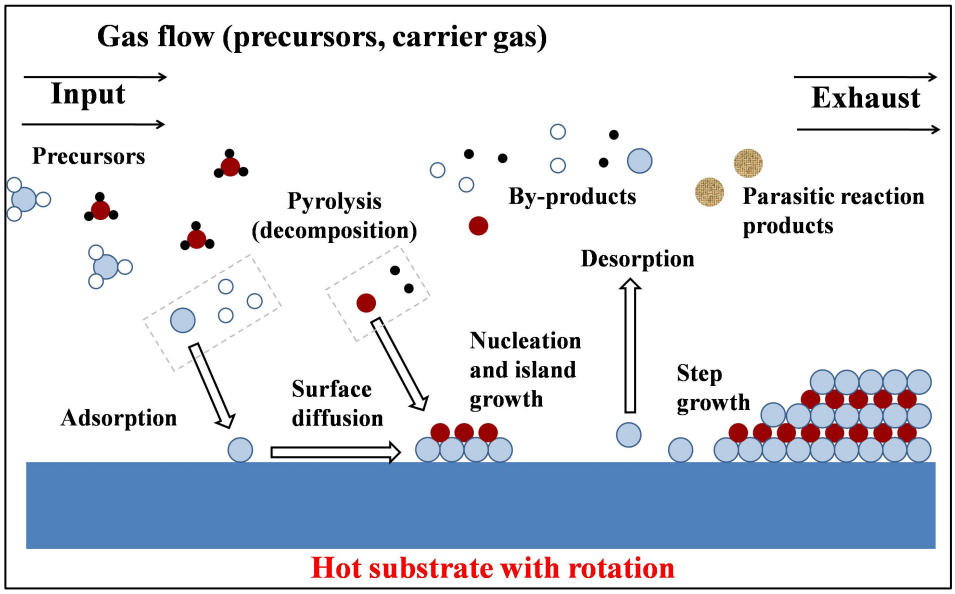

Figure 3: Schematic of III-nitride epitaxial growth. Adapted from [Str99].

The wafer is heated in the reactor to create necessary conditions to crystallize from the vapor phase. This process is analogous to the formation of snow from water vapor (clouds) under specific conditions. The organometallic precursors are mixed with ammonia near the inlet of the reactor and are then transported to the heated zone. The heated organic precursor molecules decompose in the absence of oxygen or any halogen (pyrolysis). The resulting species diffuse through the boundary layer to the growing surface and attach onto the substrate by physisorption. The species can desorb or react with other surface species at this moment. To form a new layer, the active species can diffuse on the surface to form bonds with other atoms either at the bottom of a growth step or other thermodynamically favorable sites, or nucleate at other positions to form islands consequently resulting in further growth.

The general reaction is described in the Eq. below:

$$R_3M+NH_3 \Leftrightarrow MN+3RH.$$

The byproducts that form during the deposition reactions diffuse into the carrier gas away from the deposition zone and flow into the reactor exhaust. Parasitic reactions

between precursors can also occur in the gas phase which would reduce the incorporation efficiency of sources and degrade the quality of epitaxial layers since the particles of the byproducts may fall on the substrate surface hindering the formation of single crystal.

MOVPE growth is a complex process including thermodynamics, kinetics, hydrodynamics and mass transport. The theoretical details can be found in [Str99]. Generally speaking, there are several basic interdependent growth parameters which can be adjusted to control the growth rate and the quality of epitaxial layers: temperature, pressure, V/III ratio (the ratio of ammonia flow rate to the total flow rate of organometallic precursors), III/III ratio (the concentration of one type organometallic precursor in the total organometallic precursors), carrier gas.

Growth temperature should be optimized for the epitaxy of different alloys. Empirically, it is close to one third of the melting point. On the one hand, it requires energy for the pyrolysis of precursors, the diffusion of the atoms on the substrate and activation of the reactions, which is important for the growth rate and surface structural property. On the other hand, at very high temperature, the desorption would be dominant and the substrate surface can be decomposed. Additionally, high temperature would lead to strong parasitic reactions between precursors. Furthermore, growth temperature can strongly shift the composition of In in III nitrides such as InGaN and AlInN.

MOVPE growth of III nitrides is normally done under low pressure (10-300 Torr), in order to reduce the parasitic reactions.

V/III ratio is important for the quality of the layers. If the V/III ratio is too low, supply of nitrogen atoms would be inefficient, and nitrogen vacancies and auto

background doping would be increased. But if the V/III ratio is too high, parasitic reactions would be aggravated and surface mobility of adsorbed atoms would be impeded. III/III ratio which means the concentration of one precursor in the total precursors for III elements (such as TMAl/III and TMG/III) is the key parameter to adjust the composition of the ternary or quaternary alloys. But under the same gas-phase concentration, the composition can also be shifted due to other parameters including temperature, pressure, or the change of the strain state of the surface (composition pulling effect).

Hydrogen (H_2) carrier gas is used in this work for growing GaN, AlN, BN and its alloys since it has better thermal conductivity and purity, as well as faster diffusivity of precursor species and carbon-radical scouring properties compared with N_2. It should be noted that the presence of hydrogen atoms is detrimental to highly volatile In containing alloys growth since it enhances the In desorption and hence N_2 carrier gas is used for growing indium containing alloys. H_2 atmosphere is harmful to Mg-doped layers due to the formation of Mg-H complexes. To overcome this issue in-situ thermal annealing under nitrogen environment is performed to break the Mg-H bonds and to activate the dopants.

Epitaxial materials and structures studied within this work were grown by low-pressure metal-organic vapor-phase epitaxy (LP-MOVPE) using a home-made T-shape reactor system and a commercially available Aixtron close coupled showerhead (CCS) MOVPE reactor system shown in the figure 4. The home-made system was designed and installed by Prof. Abdallah Ougazzaden [Mir89]. Both the system consists of four modules: gas handling/mixing system, reactor chamber, heating system and an exhaust (low pressure) pumping system.

The temperature range is from 400 °C to 1040 °C and the pressure in the reactor can be regulated from 80 to 450 Torr for the growth. Hydrogen or nitrogen can be used as carrier gas. The cold-wall system is applied so that the substrate is much hotter than the other zone and the reactants can be depleted on the substrate, contributing to the growth. During growth, the substrate is rotated at 60 rpm to enhance the layer homogeneity and to help maintain the laminar flow on the sample surface.

A new Aixtron 3×2 inch, close coupled showerhead (CCS) MOVPE system has also been brought into operation and it is shown in Fig. 4. The system has been designed in such way that the surface temperature of substrates in this reactor can reach 1300 °C. This system was used for optimizing BN and AlN based materials which typically require temperature higher than 1100 °C.

Figure 4: MOVPE system and T-shape reactor chamber. Aixtron 3×2 inch, close coupled showerhead (CCS) MOVPE system.

1.4. Scope and content of this memoire

As mentioned previously, tremendous research efforts in the past few decades in the MOVPE growth technologies have led to development and commercialization of visible light emitting diodes, lasers and transistors based on these materials. Millions of above mentioned GaN based devices are manufactured every week. On one hand, GaN, InGaN and AlGaN alloy-based LEDs and HEMTs are attaining industrial maturity and are successful in conquering a substantial market. Despite this success of GaN and related alloys, other III-nitride devices such as InGaN based solar cells and AlGaN based other devices such as UV LEDs still possess significant intrinsic limitations. On the other hand, h-BN has emerged as an important multifunctional material system that adds the much-needed functionalities like performance boost and easy lift-off and integration in to a flexible platform or other low-cost templates to overcome the above-mentioned cost issues. In addition, boron also can detect neutrons because of its high neutron capture cross section and because of its wide bandgap can be utilized for UV detectors. In spite of its strong potential, BN is the least investigated among the III- nitrides semiconductors because the growth of high crystalline quality h-BN has proven to be challenging. This material system also has potential properties that can benefit applications flexible/wearable electronics, etc., which are currently under intense investigation all over the world. These other III-nitride technologies need considerable research efforts and once they reach commercial maturity can gain leverage from GaN based solid state LED foundries for mass production. Current trends in this field are to develop new technologies and add novel functionalities to the conventional device structures for increasing the performance to cost ratio. To adapt for this need, each of these materials has to be tailored to suit specific application, for

example, BN for flexible electronics, In rich InGaN for solar cells, high quality Al rich AlGaN and p-type AlGaN for UV devices etc.,

To accelerate innovation in this technologically important area, understanding and control of these III-nitride materials is of prime importance. Recent advances in epitaxial growth have reignited development in this area. My research specifically focuses on the wafer scale growth of all III-nitrides including 2D layered ultrathin h-BN and bulk BN using state-of-the-art metal organic vapor phase epitaxy (MOVPE) system. New epitaxial growth techniques such as van der Waals epitaxy and remote epitaxy are under intense investigation for the integration of the BN and its alloys with III-nitride based devices by and explore it potential advantages. Novel growth technologies such as semibulk and Nano Selective Area Growth (NSAG) related to the growth of tailored In rich InGaN and Al rich AlGaN alloy materials were also studied for specific applications.

Covering this major research area, this manuscript has been divided in to five equally weighted parts:

1. Boron nitride and its heterostructures
2. Novel boron-based semiconductor alloys.
3. InGaN-based solar cell devices.
4. Nano-Selective Area Growth (NSAG) of ternary alloys.
5. AlGaN based UV sources and sensors.

The first two section covers MOVPE growth of boron based novel semiconductor such as h-BN, BGaN and BAlN. Prof. Ougazzaden's team was the first group in France, and one of the leaders in the world, to launch a research project on the use of MOVPE grown boron nitride and boron alloyed III-nitrides in functional III-nitride devices.

Initially, when we started to explore the growth window for high quality BN, we were limited by the temperature capability of the custom-made T-shape MOVPE reactor. This activity, which was core until 2010, then slowed down with the difficulties in growing high quality boron nitride. Hence, in partnership with AIXTRON, a new close coupled showerhead system with high temperature capabilities was installed in 2015 to continue our research exploring this fascinating 2D material system. This theme was restarted due to the recent advances in MOVPE hardware technology and very intense research efforts from our group while I was leading the second MOVPE system installation and process demonstration. Pushing the limits of the newly installed close coupled showerhead MOVPE system, the desired technology for the BN growth was realized. Now we are one among the pioneers in the MOVPE growth of wafer-scale h-BN and related technologies such as *van der Waals epitaxy.* I describe the realization of Mixed dimensional heterostructures (3D-2D, 2D-2D and 1D-2D) using the h-BN platform. Important III-nitride device technologies were grown on the h-BN platform with promising characteristics that can stimulate industrialization of this class of material and its applications. This 3D-2D architecture could improve the device performance and reduce the cost involved, allowing III-N devices to be used more flexibly in a broader range of applications.

The next two sections are concerned with tailoring of InGaN material to suit high efficiency solar cell and LEDs application. We mainly summarize strain evolution control in InGaN materials with semibulk growth and Nano selective area growth technologies. The fifth part concentrates on UV sources emitting in UV-A (around 280 nm) and UV-C (below 400 nm) constructed with AlGaN based MQW and DBR respectively. In-addition it also describes AlGaN/GaN based HEMTs for gas sensor application. Finally, the last part details my research perspectives.

I would like to mention here that I have strongly contributed to the training on MOVPE and co-supervision of the MOVPE work of several post-doctoral and doctoral students. Their works contributed in a significant way to this dissertation: Dr. Phuong Vuong, Dr. Xin Li, Dr. Youssef El gimili, Dr. Yacine Halfaya. Dr. Taha Ayari, Dr. Renaud Puybaret, Dr. Jeremy Streque, Dr. Chris Bishop, Dr. Charles Munson, Dr. Konstantinos Pantzas, Dr. Mohammed Arif, and Dr. Saiful Alam. All these students have found a positions in prestigious labs and institutions in France and over the world: CNRS, Sandia Lab, IMEC, etc., Inaddition to these doctoral students and post-doctoral researchers, I have had pleasure of working with the entire III-nitrides growth and characterization team, without their support and motivation this manuscript would not be possible.

2. Boron nitride and its heterostructures

2. Introduction

Hexagonal boron nitride (h-BN) is currently attracting interest for use in a wide range of electronics and optoelectronic applications [Dea10] [Li12] [Xu15] [Van18] [Cas16]. Due to its wide bandgap, and potentially strong light emission it can find applications in deep ultraviolet (DUV) region as active layer, as an intrinsic p-type material and as a photodetector [Mba21]. Due to good lattice matching with graphene, it can find application as substrate, as protection/passivation and as gate dielectric in graphene electronics [Van18] [Dah11] [Lal17]. Because of its layered nature, 2D-2D heterostructures with exotic properties can be formed [Geim13] [Shi18] [Gig20]. In addition to this, h-BN has high neutron capture cross section and so finds application as efficient neutron detectors [Mai18].

Outside of these areas, one of the most important applications of h-BN is for heterogenous integration of III-nitride devices. This is driven by the need for devices with flexible, stretchable and large-area form factors for wearable devices [Koy12]. Compared with conventional laser or chemical lift-off processes, mechanical lift-off using hexagonal boron nitride (h-BN) as a release layer for subsequent transfer is fast, inexpensive, and non-destructive so the substrate can be re-used, lowering cost. When compared to graphene [Chu10] [Kim14], the key advantage of using layered h-BN for realizing the III-nitrides is that it can be grown at wafer scale in the same reactor, even in the same epi-run with other III-nitrides. Even though there is room for improvement, considerable progress has been made in fundamental understanding of growth of this interesting material and its emerging III-nitride device integration and liftoff. This chapter summarizes recent progress in growth and understanding of h-BN by MOVPE

and realization of 3D, 2D and 1D configurations of device structures on h-BN platforms and their characteristics and performances. These mixed dimensional structures are especially interesting for pick-and-place transfer process which is useful for some key applications like in displays and photogenetic with the need of a matrix of LEDs with different wavelengths or the integration of optoelectronic and electronic devices on silicon.

2.1 BN growth by MOVPE

As mentioned in the previous section, advances in High Temperature (HT) MOVPE growth reactor technology led to the growth of large-area h-BN layers on 2" and 4" sapphire substrates with high structural quality and uniform morphology by our group as shown in the figure 2.1.

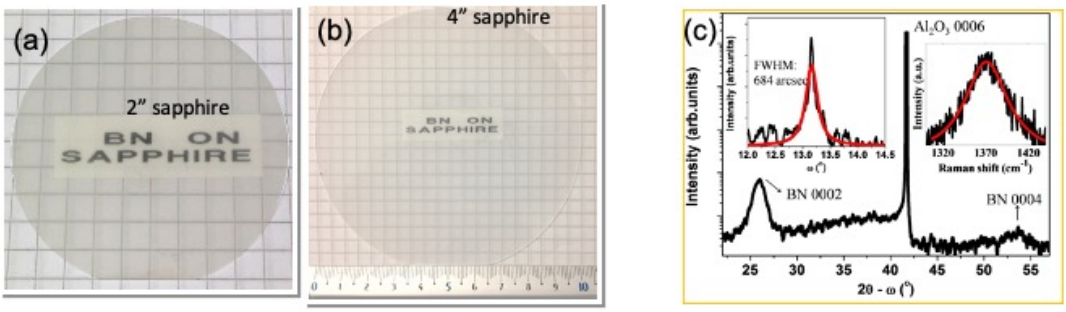

Figure 2.1: (a & b) Photograph of wafer scale h-BN on sapphire. (c) High resolution X-ray diffraction and Raman spectra studies showing respective peaks of h-BN/sapphire.

Our group was the first to demonstrate formation of pleats on the surface, confirming that the BN is layered as presented in the figure 2.2 [Li16] [Sun19] [Aya16]. A topographic transition of BN thin layers has been observed with respect to its thickness as displayed in the figure 2.2. SEM images of the BN samples clearly shows that it is atomically flat up to a thickness less than 10 nm and develops surface pleats with increasing thickness. However, the AFM images revealed pleat formation on the surface of the h-BN samples above 3 nm thick (Figure 2.2 b, c & d right side). These

pleats are characteristics of 2D materials and are now considered as gold standards in benchmarking/determining the quality of the grown material [Li16] [Kob08] [Pad16] [Chu18] [Yan18] [Sun19a] [Dab20]. Because of which, the RMS roughness values increases linearly from 0.2 nm to 3 nm with h-BN thickness.

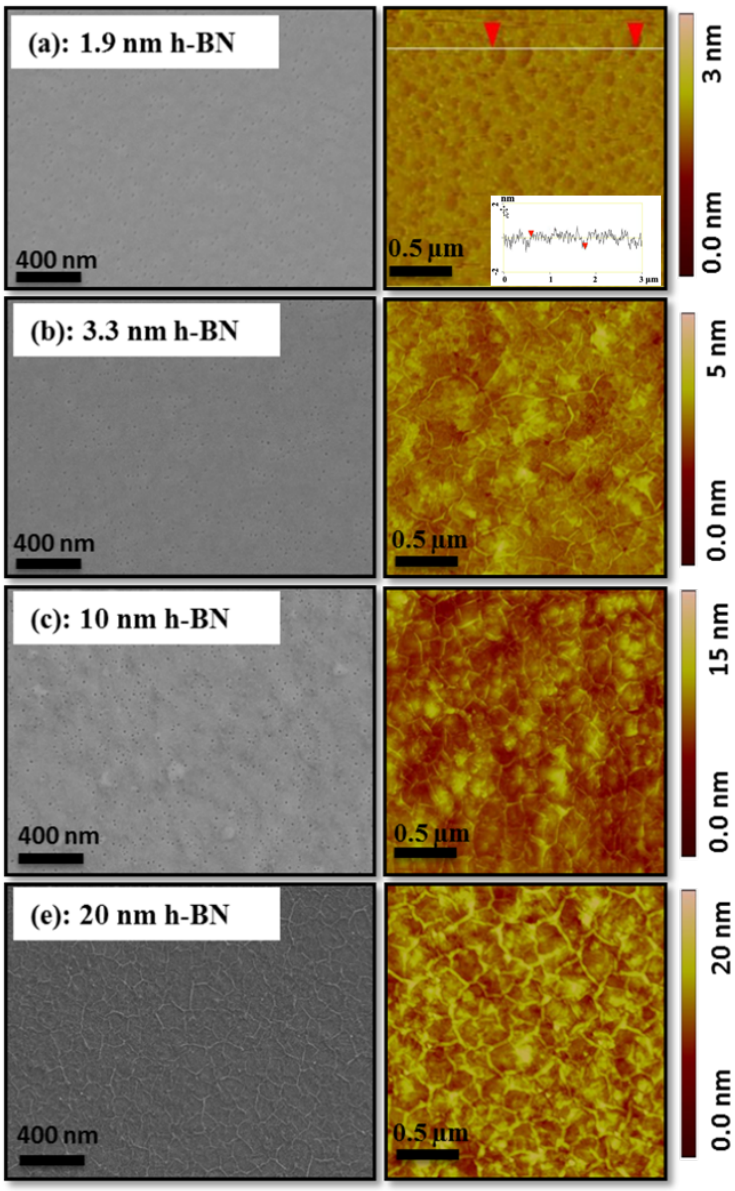

Figure 2.2: SEM (on the left) and AFM (on the right) images of h-BN with different thicknesses (a) 1.9 nm, (b) 3.3 nm, (c) 10 nm and (d) 20 nm thick h-BN.

To analyze the continuity of the thinnest (1.9 nm thick) h-BN layer, line scans from AFM images (inset in Figure 2.2 a) were further investigated. The extracted

maximum depths of the pits are less than 1 nm, which is much lower than the total thickness of the h-BN layer, confirming that the h-BN layer is continuous on the sapphire substrate. The continuity of h-BN layer is important for avoiding direct seeding of III-nitrides or other heteronuclei on sapphire substrates which may hinder complete liftoff of the grown layer [Kon18].

The Raman spectrum of the thin BN film clearly displayed a peak at 1370 cm^{-1} that is attributed to the h-BN first-order Raman E_{2g} vibrational mode [Son10] [Gei66] [Rei05]. The variation of the FWHM of the peak and the peak position with respect to the thickness of the layer is plotted and is as shown in the figure 2.3. The peak FWHM varies from 34 to 52 cm^{-1} on increasing the thickness from 3 to 60 nm. This FWHM values are comparable with what has been observed for single-crystal BN flakes fabricated by MBE [Zuo15] and by CVD [Tay14]. Very narrow FWHM was also reported in the literature for bulk h-BN (11.7 cm^{-1}) or few layer h-BN flakes (15.6 cm^{-1}) [Son10].

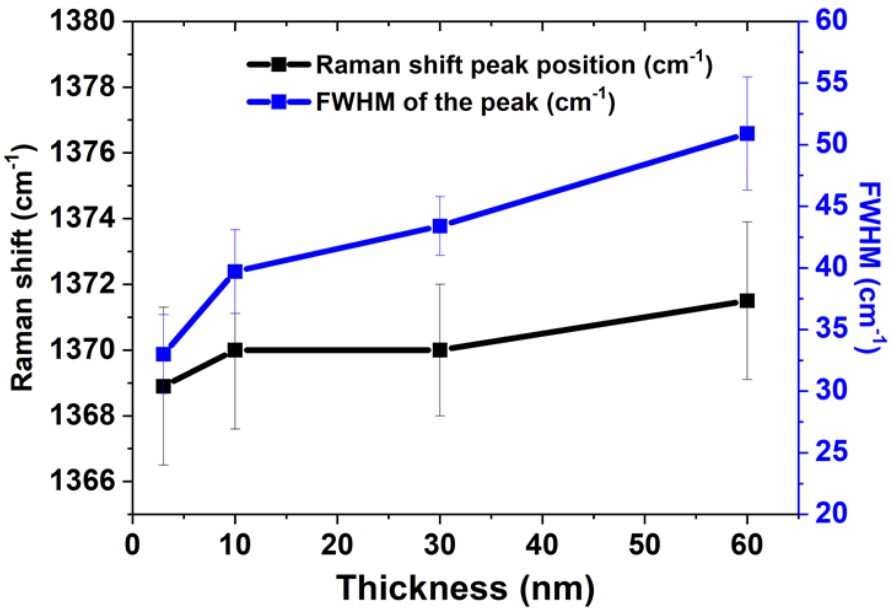

Figure 2.3: Raman peak position and peak full width at half maximum (FWHM) of h-BN with different thicknesses of h-BN.

The relatively broad peak obtained here might be caused by the spatial strain variation in the layer. Nonuniform strain would split the E_{2g} peak as has been observed for other 2D materials [Moh14] [Con13] [Bis14], leading to a broader peak. Especially for 2-in. wafer-scale continuous thin films on a substrate, the thermal strain from the cooling process after the epitaxial growth cannot be effectively released. The pleats pattern presented in the morphology studies is also related to the localized strain in the layer. The strain variation across the pleats produces phonon shifts and hence Raman peak dispersion [Cos13] [Pol15] [Zhu12]. Further increase in the thickness of the BN layers leads to the formation of misoriented islands of BN or turbostratic insertions with thickness and then complete transformation in to 3D turbostratic BN [Chu18] [Li17]. High resolution transmission electron microscopy (HR-TEM) images confirmed that these thin layers of BN are growing layer by layer along the c-axis as shown in the figure 2.4 a. Further stacking sequence and fast Fourier transform (FFT) study also confirmed that the layered structure is hexagonal as shown in the figure 2.4(b).

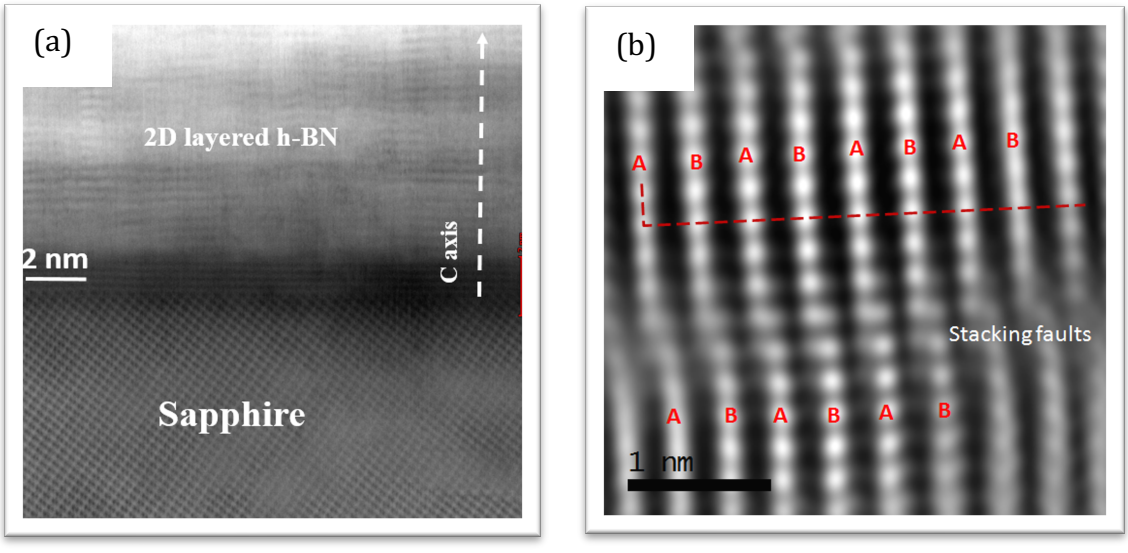

Figure 2.4 (a) Cross-section high-angle annular dark field scanning transmission electron microscopy (HAADF-STEM) image along zone axis <1 1 -2 0> of 30 nm BN grown on sapphire with (b) stacking sequence study confirming that the BN is hexagonal and layered.

It is worth mentioning it here that these BN layers can be mechanically exfoliated from the sapphire substrates by using scotch tape which enables transfer of the layers grown on top of it to any arbitrary platform. This demonstration targeted all the applications mentioned in the introduction section of this chapter including deep UV optoelectronics and graphene electronics [Li16]. Cross-sectional scanning transmission electron microscopy (STEM) reported above explored the origin of these surface pleats. Thin layer buckling occurs in order to release the thermal compression energy that is generated during cooling. In the pleated area, the stacks of as-grown basal planes are still highly oriented, but they are bent following the pleats' waviness. The local decohesion of the BN layer was also observed at the maximum height of a pleats. The local decohesion could be caused by the weaker van der Waals forces between the BN and the substrate in this area due to the direct growth on the sapphire substrate without any 3D bonded nucleation/buffer layers.

2.2 BN growth on patterned sapphire substrates

Layered h-BN (up to approximately 60 nm thick) were grown on dome patterned sapphire substrates as shown in the figure 2.5 (a), to study the local tunability of the structural, optical and electrical behavior of the material.

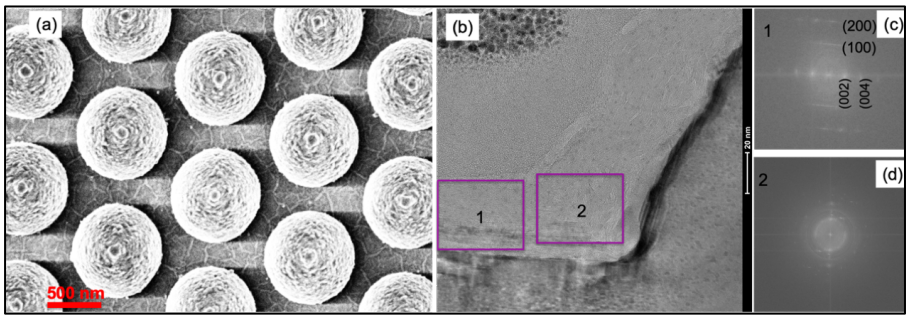

Figure 2.5 (a) SEM image of the as-grown 30 nm h-BN on dome patterned sapphire substrates. (b) Higher magnification image of the intersection between the c-plane sapphire and dome structures, showing the clear bending at the intersection without discontinuity on h-BN layer, misoriented BN islands can also be observed on the BN on sidewalls. (c) fast Fourier transform pattern from the h-BN on the c-plane of the patterned sapphire substrates. (d) fast Fourier transform pattern from the BN layers on the domes of the patterned sapphire substrates.

First, the extreme flexibility of the h-BN was confirmed with this experiment. BN covered the both the *c*-plane and the domes uniformly. Drastic difference in the morphology between the h-BN on the c-plane and BN on the side walls were also observed. Typical wrinkled surface of h-BN on *c*-plane sapphire confirming that this BN is crystalline and layered. More pleats of BN were formed on the domes. Detailed structural studies using HR-TEM on these areas showed that the BN is continuously covering the domes like a blanket of snow. At the intersections of the domes and *c*-plane, strain generated stacking faults and few h-BN islands were seen elucidating strain localization effects induced by the misorientations. Further structural analysis on this cross-sectional TEM images led to a very important finding that the substrate orientation plays a major role in the quality of the h-BN leading to difference in quality of the h-BN laterally as demonstrated in the figure 2.5(b) and their respective FFT patterns in figure 2.5(c) and (d). Further cathodoluminescence studies on the optical characteristics showed that the h-BN layers on c-plane sapphire were having better emission properties with less defect band intensity and observable near band edge emission at 5.9 eV supporting the TEM observations. In-plane flexibility exhibited by the layered h-BN is already interesting for complex device isolation and passivation applications. This study suggested that it is possible to achieve local control of the structural and optical characteristics of the h-BN [Sun19b].

2.3 Van der Waals epitaxial (vdWE) growth of (3D) III-nitrides on (2D) h-BN

Van der Waals epitaxy is relatively new growth technique when compared to conventional epitaxial growth techniques such as homoepitaxy and heteroepitaxy. In homoepitaxial growth technique, even though there are surface dangling bonds there is no/negligible difference between layer and the substrate bonds hence high-quality

layers with very low misfit dislocations can be grown. In heteroepitaxy, rigid surface dangling bonds between the substrate and the layer play an important role. Consequently, the lattice parameters and the lattice mismatch between the layers and substrate is playing a considerable role. The layer interfaces mimic the substrate first as shown in the figure 2.6 (a) and interface layers will be pseudo-morphically strained up to certain thickness called the critical thickness. Then after reaching critical thickness, the layer relaxes to its own lattice by generating defects/dislocations.

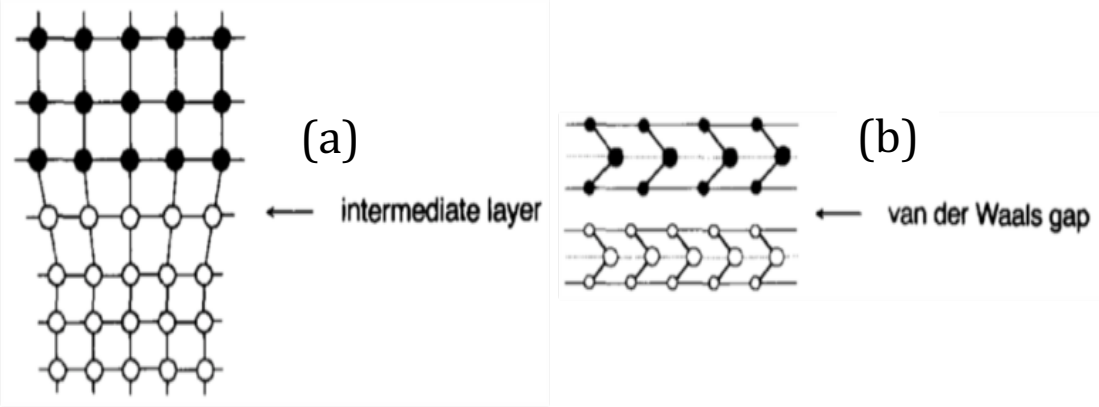

Figure 2.6 (a) conventional epitaxy with pseudo morphically strained layer at the interfaces (b) interfaces in van der Waals epitaxy, showing materials held together by van der Waals forces.

In van der Waals epitaxy the surface dangling bonds free, layered materials are used as templates for growth hence the growth is theoretically independent of the substrates, so high-quality layer free from misfit dislocations can be expected. The layer is held only by weak van der Waals forces without the presence of any 3D bonding between the surface the 2D materials and the layer as shown in the figure 2.6 (b) [Kom84]. Technically, this van der Waals gap can be referred to an angstrom size crack between the layer and substrate, since there is no physical bonding between the layer and the substrates these layer and substrate. This crack can be propagated and the layer can be exfoliated from the substrates very easily. Previously, 2D materials like

graphene has been used as 2D template and interesting device structures has been lifted off [Chu10]. In 2012, Kobayashi et. al. similar exfoliation demonstration is carried out using h-BN layered material, but the scalability and quality of the layered BN was listed as the bottlenecks associated to commercialization of this technology [Kob12]. In our group, we have developed BN which can mitigate the above-mentioned issues, both wafer scale and high-quality BN has been grown and the strategy here was to deploy it in van der Waals epitaxial growth of different III-nitrides mixed dimensional device structures and explore its potential characteristics.

Here, the optimized 3 nm thin and smooth h-BN without any pleats were used as a template to grown GaN based device structures. Direct growth of GaN resulted in Polycrystalline GaN formation due to nucleation issues. $Al_{0.15}Ga_{0.85}N$ interfacial buffers were used to nucleate III-nitrides on h-BN. A specular GaN growth was obtained using this AlGaN interfacial buffer.

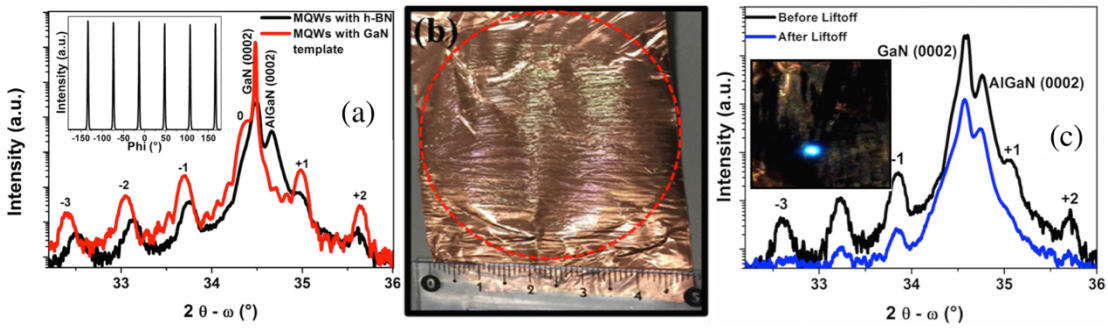

Figure 2.7: (a) High resolution X-ray diffraction 2θ-ω scans of the MQW structure on the h-BN layer and the same structure using conventional GaN template. (b) Photograph of the MQW structure after exfoliation using a copper foil. (c) X-ray diffraction using the 2θ-ω configuration of the same MQW structure before and after the transfer. The inset shows Blue light emission by electrical injection from the exfoliated MQW structure. Ref. [Aya16]

Subsequently, a complete Light Emitting Diodes (LED) structure was grown on thin layered h-BN/sapphire substrates and its characteristics were studied and compared with conventional LED structure on sapphire. The HRXRD 2θ-ω scan on the LEDs on

BN shown in the figure 2.7 (a) shows the signature satellite peaks of the MQW structure on BN which is of comparable quality with the conventional LED. In addition, the inset of the figure 2.7 (a) shows the phi scan with six equidistant peaks vividly proving that the LED structure on BN is single crystalline. Further wafer scale mechanical liftoff was demonstrated using an Al and Cu tapes as shown in the figure 2.7(b). The structural and optical functionality such as satellite peaks of the MQW structure and bright blue light emission was preserved during liftoff as demonstrated in figure 2.7 (c) and its inset respectively [Aya16]. This futuristic demonstration aims at low cost and high yield transfer realization of functional III-nitride devices on flexible or any arbitrary platforms.

Using, similar approach high quality GaN based device structures such as InGaN based solar cell and AlGaN based light emitting diodes (LEDs) and High electron mobility transistors (HEMTs) were grown on h-BN and transfer to arbitrary substrates has been demonstrated which has been discussed separately in chapter 4 and 5 [Aya16] [Aya17] [Aya18].

2.4 Remote epitaxy on BN

Remote epitaxy is another new growth technology adapted to the use of 2D materials. In this cutting-edge technology, remote atomic interaction of underlying substrates transmits its atomic registry to overlaying films through 2D materials. This leads to realization of layers that are similar to high quality epitaxial layers on 2D materials for example high quality GaAs on 1Monolayer (ML) Graphene/GaAs [Kim17]. This remote atomic interaction through 2D materials is governed by the binding nature, that is, the polarity of atomic bonds, both in the underlying substrates and in 2D material interlayers.

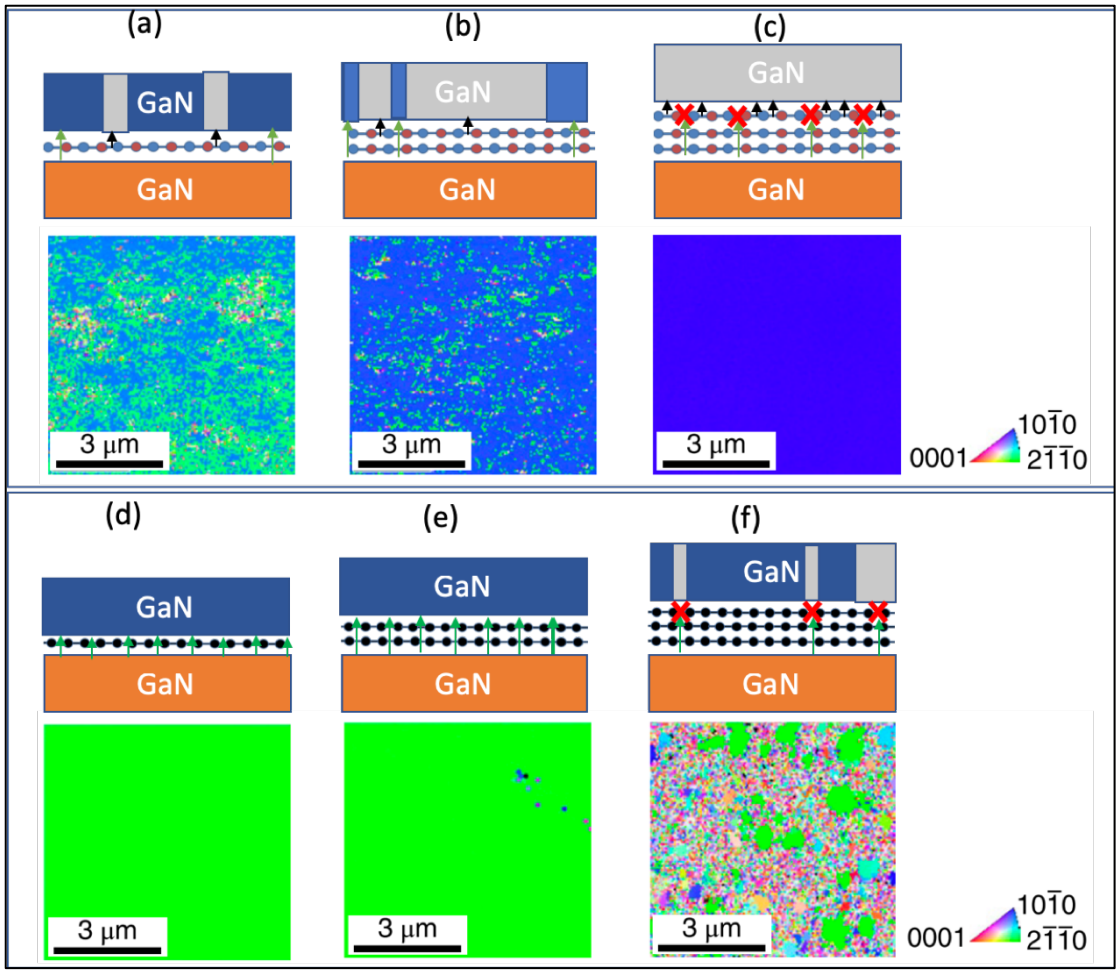

Figure 2.8 Schematic (top) and Electron Backscatter Diffraction (EBSD) (bottom) of the exfoliated surface of GaN on (a)1-ML-hBN/GaN (b), 2ML-hBN/GaN (c) and 3ML- hBN/GaN (d) 1-ML-graphene/GaN (e), 2ML-graphene/GaN (g) and 3ML-graphene/GaN (f). a.u., arbitrary units.

Although the potential field from covalent-bonded materials is screened by a monolayer of graphene, that from ionic-bonded materials is strong enough to penetrate through a few layers of graphene. For example, attempting remote epitaxy of elemental semiconductors with covalent bonding such as Si and Ge resulted in the formation of polycrystalline films, whereas substrate that have ionic bonding properties affects growth through a graphene layer; furthermore, the potential field penetration depth increases with increased ionicity of substrate materials. As such, critical graphene thicknesses for remote epitaxy of GaAs (30% ionicity), GaN (50% ionicity) and LiF (90% ionicity) are 1 ML, 2 ML and 3 ML, respectively. Since ionicity governs remote

epitaxial field penetration through graphene, all compound materials could be grown via remote epitaxy as a perfect single-crystalline form.

However, perfect transparency of remote interaction is not guaranteed in other 2D materials that have an ionic character as this can also play a role as an epitaxial seed layer. Such field penetration is substantially attenuated by 2D hexagonal boron nitride, which itself has polarization in its atomic bonds. For example, 1 ML h-BN is not thick enough to screen the field from the GaN substrate, hence remote epitaxy can still occur. In fact, GaN grown on 1 ML hBN/GaN substrates shows two different azimuthal orientations; one follows the orientation of the hBN ML and the second is seeded to the GaN substrate as shown in figure 2.8 (a & b). Thus, both vdWE and remote epitaxy occur simultaneously; in contrast, only vdWE occurs when 3 ML hBN interlayer is used, as the substrate potential field is completely screened as shown in figure 2.8(c). In the case of graphene, the substrate field is well transmitted through 1 ML owing to the non-polarity of this material as demonstrated in figure 2.8 (d & e); still, GaN films grown on 3 ML graphene is polycrystalline, this time due to insufficient seeding effect from the substrate as shown in figure 2.8 (f). This work was carried out in collaboration with a Prof. Jeehwan Kim group in MIT [Kon18].

Difficulties with van der Waals epitaxy of III-nitrides and growth of BN on dielectric patterned sapphire substrates.

As described earlier, thin layer buckling in 2D materials occurs in order to release the thermal compression energy that is generated during cooling. The local decohesion or delamination could be caused by the weaker van der Waals forces between the BN and the substrate due to the direct growth on the sapphire substrate without any 3D bonded nucleation/buffer layers. Controlling this stress induced decohesion and its evolution in BN may lead to many reliable and reproducible

applications, especially in van der Waals epitaxial growth of the other III-nitrides where self-delamination during growth and delamination's during the front-end process are reported and seen as serious issues.

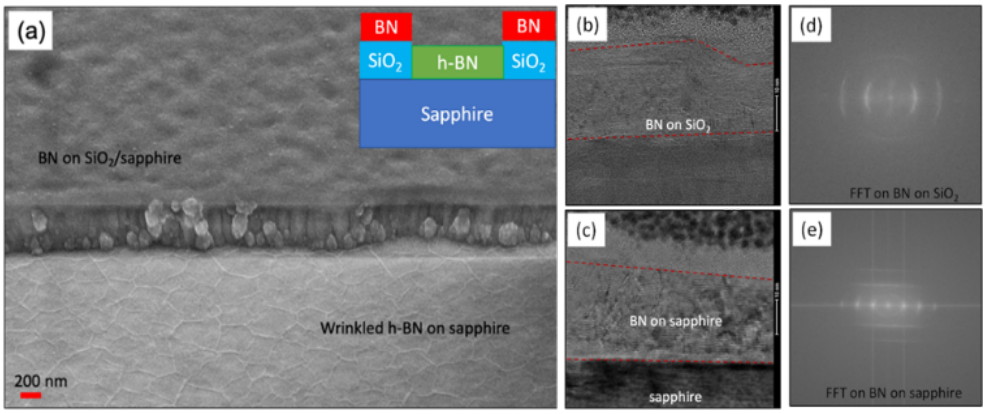

Figure 2.9: a. Top-view SEM image of the BN on SiO2 dielectric patterns and on c-plane sapphire along with cross section of the structure in the inset. (b and c) HR-TEM images of the BN deposits on SiO2 pattern and c-plane sapphire respectively. The scale bar is for 10 nm. FFT patterns (d and e) captured from the area shown in b and c respectively indicates that the BN on SiO2 is nanocrystalline whereas BN on c-plane sapphire is perfectly crystalline.

To control and study its evolution and characteristics, BN was grown on patterned sapphire substrates as reported in the previous section. It is worth noting that, generally, III-nitrides grows at relatively higher temperature, may be before the evolution of the surface pleats on thin h-BN. Local control of stress can be achieved by controlling the orientational characteristics of the substrates as observed in the dome patterned sapphire substrates that was described in the earlier section. It is necessary to understand the mechanism well enough for control of structural and optical characteristics, so that BN can be utilized for growth of device structures.

The use of dielectric patterned sapphire substrates with different geometries may bring better clarity to this study, hence, they were utilized. High quality thicker h-BN layers were grown on dielectric patterned sapphire substrates. As expected, on the

un-patterned area the h-BN formed semi-hexagonal pleats which matched the quality of standard high-quality h-BN as shown in SEM images in figure 2.9 (a). BN deposits on the dielectric region were difficult to detect. However, the presence of BN on the dielectric patterns were identified and confirmed with localized secondary ion mass spectroscopy (SIMS) measurements and found to be of comparable thickness to BN on un-patterned area. This study confirmed that the BN growth process under this growth condition is non-selective. Further cross-sectional TEM studies on the samples were carried out to study deeply and is as shown in the figure 2.9 b and c. BN on SiO_2 presented a layered structure when compared to the BN on *c*-plane sapphire. However, the fast Fourier transform (FFT) pattern of this high-resolution TEM image shown in figure 2.9 d and e clearly showed the differences between these layers. It gave a diffused ring pattern for BN on SiO_2 indicating that this BN has only short-range order whereas the BN on *c*-plane sapphire displayed diffraction spots corresponding to the hexagonal structure of BN confirming that they are completely crystalline. This deep study demonstrates that the BN grows non selectively but there is radical difference in quality between BN on dielectric SiO_2 and on sapphire substrates which can be exploited for selective growth of III-Nitride device structures.

2.5 Van der Waals epitaxial growth of 3D GaN-based heterostructures on BN on dielectric patterned sapphire substrates

III-nitride device structures were grown on BN on dielectric patterned sapphire substrates along with control samples. These samples were characterized to study the selectivity of III-nitrides. To study the structural characteristics of these device structures, non-destructive XRD measurements were made on the sample on h-BN templates.

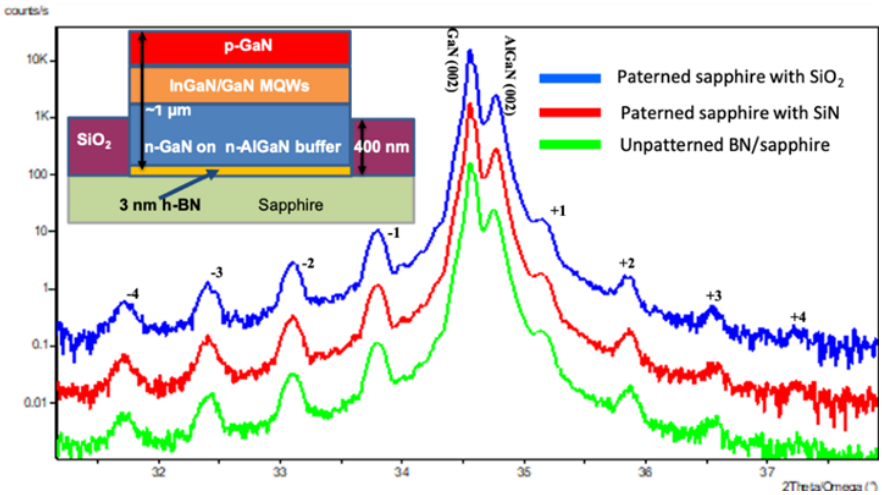

Figure 2.10. HR-XRD 2θ-ω scans measured from GaN based blue LEDs on h-BN grown on patterned and unpatterned sapphire templates.

High-Resolution X-Ray Diffraction (HR-XRD) 2θ−ω scans of 5 period InGaN/GaN blue LEDs on h-BN on SiO_2 and SiN patterned sapphire substrates in comparison with h-BN on unpatterned sapphire substrates is shown in the Figure 2.10. This measured diffraction pattern is similar to the one reported previously and comparable with the standard LED on sapphire [Aya16]. The XRD diffraction pattern clearly presented the MQWs satellite peaks up to the fourth order as well as the peaks from the GaN and $Al_{0.14}Ga_{0.86}N$ layers confirming high interface quality in the InGaN/GaN MQW structure. Comparing the measured scans on the unpatterned sample with the one on the patterned, it can be observed that there is no considerable peak shift or peak broadening, which further confirms that the patterning process does not affect the structural quality of the LEDs on BN. This is unexpected because the van der Waals epitaxial growth of boron nitride is not likely completely selective, since it is theoretically substrate independent growth. On the other hand, the quality of the BN on randomly oriented SiO_2 patterns may be significantly different when compared to h-BN on highly oriented *c*-plane sapphire, since the substrate orientation controls the quality of these van der Waals layers [Sun19a] [Zha18]. This cross-quality BN on SiO_2 patterns

should lead to non-uniform III-nitride growth due to difference in surface growth kinetics that may alter the XRD scans unless otherwise the GaN device structures are growing selectively avoiding the BN on SiO_2. To confirm these insights first surface morphology of the GaN LEDs on patterned samples were studied with scanning electron microscope (SEM).

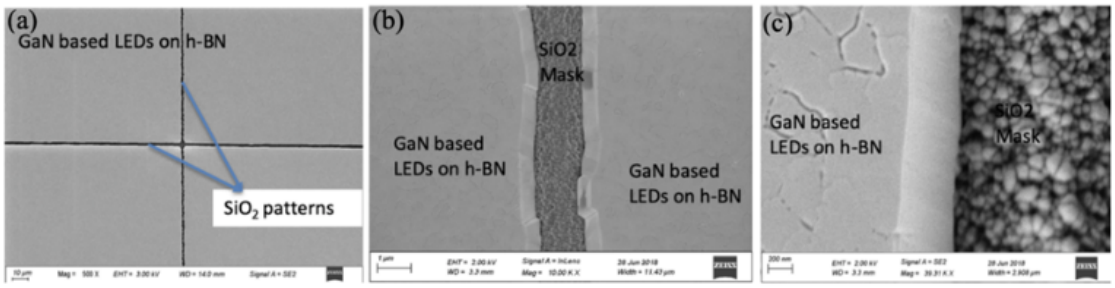

Figure 2.11. SEM image of the surface of InGaN based blue LEDs grown on SiO2 patterned h-BN templates in various magnifications clearly showing selective epitaxial lateral growth of GaN device structures on the h-BN on c-plane sapphire substrates only.

The SEM image in fig. 2.11(a) vividly shows the selective growth of the GaN based LED structure in regions where layered h-BN is deposited, avoiding the growth on randomly oriented BN on SiO_2. The higher magnification SEM image shown in figure 2.11 (b) depicts a clear boundary and very sharp side walls of the LEDs structure in each side of the mask which is required to guarantee the separation between the devices after process fabrication. It is also observed from other higher magnification images shown in figure 2.11 (c) that there are some nanocrystalline deposits on the surface of the SiO_2 masks which can be cross quality BN and other polycrystalline materials deposits of III-nitride. Similar selectivity has been observed in SiN patterned sapphire substrates also. Following this study, a full front-end lithography, etching and metal deposition process was applied on the LEDs wafer to create devices on the as-grown wafer as shown in the figure 2.12.

Thanks to the patterning with the SiO_2 mask, the fabricated devices are already physically isolated from each other. The discrete LEDs can be released and transferred individually without the need for a dicing step. In this work, a particular set of devices has been released from the matrix of processed devices by means of a water-dissolvable tape and transferred to a flexible aluminum tape. Mechanical exfoliation transfer process is relatively fast (only takes few seconds) after pressing the tape on the layer for proper contact, peel off involves shear force on the interface. The water dissolvable tape has 20 μm thick adhesive layer on it [Kar20] [Aya19].

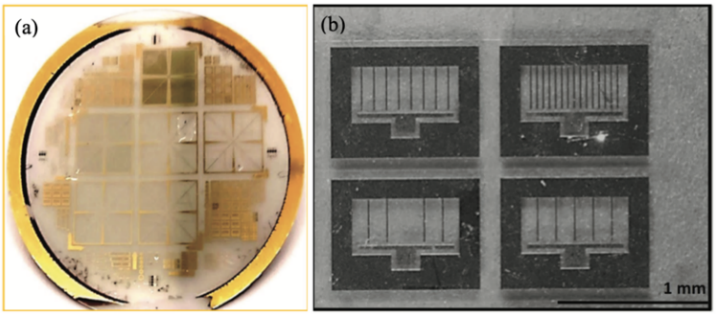

Figure 2.12. (a) Photograph and (b) optical microscope image of devices with 1 mm² contact area of the full front end processed GaN based blue LEDs on h-BN grown on patterned sapphire templates.

The tape is attached to a carrier for the release. Then, once the device is placed on the final support platform, the tape is simply removed by dissolving it in water for around 1 min. The pick-and-place capability is demonstrated in Figure 2.13(a) where we clearly see that specific aimed devices have been lifted off from sapphire leaving their locations empty, while other untargeted LEDs remained on the growth wafer. During the transfer process, device structures remained completely intact and free from cracks and metallic contact damage. I–V measurements for a released LEDs were performed after its transfer to confirm the preservation of the device functionality as shown in Figure 2.13(b), inset shows a photograph of the blue light emission from the LED after its release from the substrate and transfer on to the aluminum tape.

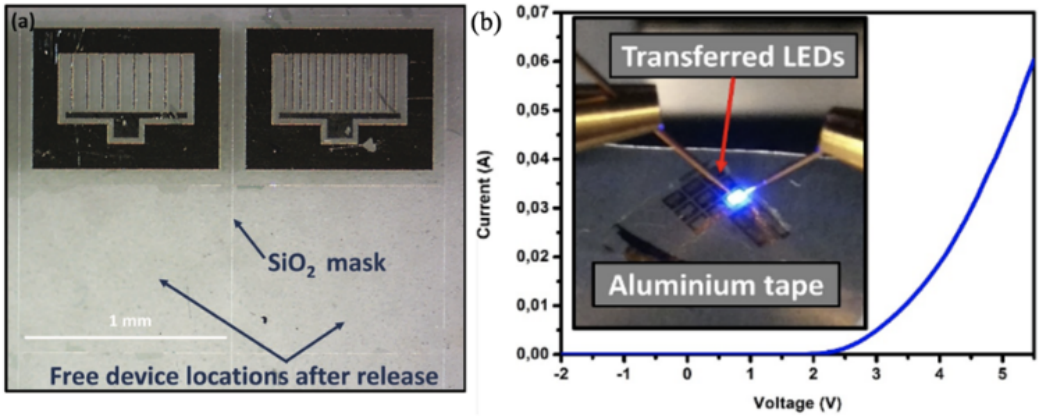

Figure 2.13. (a) Optical microscope images showing two LED devices with 1 mm2 contact area and empty locations of two lifted off LEDs on h-BN grown on the patterned sapphire demonstrating patterning induced isolation and specific device liftoff. (b) I–V characteristics of a device after its transfer with its blue light emission shown in the inset.

In the above sections, the high-quality 3 dimensional (3D) III-nitride device structures growth on the h-BN with mechanical exfoliation and transfer capabilities has been demonstrated. In addition, an improved patterning-based growth of drastically different BN allows GaN to be grown selectively. Subsequently, active device structures with local pick and place possibilities without compromising the structural and optical characteristics of the device structures is demonstrated which is promising for industrial and commercial applications. Similar quality, isolation and local transfer can be achieved if the one-dimensional (1D) GaN nanowires are grown on the h-BN platform. Hence, a series of experiments designed and launched to fully study this 1D-2D configuration that can further extend the applications of this class of materials.

2.6 Self assembled van der Waals epitaxial growth of 1D GaN-based heterostructures on BN on sapphire substrates

The growth of 1D nitride device structures on h-BN by self-assembly on layered h-BN was explored. First h-BN was grown after nitridation and surface smoothing by AlN deposition on sapphire substrates. As reported by Kobayashi et al 2012, Direct

growth of GaN on h-BN resulted in the formation of sparsely distributed isolated discrete polycrystalline GaN lumps [Koy12]. Uniform nucleation on dangling bond-free h-BN was induced using short pulse of AlN growth before successive GaN growth. AlN islands on h-BN serve as nucleation sites for the uniform growth of GaN. Immediately after AlN nucleation, GaN was grown under conventional GaN growth conditions, forming vertical GaN nanorods.

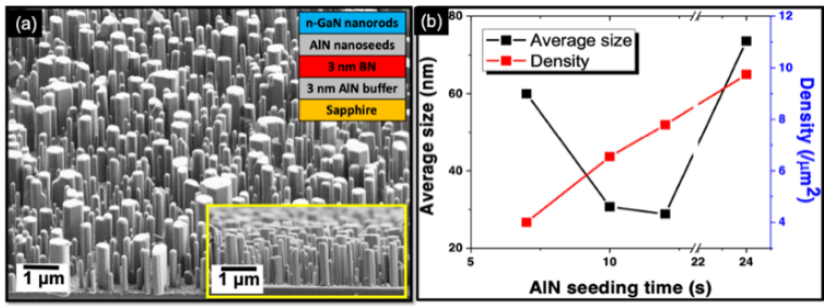

Figure 2.14. SEM images. (a) Tilted view of the GaN nanorod structure on the sapphire substrates with clear hexagonal symmetry, inset of the figure shows higher magnification cross-sectional view of the GaN nanostructures vividly displaying the vertical alignment. (b) Variation of nucleation density and average size (diameter) of GaN nanorods with AlN seeding time.

Figure 2.14(a) shows the tilted scanning electron microscopy (SEM) image of the formed GaN nanorod arrays with the hexagonal six-fold arrangement of the wurtzite lattice structure on sapphire substrates. Inset of Figure 2.14(a) shows the cross-sectional SEM image of the GaN nanorods confirming vertical alignment. The unprecedented formation of GaN nanorods on layered h-BN in single step and wafer-scale uniformity is the result of the combination of van der Waals epitaxial growth of h-BN layer and nanoseeding of crystals by AlN. We note that control over the density and aspect ratio of the GaN nanorods can be achieved by adjusting the density and size of the AlN islands on h-BN. The islands of varying size and density were grown by changing the AlN growth time on 2D h-BN, after which the GaN nanorods were grown. As the AlN nucleation layer growth time increases, the nanorod density increases almost linearly

and the size of the rods decreases. The variation of nucleation density and the average size with respect to the AlN seeding or nucleation layer growth time is shown in Figure 2.14(b). Raising of the nucleation density beyond a certain limit (18 s of AlN growth) resulted in coalesced GaN nanorods structures pushing the average size estimation to be out of the trend.

Having established the high-quality growth and control of GaN nanowires on h-BN templates, the feasibility of growing nanodevice structures on 2D layered h-BN was explored. PIN nanodevice structures as shown in the inset of Figure 2.15(a) were grown. The initial GaN nanorod on h-BN buffered sapphire templates was doped with silane to form a n-type rod. In addition to this, nanostructures, InGaN layers, and p-GaN layers with Mg doping were added on top of it.

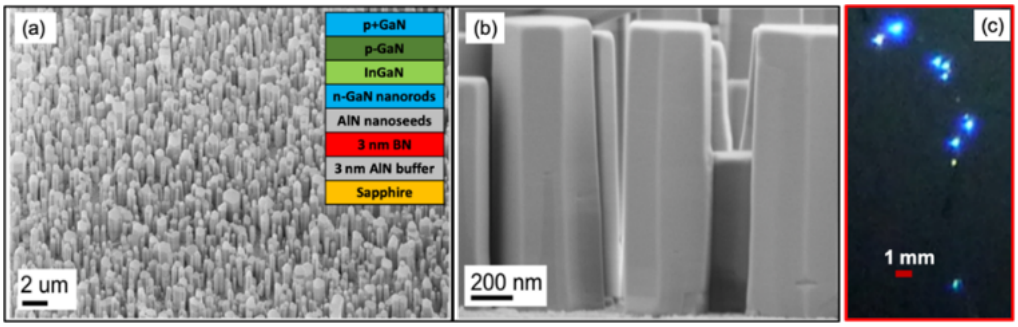

Figure 2.15. SEM image of (a) p-GaN/i-InGaN/n-GaN nano-PIN structures on h-BN/sapphire substrates, inset shows designed structure. (b) High magnification cross-sectional SEM image of the nano-PIN on the h-BN/sapphire substrates showing the vertical alignment and flat- topped hexagonal columns of the nanorods and (c) blue light emission from the nano-PIN structure under electrical injection.

Figure 2.15(a) shows the low magnification tilted view SEM image of the resulting p-GaN/i-InGaN/n-GaN PIN nanodevices. Figure 2.15(b) shows the cross-sectional high magnification image of a few PIN nanodevice structures on the AlN/h-BN buffered sapphire substrates. These nanodevice structures are uniform in shape with flat top and have the hexagonal sixfold arrangement confirming the single crystalline

wurtzite lattice structure. Even though the p-GaN/i-InGaN/n-GaN PIN device structures were grown on layered h-BN, the hexagonal shape of these nanorod-based structures is similar to those of GaN nano- and microrods reported on single crystal substrates [Dai15] [Li12] [Chu14]. We envision that the tilt component of the nanorods structures can be further controlled by improving the quality of the AlN nucleation layer and h-BN layer. Under electrical injection, the PIN nanodevice structures emitted intense blue light as shown in Figure 2.15 (c) which endorses the full functionality of the as-grown nanodevice structures. The formation of the core-shell structure and the presence of the h-BN was confirmed by high-resolution cross sectional transmission electron microscope studies and reported separately elsewhere [Sun19b].

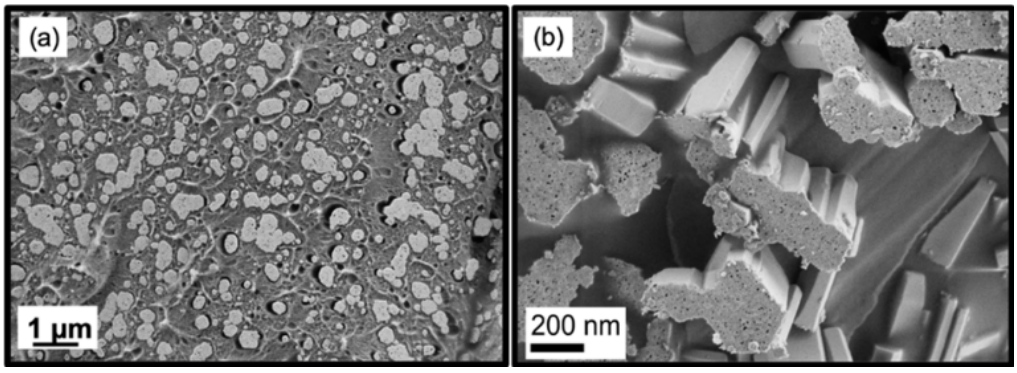

Figure 2.16. (a) Lifted-off core–shell nanorods using copper tape (bottom view) and b) higher magnification SEM image confirming the retention of the core–shell nanorods after the lift-off.

The nanorods on 2 in. sapphire substrate were lifted off by a simple mechanical peeling technique using a copper tape. After taping the surface of nanorods, the tape was peeled off holding the sapphire substrates which prompted a shear stress at the nanorods/h-BN interfaces separating them. The SEM images of the top surface of the lifted-off planarized nanorods in Cu metallic tape are shown in Figure 2.16(a & b). The SEM image clearly displays damage free bases of the nanorods with flat surfaces and no visible breakage or cracks on the nanorod structures. Backside surfaces of the nanorods are smooth and similar to the surface of the h-BN covered with misoriented

AlN or AlGaN islands with some nanovoids on it, which further confirms that the lift-off occurred at the h-BN/ sapphire interfaces. This simple mechanical exfoliation technique allows transfer of the nanorods to any appropriate platform without any interface damage preserving the structural and optical quality.

2.7 2D-2D van der Waals heterostructures using h-BN

2D/2D heterointerfaces are at the focus of scientific attention in view of their numerous exciting physical properties [Geim13]. Assembling 2D materials based heterostructure is often described as stacking LEGO blocks as shown in the figure 2.17.

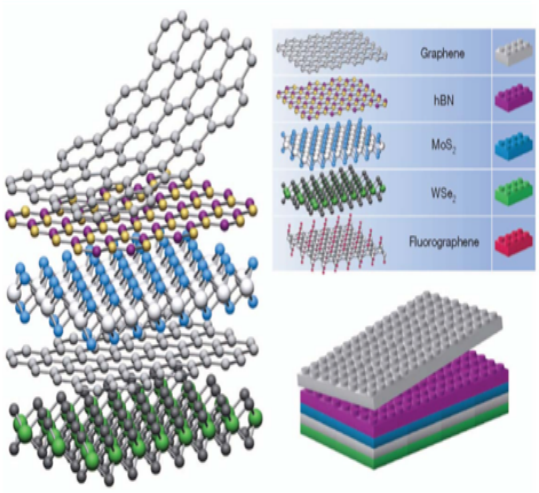

Figure 2.17. Building vdW heterostructures. If one considers 2D crystals as Lego blocks (right panel), construction of a huge variety of layered structures becomes possible. Conceptually, this atomic-scale LEGO employs different 'construction' rules and a distinct set of materials than conventional Crystals that are 3D bonded Ref. [Gei13].

Even though realizing this heterostructure stack by growth is the best route, due to intrinsic difficulties in growth of these chemically different materials, the entire assembly and exploration of the interesting properties must be done via other heterointegration techniques. However, splitting atomically thin layers from 2D bulk crystal material for use in electronics has proven difficult to do on a commercial scale. The existing process, in which individual flakes are split off from the bulk crystals by

repeatedly stamping the crystals onto an adhesive tape, is unreliable and time-consuming, requiring many hours to harvest enough material and form a device.

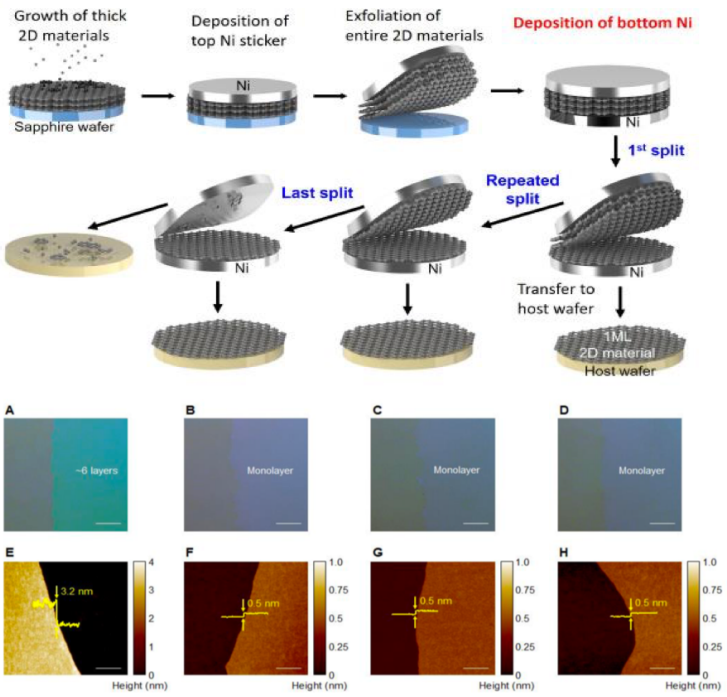

Figure 2.18. Layer Resolved Splitting (LRS) of 2D materials. Schematic illustration explaining the LRS process of 2D materials. Split of h-BN into monolayer using our LRS technique. (A to D) Optical microscopy images and (E to H) AFM images with height profiles of h-BN films for as-exfoliated thick h-BN (A) and (E), monolayers of h-BN obtained by first (B) and (F), second (C) and (G), and third (D) and (H) LRS processes. Scale bars for optical microscopy images and AFM images are 50 µm and 1 µm, respectively. Ref [Shi18].

This work, in collaboration with a Prof. Jeehwan Kim's group at MIT, demonstrates, monolayer-by-monolayer isolation of 2-D materials at the wafer scale using Ni sticker on h-BN and other related 2D materials. The process flow of the controlled crack propagation technique is as shown in the figure 2.18. This technique brought the dream of achieving the 2D heterostructures in wafer scale to commercial reality. In this, atomic layer resolved splitting technique the pristine and perfect bottom 2D layers at the interfaces were accessed after first exfoliation using Ni layer and flipping it. Subsequent atomic layers from the thick stack can also be separated by using

the same approach. One such multiple single-layer separation of h-BN from MOVPE grown multi-layered h-BN is also shown in the figure 2.18.

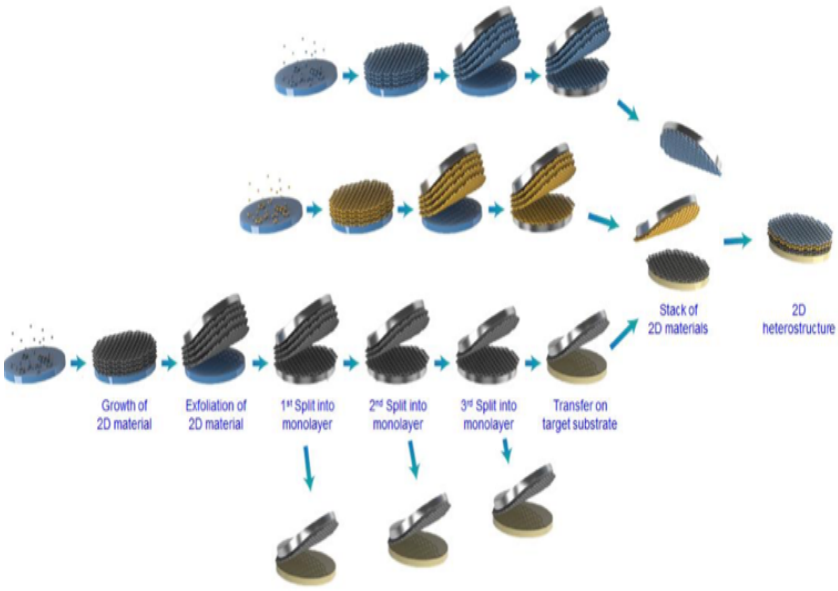

Figure 2.19. Schematic illustrations of 2D heterostructure via LRS process. Flow diagram showing the fabrication of the 2D heterostructure using monolayer 2D materials obtained through LRS process. Ref [Shi18].

Consequently, bringing together all classes of 2D materials including metals, semiconductors and insulators forming heterostructure with better functionality in wafer scale is demonstrated as shown in the figure 2.19.

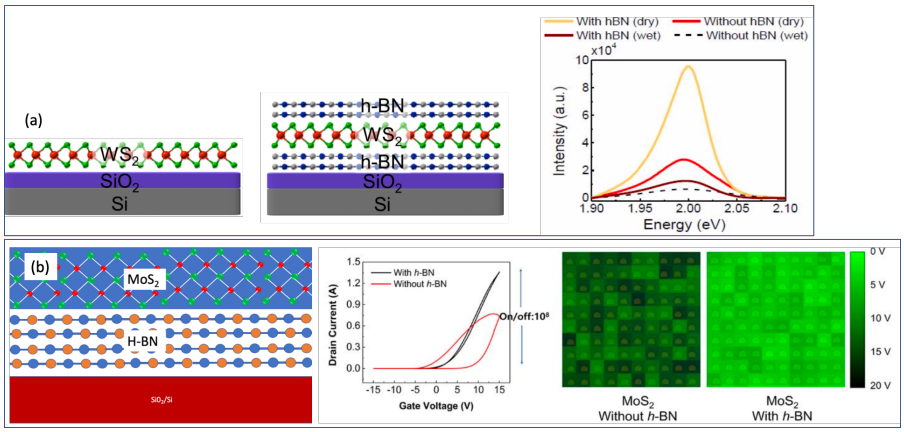

Figure 2.20 (a) 2D heterostructures structures realized with Dry and Wet transfer methods and Representative PL spectra of all different structures made by different methods. (b) 2D heterostructures based transistor structures realized with Dry transfer methods, Representative of drain current voltage characteristics of MoS_2 based FET and 2D color maps of the hysteresis voltage extracted from it. Ref [Shi18].

In this way, they could be used to create ultra-thin, flexible, transparent and wearable electronic devices. Two examples of devices fabricated with h-BN with better performances are shown in the figure 2.20.

Although, the above method to produce 2D/2D heterostructures is very promising for wafer-scale fabrication of devices that may take us close to commercialization. Interface contaminants or disordered interfaces may affect the yield and reliability of the devices. Also, electronic transport is highly sensitive to the alignment of different layers with respect to the substrates.

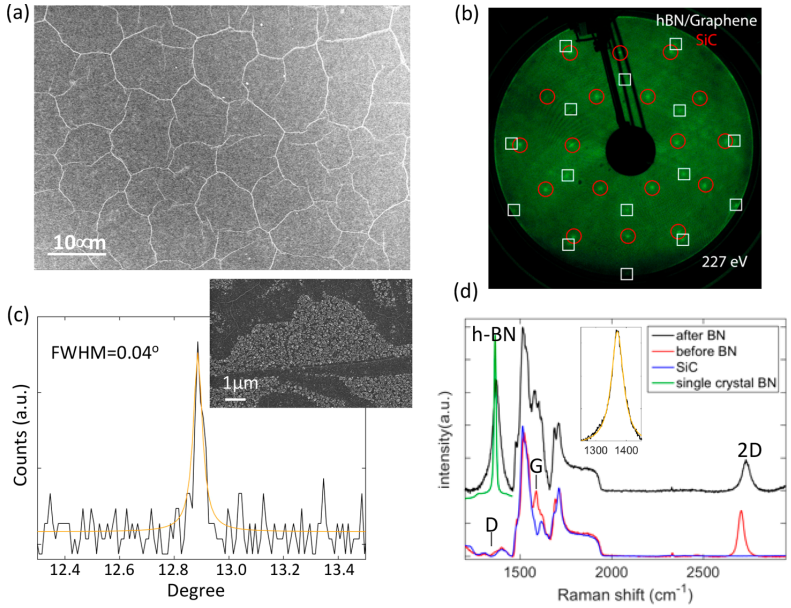

Figure 2.21. Analysis of an h-BN/EG/SiC heterostructure. (a) SEM image of an h-BN film prepared on a monolayer epigraphene of the Si-face (SiC(0001)), showing a homogeneous full coverage. White lines are pleats. (b) Low energy electron diffraction performed with a 227 eV electron beam, showing the expected h-BN, EG, and SiC diffraction spots. The relative azimuthal orientation of the spots and the absence of rings and other anomalies confirm the epitaxy of the heterostructure h-BN/EG/SiC. (c) The HR-XRD rocking curve has a full width at half maximum (fwhm) of 0.04°, demonstrating the extreme flatness of the film layers. Inset: SEM image of h-BN coating on a partially graphitized SiC surface, composed of EG ribbons (grown on natural SiC substrate step walls) separated by buffer layer regions, showing the smooth h-BN/EG surface (dark areas), compared with the rough h-BN/buffer layer surface caused by the very high density of nucleation sites on the buffer layer. (d) Raman spectra of a few graphene layers on the carbon face (red) compared to the bare SiC spectrum (blue). The Raman spectrum after h-BN growth (black) displays a large peak at 1370 cm−1 that is ascribed to the h-BN E2g due to the absence of a D peak in the as-grown EG. (For this spectrum, the disordered top h-BN layers are mechanically removed.) Inset: Lorentizan fit of the peak at 1370 cm−1 (fwhm = 47.3 cm−1). Ref [Gig20].

Epitaxial growth of these heterostructures is indispensable and may be offering technologically viable production solutions that may have better yield, reproducibility at lower cost. Hence, A multilayer h-BN was grown epitaxially on Epitaxial Graphene (EG) using a migration- enhanced metalorganic vapor phase epitaxy (ME-MOVPE) process. In this high temperature process, triethylboron (TEB) and ammonia (NH_3) are used to produce a multilayer h-BN film on the sapphire wafer, informing the present approach. Direct evidence that the ME-MOVPE process yields atomically sharp h-BN/graphene epitaxial interfaces, with a templated h-BN growth on graphene. This result, combined with the industrial compatibility and fast growth process, makes MOVPE a method of choice.

Conventional atomic layer deposition is a cyclic process involving two different precursor molecules in the gas phase that are alternately introduced on a surface and in which each cycle deposits exactly one atomic layer on top of the film. In contrast, in the migration-enhanced lateral epitaxial deposition (LED) mechanism that each cycle "knits" one row of atoms to the edge of the growing multilayer film. As a result of the lateral epitaxial deposition (LED) mechanism, the grown h-BN/EG heterostructures have good structural quality with highly ordered epitaxial interfaces, as summarized in the figure 2.21. It is desired in order to preserve the transport properties of pristine graphene. Atomic scale structural and energetic details of the observed row-by-row growth mechanism of the two-dimensional (2D) epitaxial h-BN film are analyzed through first-principles simulations, demonstrating one-dimensional nucleation-free-energy-barrierless growth. In conclusion, this industrially relevant LED growth strategy can be applied to a wide variety of van der Waals materials. [Gig20]

Summary

Significant progress in MOVPE growth of GaN based devices structures on h-BN epilayers has been made. New epitaxial growth technologies such as van der Waals epitaxy and remote epitaxy were explored using h-BN layers. Mixed dimensional heterostructures were realized using h-BN platform grown by MOVPE. On 3D-2D configuration high quality GaN based devices were demonstrated. Patterning induced drastically different BN allows selective area growth of GaN and resulted in local isolated devices structures. The modified front-end process applied on device structures on h-BN on patterned sapphire substrate showed respectable characteristics without degrading the structural integrity of the layers. On 1D-2D configuration, Dramatic self-assembly of GaN nanorods and nanoLED device structures growth was also demonstrated with blue light emission. Both these configurations, improves GaN material quality by reducing threading dislocation density and associated issues, avoids self-delamination occurring during the growth and front-end process and further process-free isolated devices. Exotic 2D-2D van der Waals heterostructures were also realized using dry transfer techniques using Ni sticker in wafer scale and high reproducibility. In addition, 2D-2D heterostructures was realized with MEMOVPE growth. The characterization performed on the device structures before and after liftoff showed that the structural, optical and electrical functionalities of the devices have been preserved or enhanced which is interesting for realizing Pick and Place assembly technology, which suits the next generation highly efficient and flexible opto-electronics devices. These studies have led to more than 15 peer reviewed publications in the last 5 years in highly reputed Journals and several international collaborations and funded projects.

3. *Novel* semiconductors - boron (III) nitride alloys.

3.1 Introduction

As described in the previous chapters, The growth of BN and boron-containing alloys of GaN and AlN has been a recent topic of interest. Diluting III-nitrides with boron adds much needed functionalities, and pushes the fundamentals limits of the III-nitride material system. It also improves the freedom to design this material for bandgap and strain engineering. Significant progress includes the first reports of BGaN and BAlN use in devices, specifically, gas sensors [Bis15], HEMTs [Rav12], and BAlN & BGaN/GaN Bragg reflectors [Abi11] [Li15]. Additional applications can be envisioned, but they will require thick materials possessing a quality that exceeds the current state-of-the-art. For example, the boron-10 isotope has a very high thermal neutron capture cross-section, so a BGaN or BAlN diode is effectively a monolithic direct conversion neutron detector [Ats14]. Future applications can also take place within existing devices, where boron can be added to GaN or AlN to increase resistivity [Bag09], which may be useful in betavoltaic applications, or for bandgap and strain engineering of quaternary III-N alloys [Oug08] [Aka07].

An awareness of the device potential of BGaN motivates a brief review of the challenges of growing BGaN materials of high quality. The small size of boron relative to gallium or aluminum and the high bond strength between boron and nitrogen is the cause of large strain resulting in a very large immiscibility gap for BGaN and BAlN. This manifests in a strong tendency for phase separation. Additionally, BGaN and BAlN nano-clusters tend to form in the other than wurtzite phase, impacting uniformity [Gau11]. At larger scales these growth dynamics have resulted in layers which consist of random multi-crystalline nanocolumns strongly aligned to the preferred growth axis.

To mitigate these issues, we have employed several growth strategies some of them are reviewed below.

3.2 Growth of BAlN for lattice and bandgap engineering

A small amount of boron incorporation in AlN can introduce a strong refractive index contrast along with lattice matching with SiC substrates. This is of great interest for high reflectivity III-N DBRs in the deep UV region. Flow-modulated epitaxy (FME) was used to grow this new class of material, the feeding sequences of precursors during the growth was shown in Figure 3.1: 2 s supply of metalorganics and 1 s supply of NH3 were alternatively run into the reactor.

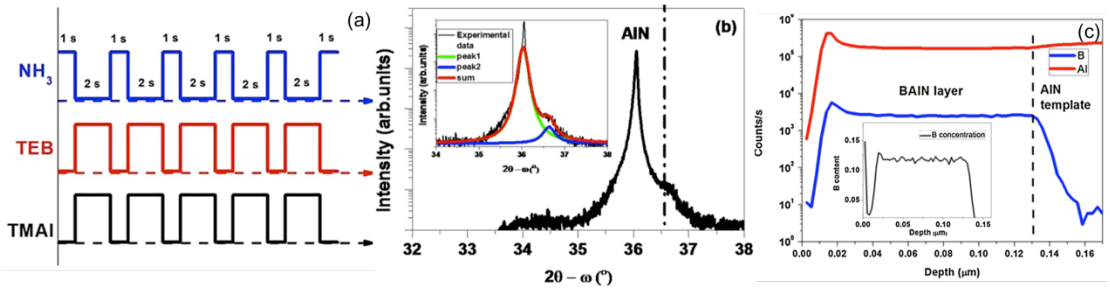

Figure 3.1: (a) Feeding sequences of precursors for flow-modulate epitaxy method. (b) HR-XRD of 70nm BAlN on: AlN template by FME growth (TEB/III=39%). Inset figures show the smoothing and deconvolution of two peaks. (c) SIMS elemental concentration depth profiles of B and Al for the sample grown on AlN template; the inset shows the boron concentration obtained by using boron implanted AlN as calibration sample. Ref. [Li15]

BAlN alloys with crystalline quality beyond the state of art, as shown in the Figure 3.1(b) and record for highest boron incorporation as confirmed by SIMS measurements (12%-B) (Figure 3.1c) on GaN and AlN templates was obtained using this technology [Li15].

3.3 Growth of BAlN/AlN heterostructure

The fabrication of heterostructures of Boron based alloys with AlN or GaN is an important approach which needs to be further developed irrespective of their

applications, for example, BAlGaN based MQWs or for DBRs. This approach may mitigate intrinsic issues in the boron-based materials. A 5-period AlN/BAlN layers (25 nm / 32 nm) were grown on the AlN templates that are appropriate substrates for deep UV applications. Flow modulated epitaxy (FME) was applied during the growth of BAlN layers in order to enhance the migration of B and Al atoms, and also suppress parasitic reactions whereas the AlN layers were grown in a continuous way. The boron concentration in the BAlN layers along growth direction was evaluated by SIMS profile, as shown in Fig. 3.2(a). It was clear that B profile varies anti-phase with Al, which indicates that boron atoms substitute aluminium atoms on the III sites of the lattice to form an alloy. The average boron content distribution along the growth direction is presented in Fig. 3.2(b). Under our growth conditions, 11% (± 0.6%) boron incorporation has been obtained.

In order to investigate structural quality of this heterostructure and also crystalline characteristics, the cross-section STEM was performed along ⟨1 1 -2 0⟩ zone axis. As shown in Fig. 3.3(a), the bright-field STEM image shows that the AlN/BAlN heterostructure has columnar polycrystalline features, such as the part in the rectangle box. By looking into the higher magnification image of the interface between 1st AlN and 1st BAlN in Fig. 3.3(c), it is clear that the 1st AlN layer is still monocrystalline. When BAlN (with 11% boron) growth starts, the lattice is oriented along c-axis for around 5 nm, and then the tilt as large as 60° can be observed that means the structure tends to be polycrystalline and columnar growth starts.

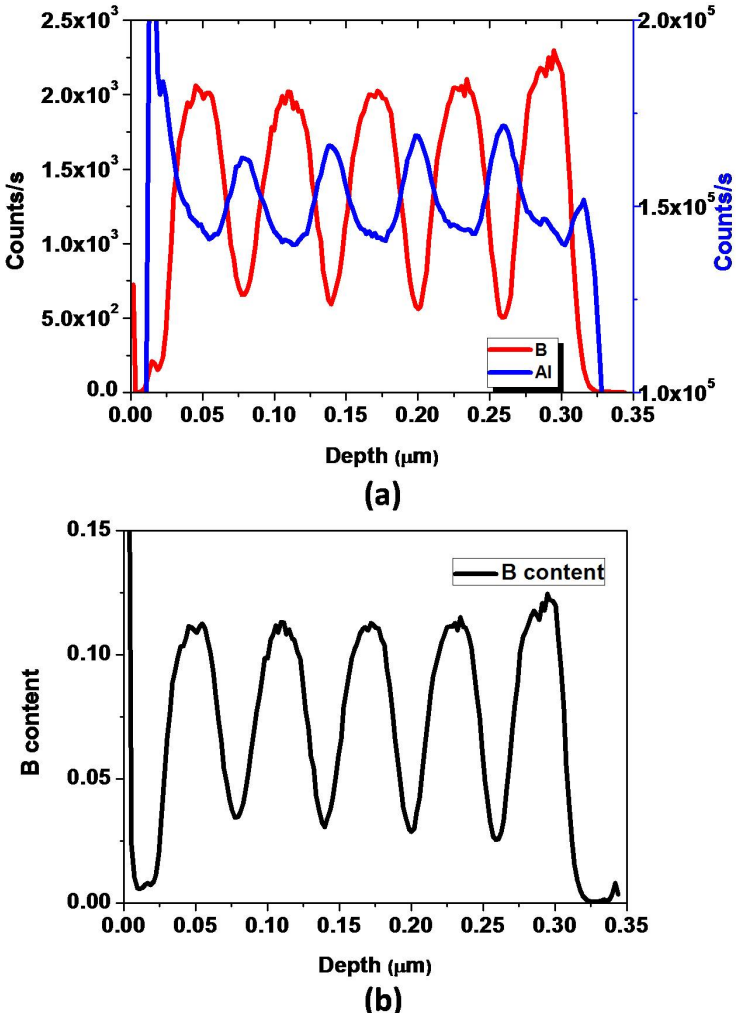

Figure 3.2: (a) SIMS elemental concentration depth profiles of B and Al for the sample grown on GaN template; (b) Boron content in solid layers calculated from SIMS by using boron implanted AlN sample as reference.

Better contrast of AlN and BAlN layers can be observed by Z-contrast High angle annular dark field (HAADF)-STEM image shown in Fig. 3.3(b), where layers with higher brightness represent AlN layers and darker layers represent BAlN. The surface roughness height caused by this columnar feature is around 10∼13 nm from STEM images. The polycrystalline feature has been confirmed by HR-XRD results also. The polycrystalline feature is caused by the short diffusion length of boron atoms, which would challenge the applications of this material.

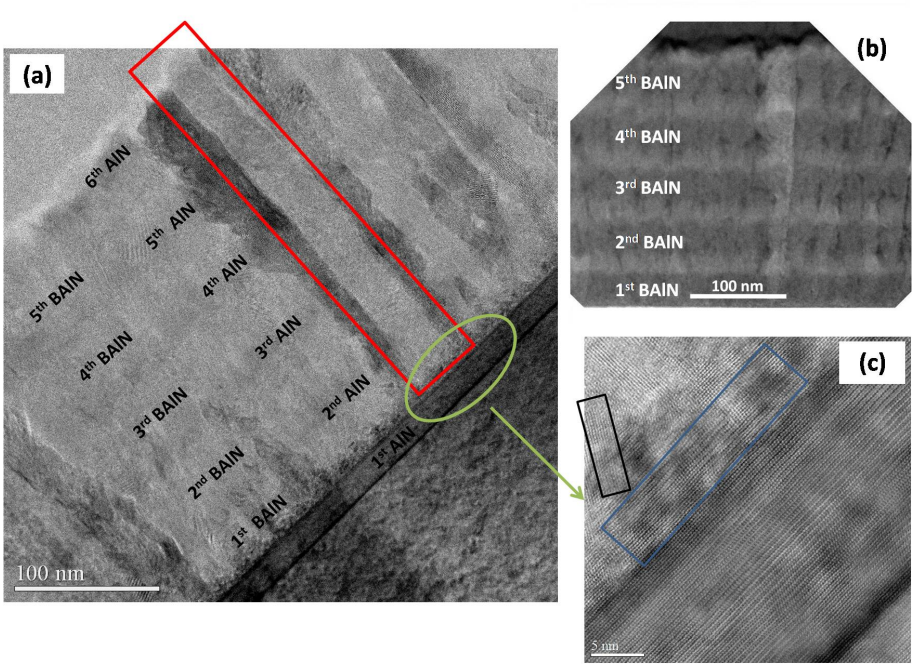

Figure 3.3: (a) STEM images (bright field) of 5-period AlN/BAlN heterostructure and columns are clearly observed in the structure; (b) HAADF-STEM image to show better contrast of BAlN and AlN layers; (c) high magnification of the zone where the 1st BAlN layer starts to grow.

From STEM image, it was observed that good periodicity of two different layers has been achieved. The monocrystalline critical thickness for BAlN with 11% boron is around 5 nm, above which the polycrystalline growth occurs. Meanwhile, the monocrystalline critical thickness is around 500 nm for BAlN of 2% boron as reported in the literature [Aka06]. The more boron is incorporated, the monocrystalline BAlN thickness is smaller. Therefore, for different applications, a compromise can be achieved between thickness and boron composition. For example, for deep UV distributed Bragg reflectors (DBRs), boron incorporation no more than 5% is enough to achieve high refractive index contrast theoretically [Abi12] [Wat03]. Hence, it can be an option to reduce the boron content and maintain BAlN layers (30~40 nm) monocrystalline. For ultra-thin layers such as MQWs or strain engineering superlattices, higher boron incorporation can be used allowing a large design freedom and it can still be kept as monocrystalline for its thin thickness (below 10 nm).

3.4 Realization of BAlN/Al(Ga)N DBRs for DUV

This section describes the realization of BAlN/Al(Ga)N DBRs. Related characterizations were performed and analyzed. The influences of increasing TEB/III ratio for BAlN layers on structural and optical characteristics of DBRs as well as the influences of replacing AlN layer with AlGaN were studied. The experimental results are also compared with the simulations by using parameters determined from characterizations. The previous sections analyzed structural features of BAlN layers grown by FME method. It is concluded that by FME method, crystalline quality can be improved since the grain size is increased and columns are formed. But in this case, the interface of BAlN and AlN layers would be destroyed, which can be a disastrous for DBR. For example, the structure of 5-period BAlN (32 nm) / AlN (25 nm) didn't have any reflection peak at around 260 nm as it is supposed to. To realize a DBR, more than crystalline quality the interfaces quality is important, hence the structure grown at 1000 °C simply in a continuous way, where the BAlN layer is nanocrystalline and the small-size crystallites that maintain acceptable interface as well as a clear contrast between two materials are suitable for this application. here, the DBRs for DUV region were realized under continuous flow condition.

Firstly, a series of 18-pair BAlN/$Al_{0.72\sim0.76}Ga_{0.28\sim0.24}N$ DBRs have been grown. The average growth rate for the BAlN/AlGaN structure is around 2 μm/h. Different TEB/III ratios were used for BAlN layers in order to study the influence of boron incorporation on the performance of DBRs. DBRs were also grown with a lower growth rate of 500 nm/h, since the low growth rate can increase the mobility of Al and B elements, and hence improve the homogeneity and interface abruptness. The RMS roughness is around 9 nm over 20 × 20 μm^2 while the RMS of similar structures grown at 2 μm/h is around 16 nm. The experimental reflection spectra along with the

simulations of three DBR structures are summarized in Fig. 3.4. The simulations here only considered ideal case without roughness or strain, and the comparison between experimental data and simulations considering quality factors would be demonstrated in the next subsection. The composition and thickness of AlGaN layers were determined by XRD. The composition and thickness of BAlN were determined by EDX (next subsection) and approximate calculation from reflection peak wavelength (the optical thickness of each layer should be one quarter of the central reflection wavelength).

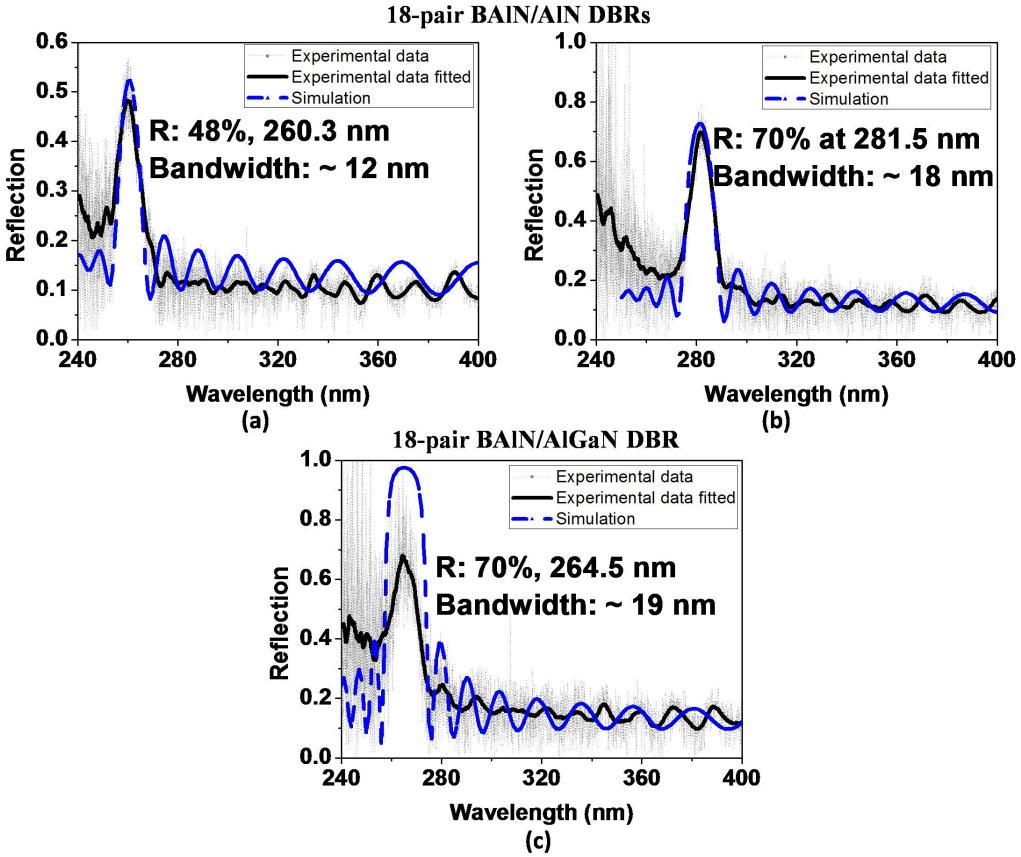

Figure 3.4: (a) 18-pair BAlN (29 nm) / AlN (29 nm) DBRs reflecting at 260 nm; (b) 18- pair BAlN (33 nm) / AlN (32 nm) DBRs reflecting at 280 nm; (c) 18-pair BAlN (33 nm) / $Al_{0.8}Ga_{0.2}N$ (24 nm) DBRs reflecting at 265 nm.

For BAlN/AlN structures, the experimental results are very close to the simulations. From central wavelength of 260 nm to 282 nm, the reflection was increased from 48% to 70%. At central wavelength of 260 nm and 265 nm, by replacing

AlN with $Al_{0.8}Ga_{0.2}N$, the reflection was also increased from 48% to 70% and the stopband width was increased from 12 nm to 19 nm (more than 50%) which confirmed better performance of BAlN/AlGaN structure than BAlN/AlN structure.

3.5. Boron rich BAlN alloys

Boron rich BAlN alloys with Al content varying from 0-25% in BN have been explored experimentally. Boron rich B(Al)N alloys system on the other side also enables desirable bandgap and lattice/strain engineering for applications. For example, thicker h-BN based alloys can switch into a direct bandgap material through strain engineering or alloying with Al, which would enhance emission efficiency in the deep UV for UV LEDs. A single crystalline boron rich BAlN alloys was achieved with the Al content up to 17%. The surface of these alloys exhibits the honeycomb wrinkled morphology features upto 17% of Al in BAlN. Above this Al content, the presence of wurtzite Al rich BAlN secondary phases in a matrix of layered hexagonal B rich BAlN was observed as shown in the figure 3.5 (SEM images).

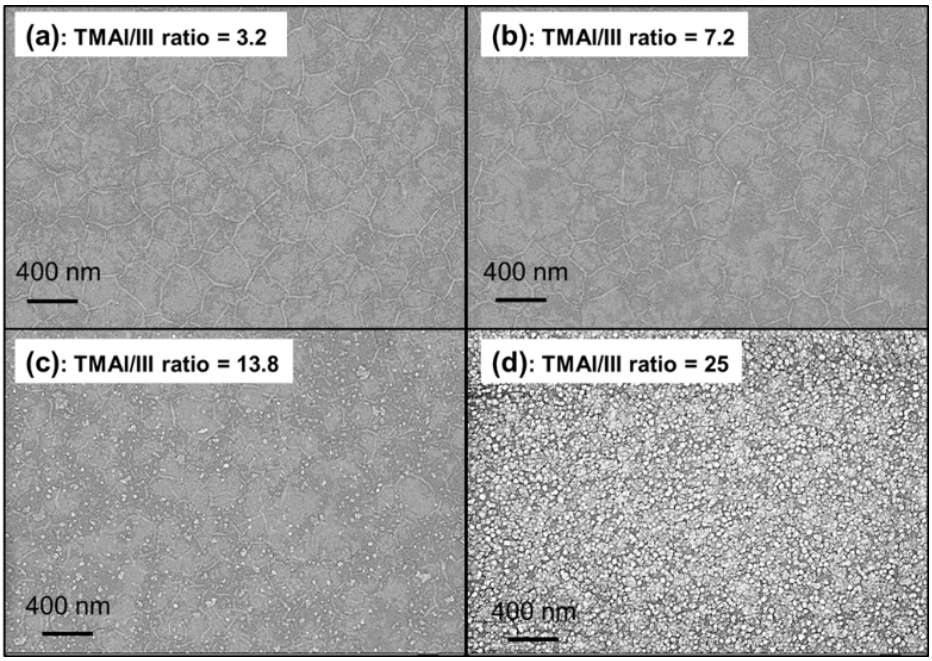

Figure 3.5: SEM images of BAlN alloys grown on sapphire with four different TMAl/III ratios. (a) 3.2, (b) 7.2, (c) 13.8, and (d) 25. Ref. [Vuo20]

To estimate the efficiency of Al incorporation in our BAlN alloys, secondary-ion mass spectrometry (SIMS) measurements were performed using molecular ions Cs+. Figure 3.6 (a) shows SIMS elemental concentration depth profiles of aluminium atoms in BAlN alloys with five different TMAl/III ratios. At the TMAl/III ratio of 25, the Al concentration reaches to the same level with the one derived from sapphire substrate (30-40 nm depth) due to the phase separation as demonstrated by HR-XRD. Figure 3.6 (b) plots the estimation of Al composition from 0% (pure h-BN) to 100% (pure w-AlN) as a function of TMAl/III ratio. We obtained the Al content of 1%, 3.5%, and 17% for the TMAl/III ratios of 3.2, 7.2, and 13.8, respectively. In case of the TMAl/III ratio of 25, the Al content is found to be almost 100%. To interpret this, our experimental data were fitted by using the Lorentz function (green solid line in figure 3.6 (b)). At low TMAl/III ratio (≤ 14), the fit gives a good agreement with our data, confirming the enhancement of Al incorporation when the TMAl/III ratio is increased. However, when the TMAl/III ratio is higher than 25, the Al composition starts to be saturated. We attribute that due to the phase separation between BN and AlN as also investigated by HR-XRD. Therefore, in this study the maximum composition of Al in BAlN without phase separation is up to 17%.

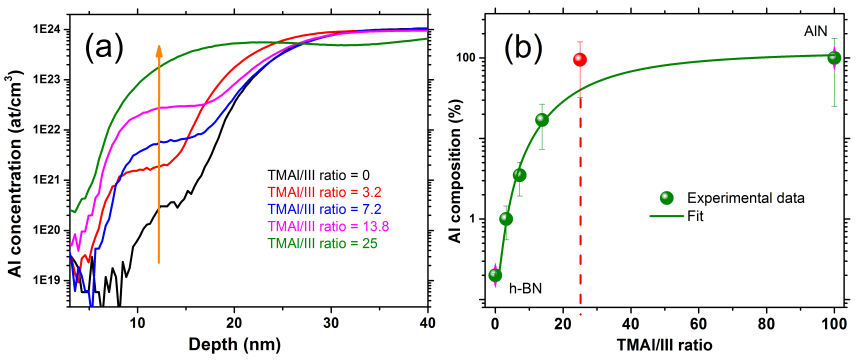

Figure 3.6: (a) SIMS elemental concentration depth profiles of Al for the BAlN alloys grown on sapphire with four different TMAl/III ratios; (b) Al composition as a function of TMAl/III ratio. Ref. [Vuo20]

Transmission spectroscopy was utilized to investigate the bandgap variation in the BAlN layers. Figure 3.7 (a) shows transmission spectra, which were recorded at room temperature for the three different Al compositions of the BAlN alloys. All spectra recorded for different BAlN samples exhibit a shift to higher wavelengths with an increase in Al incorporation.

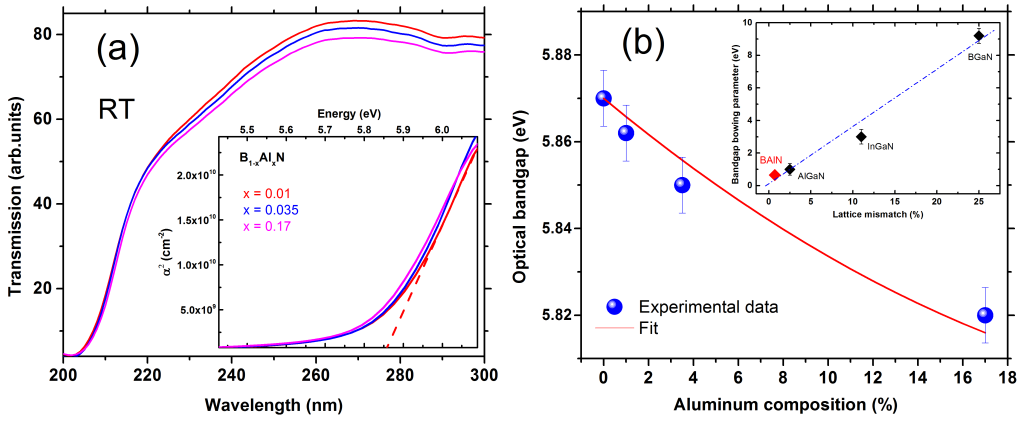

Figure 3.7: (a) Transmission spectra of the BAlN grown on the sapphire substrate with different Al compositions. Inset: the squared absorption coefficient (α2) vs photon energy for estimating energy bandgap; (b) Bandgap variation vs Al composition. Inset: bandgap bowing parameters for nitride compounds vs the lattice mismatch between the end point binaries. Ref. [Vuo20]

A well-defined linear behavior is observed in the high-energy side (dashed line in the inset of figure 3.7 (a)). The optical band-gap of these samples was estimated based on the basic equation: $\alpha^2 = \alpha_0^2(E - E_g)$. We obtain a shift to lower energy from 5.86 eV to 5.82 eV when the Al content is increased from 1% up to 17%. The red-shift of band-gap in our alloys can be understood using band-gap bowing concept. Figure 3.7 (b) plots our estimated band-gap of BAlN alloys versus the Al composition (blue sphere) together with the fit (red line) using a modified Vegard's law:

$$E_g = (1 - x)E_g^{h-BN} + xE_g^{w-AlN} - Cx(1 - x)$$

with C is the bowing parameter. In our fit, the band-gap of AlN = 6.12 eV [Liu18], the optical gap of h-BN = 5.87 eV [Li16], and we obtained the bowing parameter C = 0.65

± 0.05 eV. The relatively low value of C in BAlN may be attributed to the small difference between the indirect gap of h-BN and the direct gap of AlN. Thus, the alloy bandgap exhibits only small deviation from linear interpolation. The inset of figure 3.7 (b) illustrates the general trend for the bandgap bowing parameter in the III-nitride alloys systems by presenting C value versus the lattice mismatch between the end-point binaries: AlGaN (C= 1eV [Vur01]), InGaN (C = 3eV [Ors14]), BGaN (C = 9.2 eV [Oug08]) and BAlN. Our experimental value of C = 0.65 ± 0.05 eV, thus is in a reasonable range of the bowing parameters for nitride compounds.

Very recently, Al atoms diffusion into h-BN were found to anchor layered h-BN on to the sapphire substrates [Vuo20a]. In addition, it was found that mechanical transfer characteristics of BAlN sample got altered with Al concentration. Detailed structural analyses of these samples along with other AlN/BN/sapphire heterostructures were performed using TEM measurements to explore the lift-off mechanism. The effect of Al concentration into h-BN layers on the mechanical lift-off is verified by studying carefully BAlN alloys with different Al contents. It has been observed that for an Al content above 17%, the layered BAlN sample cannot be lifted off. The control of the mechanical adhesion of different heterostructures and device structures such as HEMT-based on h-BN layers has been examined to confirm the role of Al diffusion on controlling the lift-off of the subsequent device structure grown on h-BN and reported [Vuo20a]. This approach solves critical issues like spontaneous delamination during growth and post-growth treatments and further extends its applications.

3.6 BGaN Nanostructures

Even though the quality of these diluted III-nitrides is still in its infancy and needs tremendous improvement, these materials were employed in the device structures showing greater improvements in its performances. For example, sensors made with BGaN based superlattices showed greater sensing and better recovery than its pristine counterpart. To circumvent the intrinsic problems and associated growth issues, in BGaN growth such as phase separation, surface roughness and columnar growth, nanoselective area growth technology was adapted.

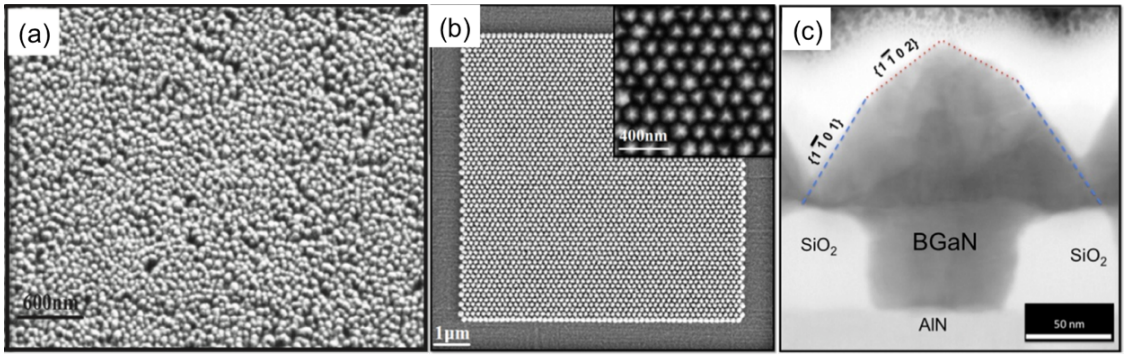

Figure 3.8: (a) SEM image of BGaN on AlN/Si templates showing 3D growth. (b) Perfectly selective NSAG BGaN on the 10x10 μm2 mask-patterned AlN/Si (111) template with insets showing higher magnification image of the BGaN nanopyramids. (c) Cross-sectional bright field STEM image of the single BGaN nanopyramids grown on the 10x10 μm2 mask pattern on AlN/Si(111), confirming its single crystalline nature. Ref. [Sun16]

Further details of this NSAG technology growth principles and associated mechanisms resulting in high-quality single crystalline thick materials are discussed in the InGaN growth for solar cell application section in chapter 4. In the unpatterned areas BGaN is stymied with 3D columnar growth as shown in the figure 3.8 (a). Using NSAG, Boron alloyed III-nitrides has been tailored to be dislocation free, single crystalline nanostructures using the NSAG as in the figure 3.8 (b) & (c) opening up new avenues for further research.

Summary

Here we demonstrate high crystalline quality BAlN materials up to 12% B incorporation and heterostructures. But for DBR applications this material is found to be not suitable hence the material has been tailor-made to have better interface by adjusting the growth conditions suitably. The DBR with 60% reflectivity at 280 nm has been demonstrated using this BAlN/AlGaN structures. Inaddition, the boron rich BAlN alloys have been successful grown by Metal-Organic Vapor Phase Epitaxy (MOVPE). The Al composition in the BAlN layer was estimated by SIMS to be up to 17%. The TEM study confirmed the layered nature in single phase BAlN alloys. It also revealed the presence of wurtzite Al rich BAlN phases in a matrix of layered hexagonal B rich BAlN. Band to band transition around 5.86 eV has been observed, which shifted slightly to lower energy with increasing Al incorporation. Apart from this progress in BAlN growth, NSAG has been explored to improve the quality of these boron-based alloys (BGaN) and investigate the fundamental properties. These studies have led to more than 6 peer reviewed publications in highly reputed Journals and several international collaborations and funded projects.

4. Tailoring InGaN alloy based new generation devices

4.1 Introduction

With conventional photovoltaic materials reaching their theoretical performance limits, a bottleneck has formed, and new materials and new concepts are required to provide the impetus for a break-through. Already a key material for the optoelectronic industry [Nak00], indium gallium nitride (InGaN) is now being actively investigated for solar-cell applications. The ability to match twice the spectral range of its competitors as shown in the figure 4.1, and an absorption coefficient ten times higher than the best alternatives, help make InGaN one of the most promising photovoltaic materials currently known. Theoretically, a single junction cell (Eg = 1.1eV) can reach 31 % conversion efficiency and a Multijunction cell can exceed 60% efficiency. However, to absorb 90 % of the incident sunlight as shown in the figure, 200 nm thick high-quality indium rich InGaN is needed, which is almost an order above the critical thickness of the pseudomorphically strained InGaN that can be grown on GaN.

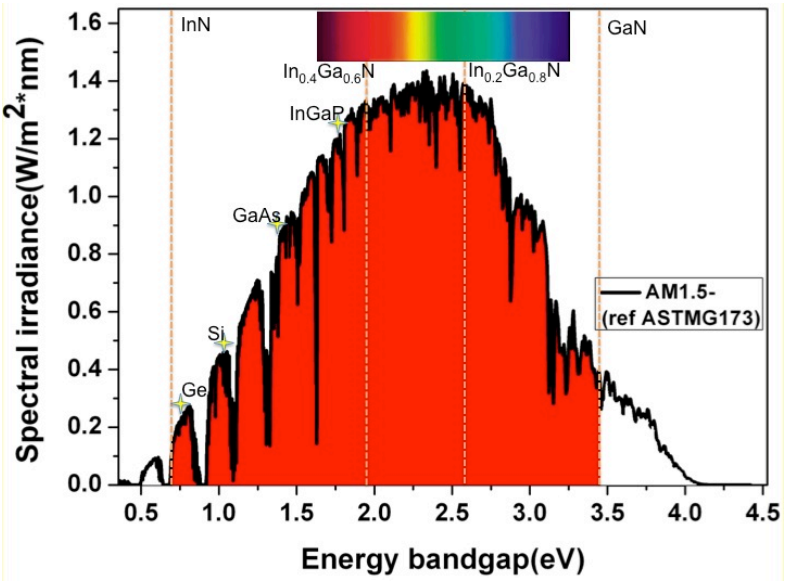

Figure 4.1: Photon Energy vs. Spectral irradiance plot of the AM1.5G solar spectrum.

4.2 Thick InGaN based new generation of solar cells

Despite technological advances that include the growth InGaN epilayers with compositions over the whole range [Liu11] [Shi09] [Hor02] and the demonstration of p-type conductivity with hole concentrations up to 2×10^{19} cm^{-3} [Yu09] [Isl09] [Hor09] [Pan09] [Pan10] [Sas11], InGaN solar cells are still at the early stages of their development. Indeed, state-of-the-art solar cells contain no more than 12 % indium and InGaN layers that are no thicker than 60 nm [Mat11] [Lan11]. While these devices still display internal quantum efficiencies (IQE) as high as 97% and external quantum efficiencies (EQE) as high as 70 %, there is still many ways to go until InGaN-based solar cells that take full advantage of the properties of the InGaN material system are demonstrated.

To fully understand the dynamics of the growth of InGaN, the bulk or thick InGaN layer with varying thickness were grown and studied first. For the purpose of this study, specimens were prepared from the 75 nm, 140 nm and 200nm thick InGaN samples. The ⟨1124⟩ RSMs of these three are reminded in Figure 4.2. Besides the intense diffraction from the GaN buffer, all three mappings present a diffraction spot corresponding to fully strained 12 % InGaN, and a diffraction spot corresponding to fully relaxed 23 % InGaN.

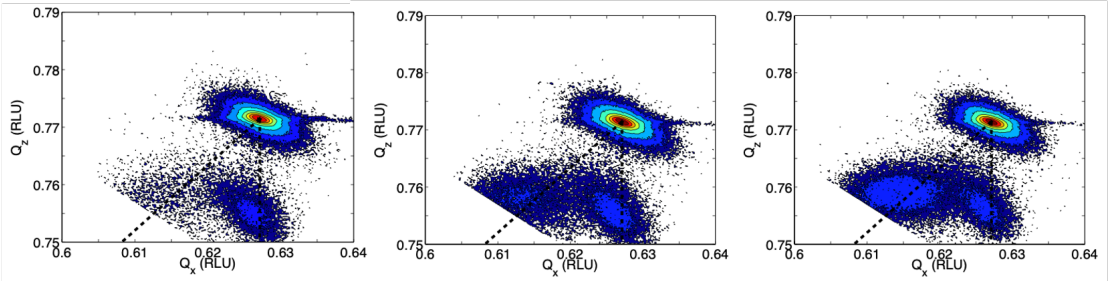

(a) 75 nm thick InGaN epilayer. (b) 140 nm thick InGaN epilayer. (c) 200 nm thick InGaN epilayer.

Figure 4.2: Reciprocal space maps (RSMs) of InGaN epilayers presenting double diffraction peaks.

The double diffraction peaks observed in thick InGaN epitaxial were associated with the presence of two distinct sublayers within the film as shown in the cross-sectional high-resolution transmission electron microscope (HRTEM) images in figure 4.3. The first sublayer (InGaN #1), located near the GaN/InGaN interface, has a homogeneous distribution of indium and is pseudomorphically strained on the underlying GaN buffer. The second sublayer (InGaN #2) has a laterally inhomogeneous composition, is fully relaxed, and exhibits three-dimensional growth.

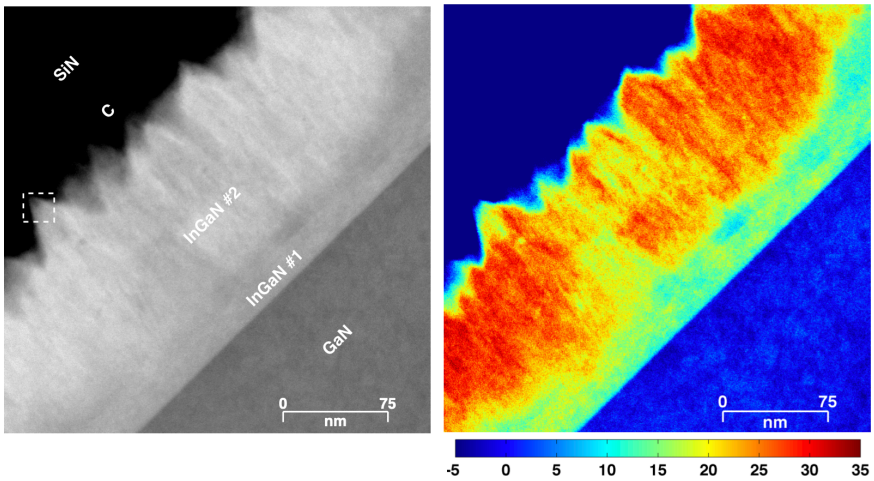

(a) Dark-field image (b) Composition mapping

Figure 4.3: Dark-field image and corresponding composition mapping of a 140nm InGaN epilayer presenting both InGaN #1 and InGaN #2 sublayers.

In the literature, the transition from InGaN #1 to InGaN #2 has been associated with a discontinuous strain relaxation of the InGaN #1 sublayer [Sin97] [Nad98]. Based on this hypothesis, the short-scale lateral variations of the Z-contrast observed in dark-field images of the InGaN #2 sublayer were attributed to the presence of misfit dislocations. Even though the critical thickness of InGaN is low, it was reported that $In_{0.12}Ga_{0.88}N$ with upto 60 nm thick can be grown without considerable relaxation induced phase separation [Mat11]. Following this, A thick InGaN layer is sandwiched between a p-type GaN (Magnesium doped) and n-type GaN layers to form the complete PIN solar cell structures as shown in the figure 4.4. A 10 nm non intentionally doped

(NID) GaN cap layer (to stop the diffusion of Mg from the p-GaN layer into the intrinsic region) followed by a 200 nm thick Mg doped p-type GaN and a 50nm of heavily Mg doped p-type GaN were grown at 800 °C. The p-GaN growth temperature was lowered considerably to reduce InGaN decomposition during growth. The solar cells composed of these InGaN absorber resulted in a peak external quantum efficiency of 79% as shown in the figure 4.5 (a).

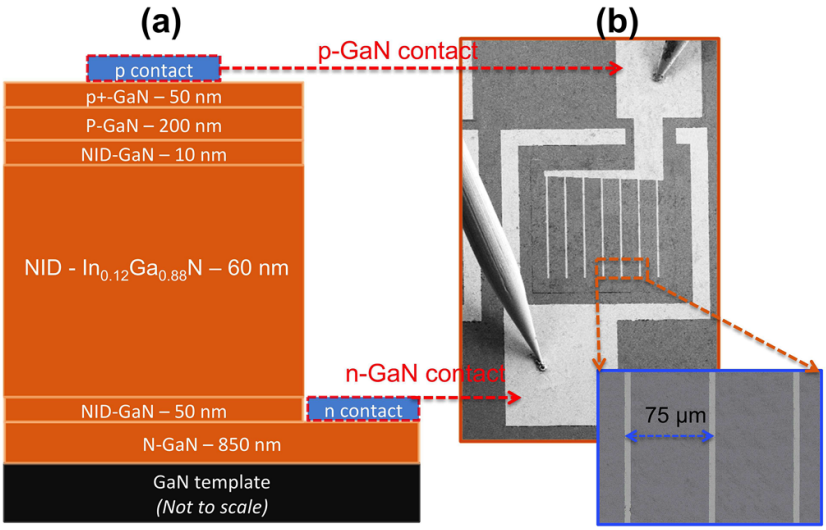

Figure 4.4: (a) Device cross-section of bulk based InGaN PV cell (T1185-B), with corresponding thickness and indium concentration for each layer, (b) SEM image of the device, showing p-GaN and n-GaN contacts, inset shows the adjacent grid spacing of 75 µm.

Fig. 4.5(b), which shows the J - V dependence measured under AM 1.5G conditions, a value of 2.56 mA/cm^2 for Jsc can be determined, which is the maximum value ever reported for a PIN heterojunction solar cell, with a 60nm thick $In_{0.12}Ga_{0.88}N$ absorber layer. We obtain larger Jsc and EQE, but lower Voc and Fill Factor, when compared to Matioli et. al. High density of deep V-pits mostly due to low temperature p-GaN growth leads to high leakage current [Mat11], hence reducing both the open circuit voltage and fill factor, the overall power conversion efficiency was 0.49% [Ari16].

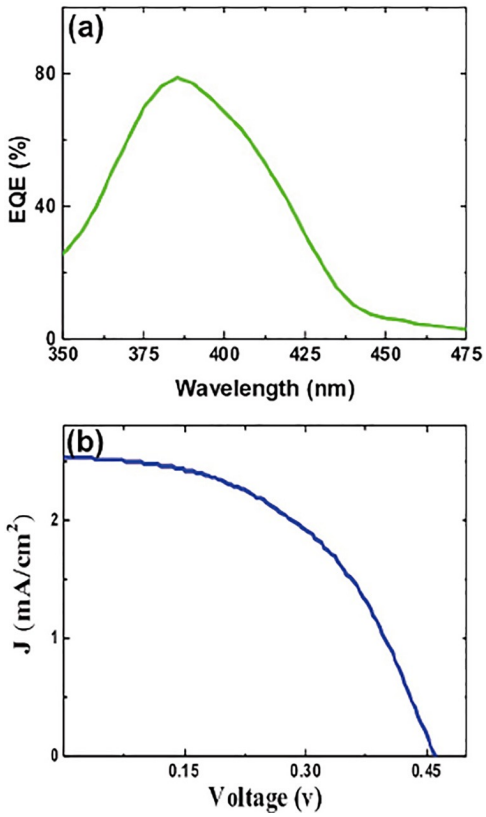

FIG. 4.5. (a) EQE spectrum and (b) corresponding J–V dependence measured under the AM 1.5G solar spectrum Ref. [Ari16].

It is clear from the above investigation that the material quality of thick InGaN epilayers plays a detrimental role in the solar cell performances and is still a major technological bottleneck. Because of which the devices suffer from high background concentration, low minority carrier lifetime, high leakage current, open circuit voltage collapse and other associated problems.

Interestingly, the deep structural studies show that despite the transition from two-dimensional to three-dimensional growth, the initial InGaN #1 sublayer remains homogenous and pseudomorphically accommodated to the underlying GaN buffer. This high-quality layer is suitable for photovoltaic applications. Thus, it would be desirable to devise a method to suppress the transition to InGaN #2 and promote the growth of InGaN#1. One such method is described in the following section.

4.3 InGaN Semibulk based solar cells

A semibulk approach was adapted to grow thick InGaN absorbers that may overcome the issues of phase separation and high dislocation density in the InGaN and thus grow InGaN-based PIN solar cells with improved properties. The approach consists of replacing the conventional bulk absorber by a thick multi-layered InGaN/GaN absorber as shown in the figure 4.6. The periodical insertion of the thin GaN interlayers should absorb the excess indium and relieve compressive strain [Pan13] [Elg13].

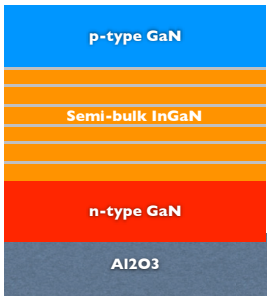

Fig. 4.6. schematic structure of semi-bulk InGaN.

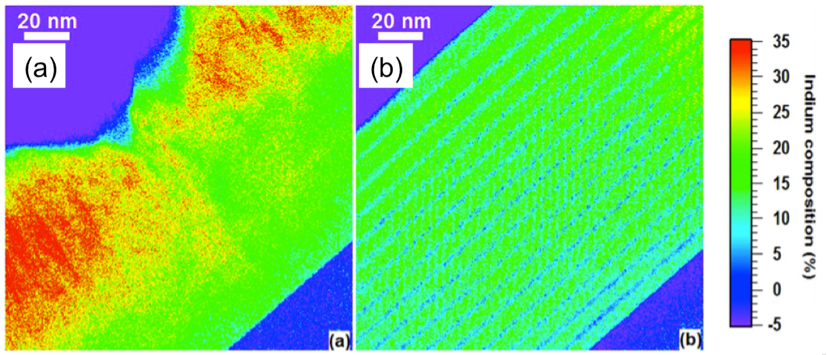

Figure 4.7: (a) Nanometrically resolved mappings of the indium composition. The mappings were obtained from the HAADF-STEM images of (a) Bulk InGaN and (b) semi-bulk InGaN samples.

These GaN interlayers need to be thick enough to be effective and thin enough to allow carrier transport through tunneling. The InGaN layers need to be thick and numerous enough to absorb efficiently the incoming light beam, and thin enough to remain fully strained and without phase separation. The growth of semibulk InGaN

prevented the transition from two-dimensional to three-dimensional growth observed in bulk InGaN, resulting in a high quality, thick, epitaxial InGaN layer. The surface morphology is completely 2D which is desirable for processing of devices. HAADF-STEM images of such a bulk and semi-bulk sample are shown in figure 4.7 (a) & (b). The images confirmed that the observed composition inhomogeneity in bulk InGaN along with 3D transition is absent in the semibulk InGaN.

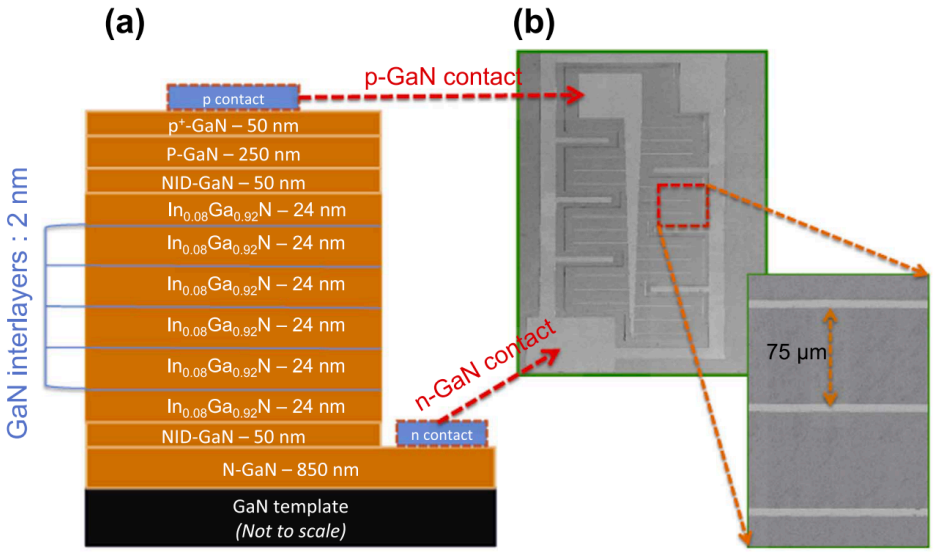

Fig. 4.8 (a) Device cross-section of semibulk based InGaN PV cell, with corresponding thickness and In concentration for each layer, (b) SEM image of the device, showing p-GaN and n- GaN contacts, inset shows the adjacent grid spacing of 75 µm.

Based on this Semi-bulk InGaN, PIN solar cells structure as shown in figure 4.8(a) was grown on GaN templates. The semibulk structure consisted of 6 periods of 24 nm $In_{0.08}Ga_{0.92}N$/2 nm GaN both grown at 800 °C. A 50 nm thick low temperature NID-GaN layer is grown at 800 °C above the semibulk absorber in order to protect InGaN layer during high p-GaN growth temperature and as a set-back layer to reduce Mg diffusion into the absorber. Finally, a 250 nm thick p-GaN layer that has been lightly doped with Mg followed by a heavily doped p+-GaN layer are grown at 1000 °C.with record internal quantum efficiency around 85% as shown in the figure 4.9 and highest

current density in that class of solar cell have been demonstrated [Ari17].

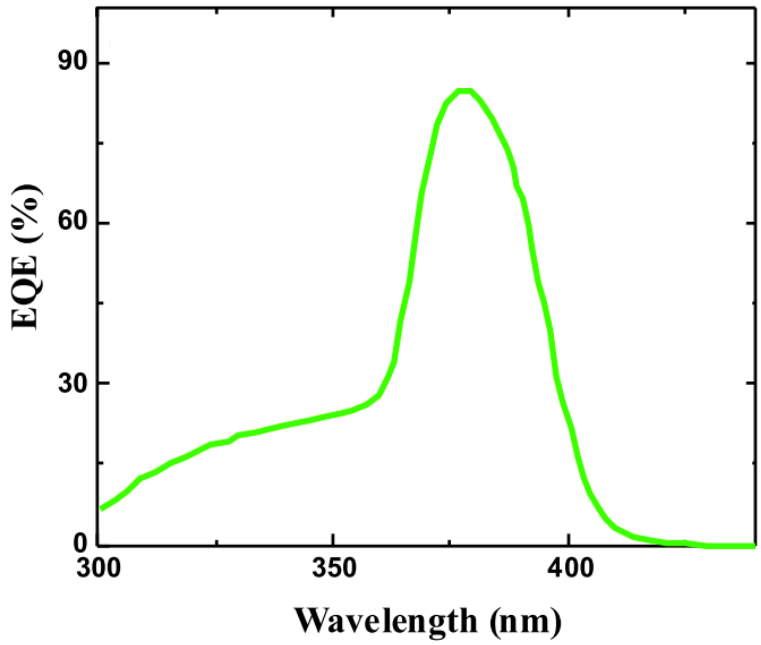

Figure 4.9: Typical EQE recorded in the semibulk based PV cell Ref. [Ari17] .

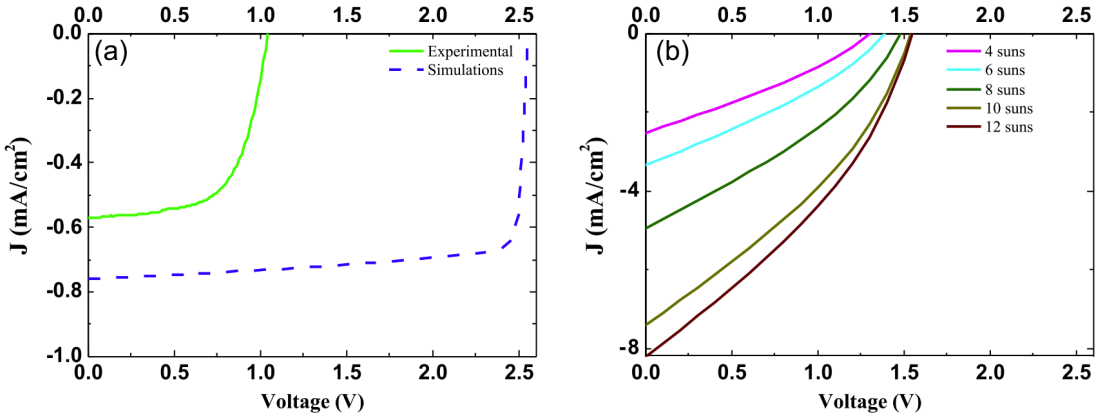

Fig. 4.10. (a) Measured and simulated J-V obtained under AM 1.5 G, and (b) measured J-V obtained under concentrated light Ref. [Ari17].

The device has a maximum EQE peak of 85% as shown in the figure which is the highest EQE peak reported so far for an InGaN PIN heterojunction solar cell for InGaN absorber with 8% In in it. The J_{sc} measured and simulated under AM 1.5 G is shown in the figure 4.10 (a). The measured J_{sc} is almost four times as high as previously reported values for 8% In concentrations and thus confirms efficient light absorption

and photocarriers collection in the semibulk absorber. The device has a power conversion efficiency (PCE) of 0.39% under an AM 1.5 G solar spectrum, almost three times higher than the current state of the art devices with 8% In in the MQWs. The J_{sc} variation under concentrated light is shown in the figure 4.10 (b). The key finding is that solar cells based on semibulk absorber results in high PCE in-spite of high density of structural defects in p-GaN and partial degradation of top InGaN layer. The main limitation in PCE is due to the low Voc. Finally, these device results along with structural characerizations show that semibulk InGaN absorber structure is a promising candidate for achieving high efficiency InGaN heterojunction solar cells.

Semibulk approach controls very well the strain evolution induced degradation for InGaN upto considerable In composition. The thickness of InGaN the layer and number of periods is very important factor controlling the threshold In composition. Since the critical thickness of InGaN decreases with increase of In composition, a much lower thickness of InGaN has to be employed which is compensated by increasing the number of periods. These factors drive the semibulk very close to multiple quantum well (MQW) configuration which also has been reported to suffer from strain related degradation. An alternate route has been found to stop this strain related degradation at the InGaN/GaN interface itself in In rich InGaN which was extensively investigated in the following section.

4.4 Nano-Selective Area Growth (NSAG) of InGaN on GaN/sapphire

Nano selective area growth (NSAG) or nanoheteroepitaxy is a relatively new growth technique which can be used to grow misfit defects free nanostructures. In this technique the materials/nanostructures are grown selectively in a nanometer scale area, which reduces the nucleation density and give these nanostructures enough lateral

spacing to relax laterally as soon as it starts growing in the preferred growth axis thus eliminating lattice mismatch issues. In general, the relaxation occurs well before the critical thickness of the material at the interfaces because of which the strain energy saturates, controlling the strain related degradation which is not the case in other conventional epitaxial techniques as shown in the figure 4.11.

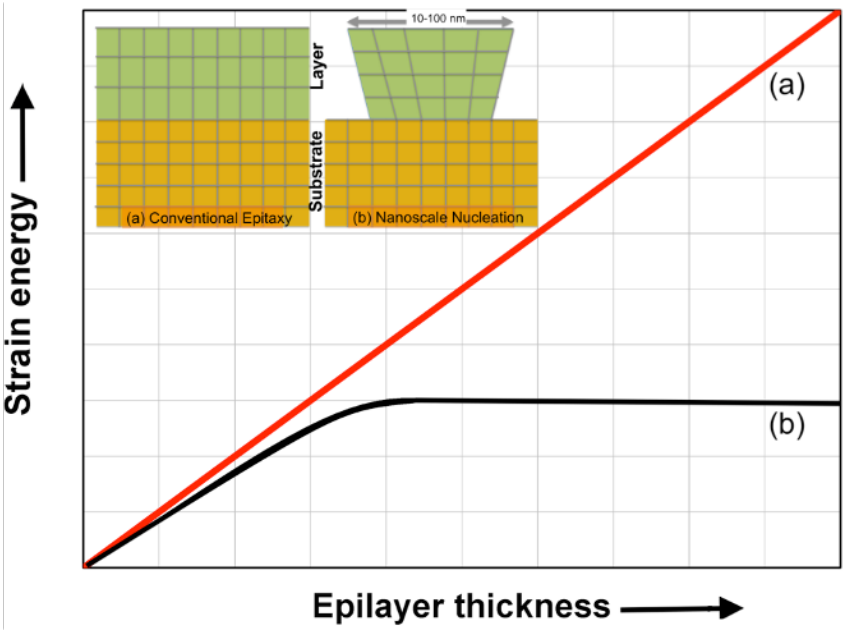

Figure 4.11: Variation of strain energy Vs epilayer thickness (a) under conventional heteroepitaxy and (b) under nanoheteroepitaxy. Inset shows the schematic of nanoheteroepitaxial process in comparison with conventional epitaxy. Ref. [Zub00]

NSAG addresses all issues related to InGaN such as lattice mismatch induced strain relaxation, phase separation, and transition from 2-D to 3-D growth resulting in InGaN epilayers with a large density of defects and In composition inhomogeneity. To grow selectively, this method involves a thin dielectric SiO_2 masks on the substrate/template surface that are patterned with nano-openings (10–100 nm) where nanostructures will be grown. In the present investigation, we have used a simple, industry friendly, single step e-beam patterning process using negative tone photoresist hydrosilsesquioxane (HSQ). The process flow is described in the figure 4.12. achieved

patterns with varying sizes from 10x 10 µm upto 100 x 100 µm matrix patterns with nanometer size opening as shown in the figure 4.12.

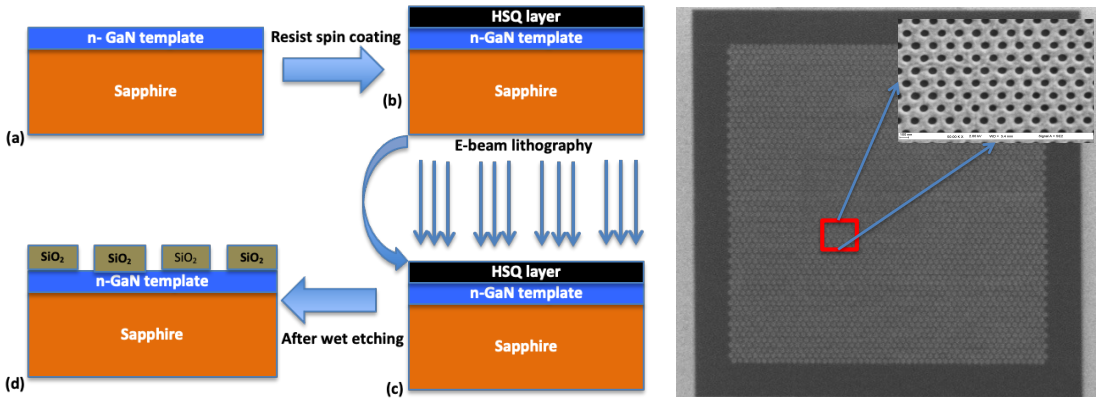

Figure. 4.12: (a-d) The process flow for realization of the SiO_2 patterns with HSQ and top view SEM image of the 10 x 10 µm patterned SiO2 mask on GaN template.

Thick InGaN epilayers (120 nm) was grown on these patterned templates using T-shaped MOVPE reactor. Trimethyindium (TMIn), trimethylgallium (TMG), and ammonia were used as the precursors for the growth. Growth temperature was 800°C under full nitrogen ambient. Fig. 4.13 shows SEM images of perfectly selective InGaN nanostructures grown on circular and stripe openings in the patterned substrate, respectively. As a result of optimized growth conditions, InGaN growth on the patterned area is perfectively selective, without any polycrystalline deposits on the masks. The pattern with circular openings contains InGaN nanorods which have a hexagonal pyramid shape. InGaN nanostructures exhibit well defined shape and size uniformity, exposing the six (1–102) triangular r-plane facets. The InGaN nanorods have smooth facets without any visible defects with inclusions and In clusters or trenches when compared to the InGaN in the unpatterned area as shown in the insets.

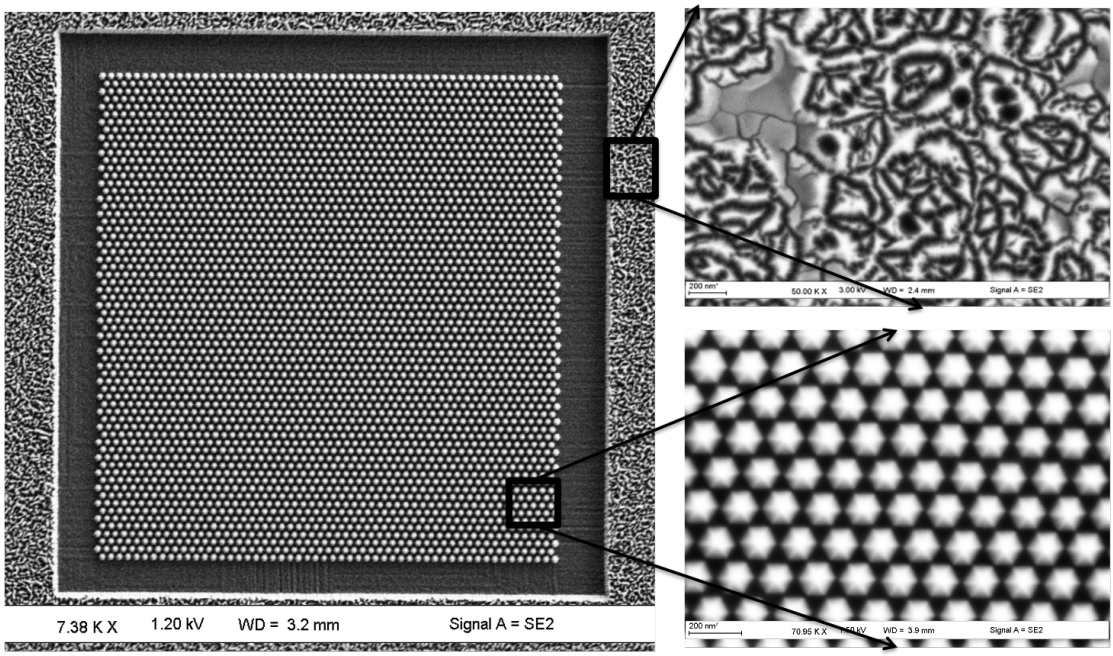

Figure 4.13: SEM image of InGaN nanopyramidal structures in the patterned area inset shows the higher magnification image of the marked patterned and unpatterned area which clearly shows the differences between the planar InGaN quality with inclusions and In clusters and InGaN nanopyramids without any visible defects on its surfaces. Ref. [Sun14] [Sun15b].

Deeper structural analysis with cross sectional transmission electron microscope was also carried out. Figure 4.14 shows different magnifications of HAADF STEM images of InGaN nanorods. The very good uniformity of the hexagonal pyramid shaped nanorods, the clear contrast between the 20nm GaN regrowth layer and 150nm InGaN, and the absence of threading dislocation emerging from the interfaces in the nanorods are all apparent. The high-resolution TEM image of one nanorod shown in Fig. 4.14 (d) clearly evidences that the InGaN nanostructure is single crystal and with its defect free growth mechanism NSAG is a very promising approach for realizing In rich InGaN. These nanostructures mitigate the propagation and generation of dislocations, as well as strain-related degradations and In clustering observed in planar InGaN.

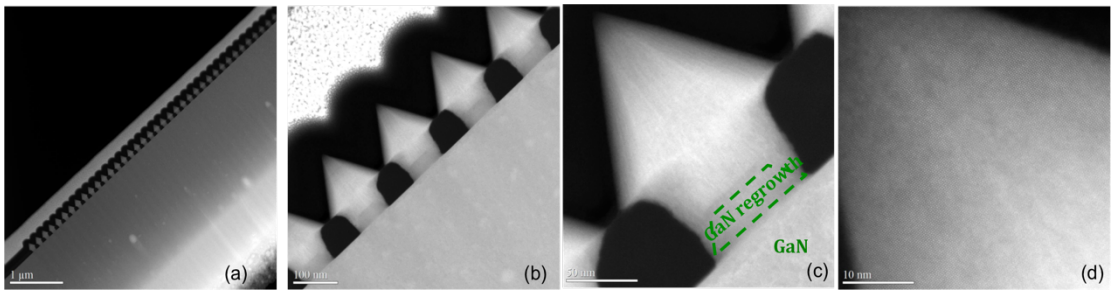

Figure 4.14. (a)–(d) Different magnifications of HAADF cross sectional STEM images of 150nm thick, and In-rich (up to 22%) InGaN nanorods.

The novelty lies in realizing precise patterns, avoiding cumbersome process steps and in preserving the seed layer quality. By adapting NSAG approach the intrinsic InGaN stress related problems have been mitigated, leading to high quality, dislocation free, compositionally uniform 150nm thick, and In-rich (up to 22%) InGaN nanorods as shown in the figure 4.14(a-d).

To enable low-cost applications, the device structures have to inevitably realize on the cheaper platforms like silicon, which also has better maturity. Nanoselective area growth (NSAG) yields high quality nanostructures independent of the substrates used, depending on the design of the nanopatterns. Using this advantage, thick InGaN nanostructures were grown on polycrystalline AlN buffered Si(111) templates. Detrimental strain related degradation in InGaN mentioned in previous section are even more pronounced in the case of planar InGaN layers grown on silicon, resulting in low crystalline quality and large compositional and morphological non-uniformity. With NSAG technology, dislocation free thick InGaN nanostructures with excellent selectivity on polycrystalline AlN/Si(111) and record 33% In incorporation in GaN was demonstrated as shown in the figure 4.15 (b) [Sun15]. The quality of the InGaN nanostructures was comparable with the nanostructures grown on GaN templates in figure 4.15 (a). This proof-of-concept result helps to overcome current limitations in

the growth of high quality InGaN nanostructured devices on low-cost III-nitride compatible substrates by MOVPE.

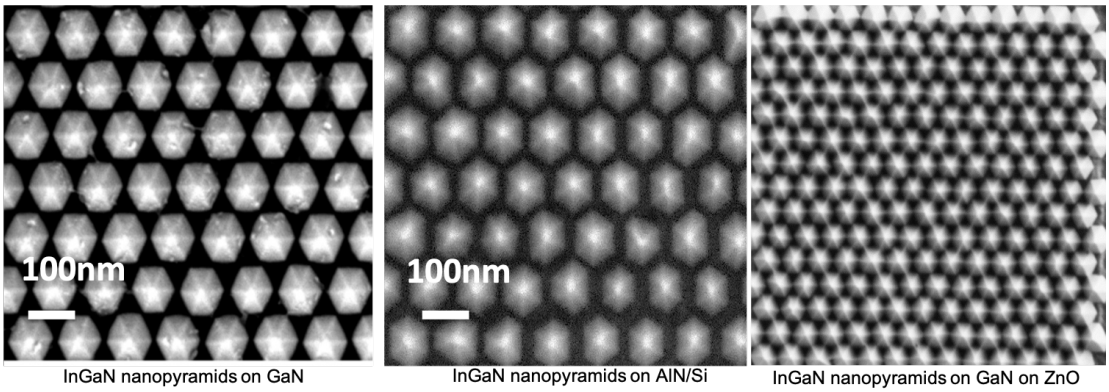

Figure 4.15: InGaN nanopyramids realized on different templates (ref [Sun15] & [Puy17]).

Using the same NSAG technique, defect free thick InGaN (22%-In) was grown on sacrificial ZnO/sapphire templates. Achieving selectivity of the InGaN on patterned ZnO/sapphire was challenging without the use low temperature GaN (growth of Low temperature (LT)-GaN on ZnO templates technology was also optimized by our group). This LT-GaN layer not only protected the sacrificial ZnO layer from degradation due to high temperature and ammonia rich ambient, simultaneously allowed the growth temperature to reach the normal InGaN growth temperature, which tremendously improved the growth selectivity. The quality of the InGaN nanostructures was analogous to the nanostructures grown on GaN templates as shown in the figure. This demonstration targets liftoff of this InGaN nanostructures by chemical etching of the ZnO sacrificial layer and further integration with multijunction solar cells for improving the conversion efficiency or on to other low cost or flexible substrates.

Given the expected high performances of InGaN, along with their industrial maturity, such devices are appealing for domestic photovoltaics, especially if made on silicon or other low-cost templates. Chemical lift-off (CLO) approach, is used to lift GaN thin films off of sapphire and GaN substrates to a low-cost soda lime glass by

means was demonstrated to achieve the above goal. This method is based on the ability to grow full p-GaN/i-InGaN/n-GaN structure on sacrificial Zinc Oxide (ZnO) underlayers. ZnO is much more susceptible to chemical etching than GaN so it can be preferentially dissolved and act as release layers for the GaN device structures. In this way wafer scale transfer of GaN and a few mm^2 of a full p-GaN/i-InGaN/n-GaN structure from sapphire and subsequent integration with glass was demonstrated without any crack formation by wet etching ZnO layers for high efficiency, low-cost next generation solar cells [Pan16].

4.5 InGaN nanopyramids based solar cell structures.

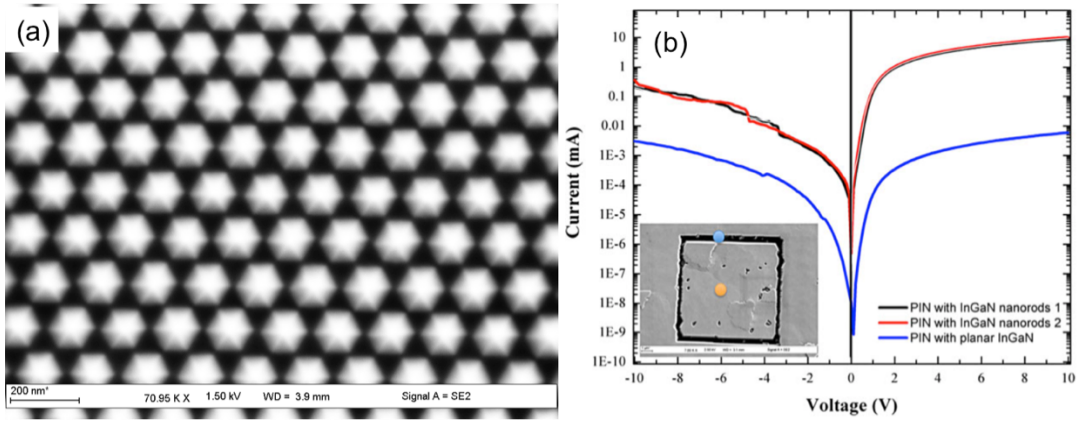

Figure 4.16: (a) Scanning electron microscope image of thick InGaN/ GaN grown on circular patterned GaN template. (b) I–V characteristics of the PIN structure with embedded thick InGaN nanostructures on GaN templates in comparison with planar InGaN PIN structure. Inset shows SEM image of the PIN structure in the patterned area, the blue and orange dots represent the point of contacts of n- and p-contact area after etching the sample with HF. Ref. [Sun15b].

Complete PIN structures embedding the dislocation free thick InGaN nanostructures on GaN templates as shown in the figure 4.16(a) was realized. First, GaN was grown under normal lateral regrowth conditions high growth temperature Low V/III, low pressure. No regrowth or low coverage of GaN on InGaN nanopyramids in figure 4.17 (a) was observed as shown in the fig 4.17(b). Hence, the growth conditions for the covering the nanopyramids were modified to have complete coverage

of the nanopyramids [Gib04]. Addition of Mg in the vapor phase enhances the L_R/V_C, ratio of the growth rate along the R⟨1–101⟩ and C⟨0001⟩ directions and results in the PIN structures with desired complete coverage as shown in the figure 4.16 (c).

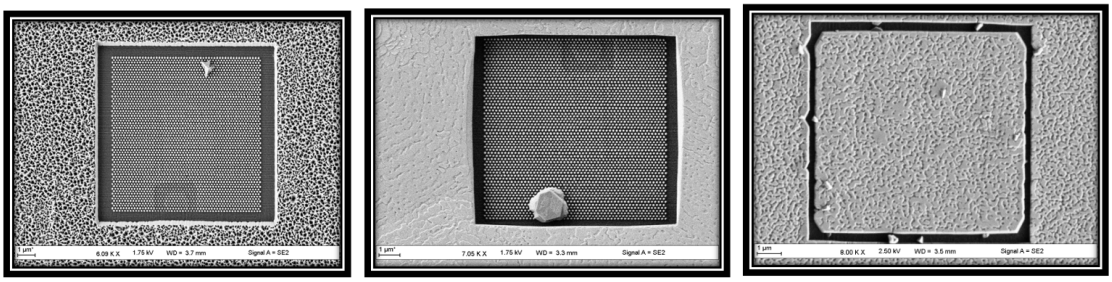

Figure 4.17: (a) SEM images of InGaN nanopyramid before growth of lateral GaN, (b) with lateral GaN growth and (c) the lateral p-GaN growth.

GaN doped with Mg is grown at 1000°C for laterally covering InGaN nanopyramids on n-GaN templates as shown in the figure 4.16 (c). The I–V measurements recorded in both planar and nanostructured areas reveal clear rectifying characteristics as shown in figure 4.16(b) with orders of magnitude better diode behavior (large currents and rectification ratio) in the patterned area embedding the InGaN nanostructures has been demonstrated [Sun15b]. Further solar cell structures were fabricated. V_{oc}, I_{sc}, FF were 1.28 V, 5.26 mA/cm^2 19% respectively. The overall efficiency was around 1.30 % under UV light illumination. These results are very encouraging as the technique may overcome current limitations in the growth of high quality thick InGaN nano-structures and may be important for the realization of InGaN-based high efficiency solar cells [Elh19].

4.6 InGaN/GaN MQWs based solar cells on h-BN

InGaN/GaN MQWs based device structures similar to the one previously reported as blue LEDs on h-BN in the chapter 2 were grown on h-BN templates on sapphire substrates for exploring solar cell applications. Several solar cells with

different designs and sizes were fabricated using a 2-inch grown sample as shown in the figure 4.18 (a & b).

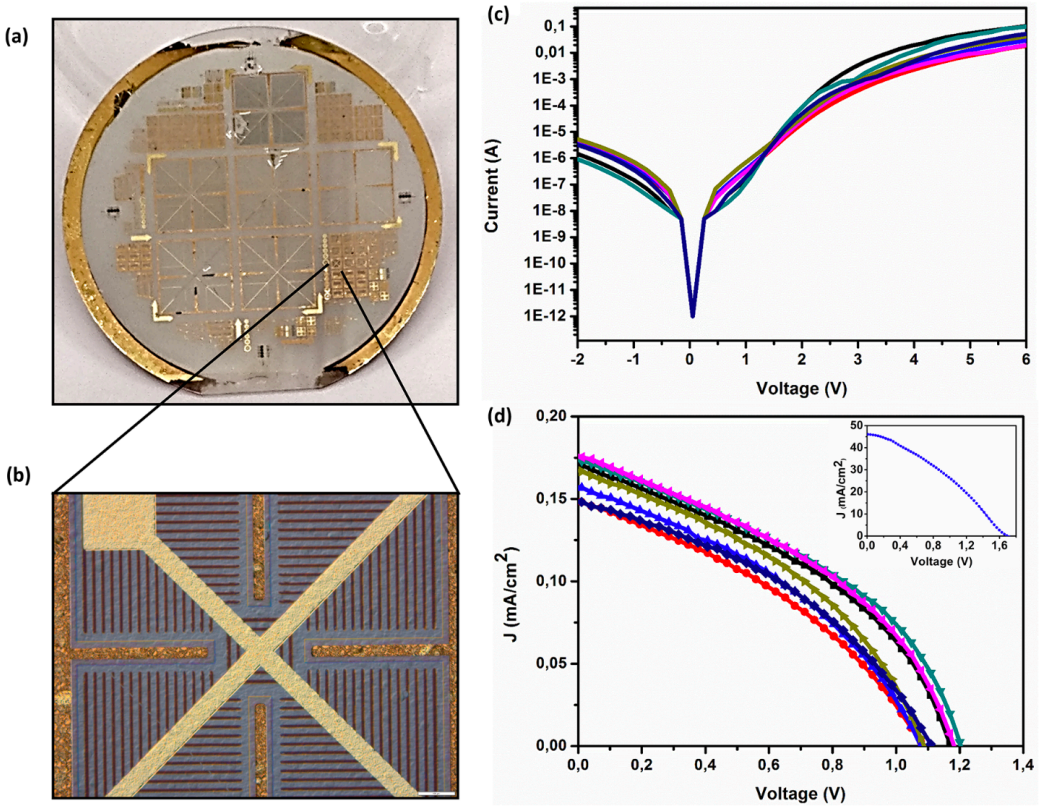

Figure 4.18: (a) Photograph of the fabricated solar cells on 2 in. h-BN/sapphire. (b) Optical microscopy image of a ~1mm2 solar cell with design A. (c) Dark I−V curves of devices in different locations on the wafer and their corresponding illuminated J−V curves under AM 1.5 condition in (d). Inset in (d) shows the illuminated J−V under a concentrated light source emitting at 440 nm. Ref. [Aya18]

Corresponding dark I−V curves of solar cell devices in different locations on the wafer and their illuminated J−V curves under AM 1.5 condition are shown in figure 4.18 (c & d). Inset in (d) shows the illuminated J−V under a concentrated light source emitting at 440 nm. After studying the solar cell characteristics, the cells were lifted off the BN templates and transferred to the foreign substrates like Al coated Glass templates and dielectric mirror reflecting 440 nm light with structure and reflectivity as shown in the 4.19 (a & b). This transfer offers a new technological degree of freedom that allowed an increase in the J_{sc} up to 20% when placed on a back-side reflector and dielectric mirror as shown in the figure 4.19 (c & d) respectively. These results confirm

that mechanical liftoff process using the ultra-thin layered h-BN as sacrificial layer results in preservation or improved performance of the III-nitride based devices in-addition to lowering the cost of the overall devices.

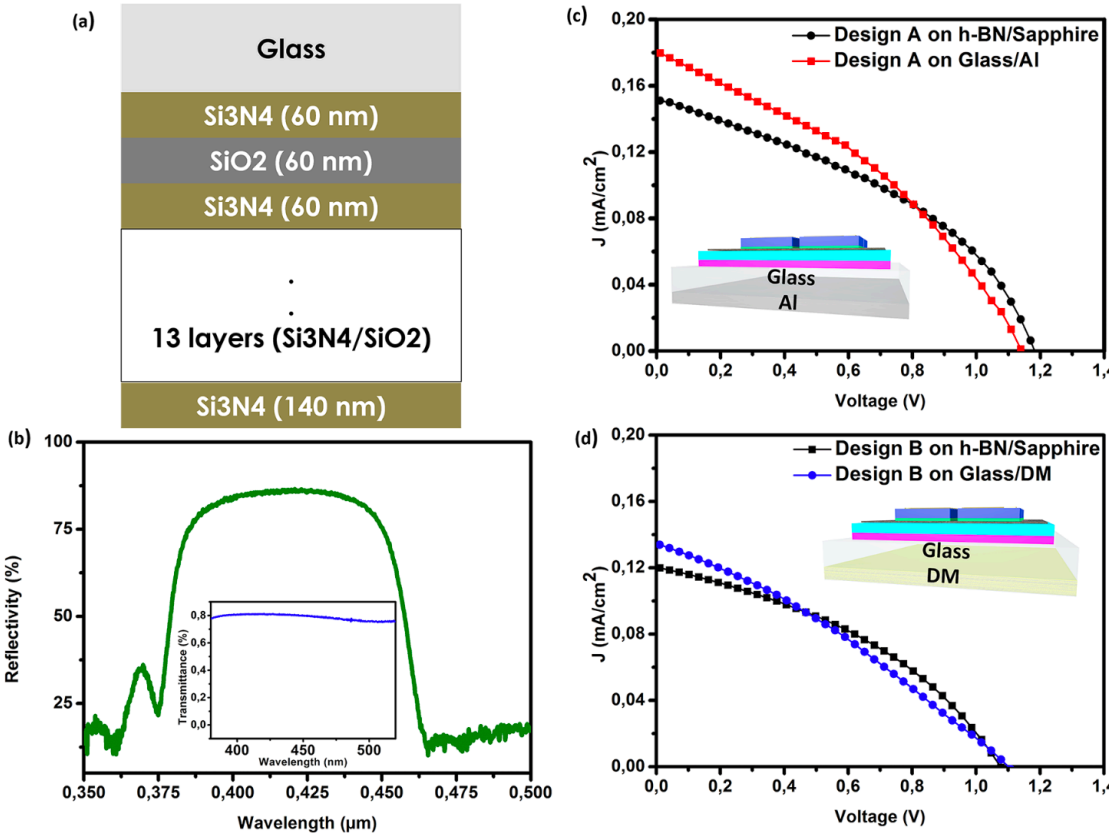

Figure 4.19. (a) Schematic of the deposited DM on glass. (b) FTIR measurements for the deposited DM on glass. (c, d) are J−V curves under AM 1.5 illumination condition of respectively the same solar cell with design A before and after its transfer to a glass with Al back reflector and the same solar cell with design B before and after its transfer to a glass with a dielectric mirror. Inset in (b) shows the transmittance of the polyurethane- based resins. Ref. [Aya18]

Summary

We have demonstrated InGaN based solar cells with several types of absorbers starting from bulk, semibulk, nanopyramidal and MQWs/h-BN utlilizing heteroepitaxial growth, nanoheteroepitaxial growth and van der Waals epitaxial growth respectively. Even though there is still a lot of room for improvement, all these technologies showed decent solar cell performances. In particular MQWs on sacrificial h-BN can be beneficial for realizing low cost tandem solar cells. Combining

technologies like realizing semibulk or nanopyramidal absorbers on sacrificial h-BN may yield better performances at much lower costs which will be investigated in the future. Based on these studies on InGaN based devices structures, we have published more than 23 peer reviewed publications in highly reputed Journals and several international collaborations and funded projects are still actively being implemented.

5. AlGaN based UV sources and sensors

5.1 AlGaN based DBRs for Resonant Cavity Light Emitting Diodes (RCLEDs)

Even though III-nitride-based blue and green LEDs have reached commercial maturity, high-efficiency RCLEDs emitting below 400 nm and in the deep ultra-violet (DUV) range are still missing. Resonant-cavity light-emitting diodes (RCLEDs) can be regarded as a hybrid between vertical- cavity surface-emitting lasers (VCSELs) and conventional light-emitting diodes (LEDs). When compared to the output from non-resonant cavity LEDs, the light output from RCLEDs is brighter, highly directional, spatially coherent, and spectrally pure [Sch92].

InGaN quantum well based RCLEDs emitting around 380–400 nm is very attractive for applications in industry, instrumentation or medicine such as photocatalysis, photolithography with and without mask, fibered light sources for spectroscopic sensing, photodynamic therapy for skin cancer and actinic keratosis treatment, fluorescence endoscopy, fluorescence microarrays and microscopy [Gor99] [Ber05] [Fie08]. Eventhough RCLEDs emitting at higher wavelengths have been demonstrated [Maa02] [Lu07], design and fabrication of RCLEDs emitting at the wavelength below 400 nm remains challenging and undemonstrated so far because of the requirement of high-quality optical resonators [Dia01]. Different growth architectures were reported in the literature to realize these resonators. Metallic, epitaxially grown (GaInAl)N/GaN DBR, and oxide-based DBR (e.g., SiO_2, TiO_2) mirrors are generally used. Both metallic and oxide DBR bottom mirrors require difficult, expensive and complex lift-off processes [Son00] [Hu11], rendering an (Ga, In, Al)N/GaN growth the preferable choice. The crystal quality of these high reflective DBRs degrades severely due to an increase in strain after a certain number of pairs are grown. Consequently, the quality of bottom DBRs will affect the active region of the

cavity. Apart from the realization of crack-free GaN-based DBRs with high reflectivity around 90% with a minimum number of pairs, there are many critical problems associated with the fabrication of high performance, UV-emitting RCLEDs on AlGaN/GaN DBR. First and foremost is the control of defects in the active region propagating from the bottom mirror, as well as the position of the active region, optimization of metallic or dielectric top mirror and device processing issues. There are only limited reports responding to these critical issues towards realization of high quality RCLED structures emitting below 400 nm.

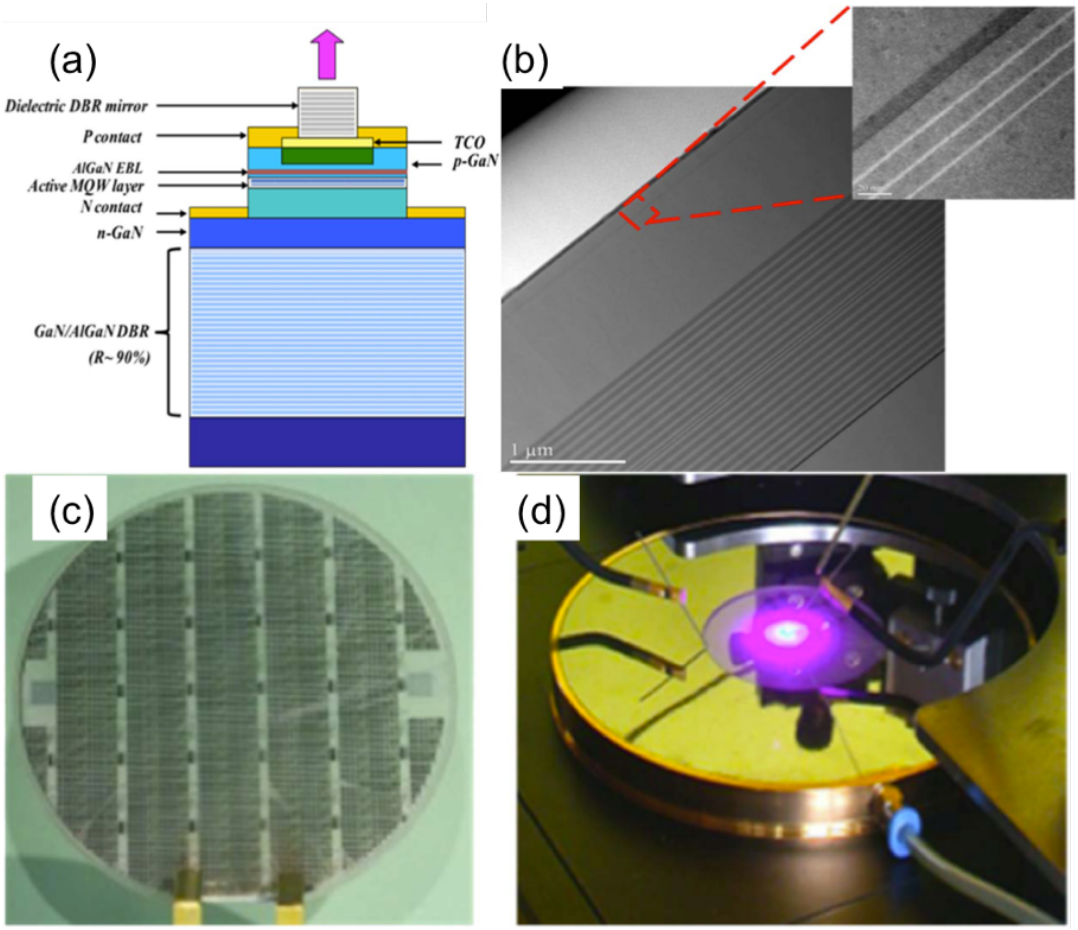

Figure 5.1: (a) Cross section of a RCLEDs device designed for light emission at 390 nm. (b) HAADF-STEM image of RCLED structure without top mirror. The zoom corresponds to the InGaN/GaN MQW region. The scale line represents 20 nm. (c) RCLED wafer after full lithographic process and (d) wafer level probing of RCLEDs showing light emission at 390 nm. Ref [Mou13]

Resonant cavity light emitting diodes (RCLEDs) emitting at 390 nm with structure as shown in the figure 5.1(a) was realized. It features novel coherently strained, crack free 20 pair AlGaN/GaN DBR. First, a thin AlN buffer layer was grown on a GaN template, then a classical quarter wavelength AlGaN/GaN DBR was grown normally except for one AlGaN layer in the middle of the structure which was replaced by an AlN/GaN/AlN multilayer. The optical thickness of this multilayer was calculated so as not to break the periodicity of the mirror for constructive interferences. The AlGaN/GaN DBR structure had a high reflectivity around 90% at 390 nm. The complete structure is as shown in the STEM image in figure 5.1(b) at the bottom and 2.5 pairs SiO_2/ZrO_2 dielectric top mirror. The devices were fabricated on this final structure as shown in the figure 5.1(c). These devices have been demonstrated with UV light emission around 390 nm with near-milliwatt-power as shown in figure 5.1(d) [Mou13]. The increase in dislocation density by an order of magnitude during the growth of AlGaN/GaN DBR was found to affect the light output. We expect that as we reduce the losses in the RCLED structures by the use of ultra-low dislocation density GaN templates, these devices can be pushed to a much significantly higher light output at low injection current.

5.2 AlGaN/AlGaN MQWs on relaxed AlGaN buffer

During this pandemic period, there is a strong demand for semiconductor light sources emitting in the DUV region for a wide variety of potential applications such as sterilization, water/air purification. Other applications of DUV-LEDs include optical imaging systems, spectroscopy, or high-density storage systems. III-nitrides are potential candidates because of their interesting properties including tunable band gap covering the entire UV spectral range, thermal and chemical stability. However,

compared with InGaN based visible laser diodes or LEDs, the development of DUV light sources based on AlGaN material system is still a challenge [Kne16]. One of the major problems with Al-rich AlGaN epilayers is that they suffer from cracks or high dislocation density due to their large lattice mismatch with conventional III-N templates [Li15] [Li15a] [Gau08]. Apart from this *p*-doping efficiency and the light extraction efficiency is also low in the designed structures resulting in overall efficiency generally lower than 10%.

First, Al-rich AlGaN epilayers suffer from cracks or high dislocation density due to their large lattice mismatch with conventional sapphire or SiC substrates. To address this issue AlGaN superlattices have been used [Fuj14] [Jme13] [Loc13]. In this approach, the active region still remains under high strain (the strain $|\varepsilon|$ in the barriers > 0.9%). Besides, AlGaN MQWs suffer from the strong quantum confined Stark effect (QCSE) induced by piezoelectric and spontaneous polarization, which leads to the separation of electrons and holes and reduces significantly the emission efficiency [Ala09] [Gau08]. In addition, c-plane AlGaN alloys also exhibit anisotropic optical polarization properties: E-field ⊥ c polarized emission (which will be referred to as TE polarization) decreases when compared to the emission polarized along the c axis (E-field // c) as the Al composition increases for the deep UV wavelength, which is detrimental to surface-emission. In other words, Oscillator strength of the fundamental transition in the AlGaN MQW structure, is highly reduced with increasing Al fraction. This is attributed to the arrangement of the valence bands at the Γ point of Brillouin zone [Ryu13] [Kol10] [Nam04] [Ler04] [Ler02], leading to the lower TE efficiency of AlGaN-based DUV lasers or LEDs. To overcome this issue, we have designed and realized a MQW structure: $Al_{0.57}Ga_{0.43}N/Al_{0.38}Ga_{0.62}N$ MQWs on a relaxed $Al_{0.58}Ga_{0.42}N$ buffer using AlN templates on sapphire as a substrate. This

relaxed AlGaN buffer is used to release the excess strain in the barriers. A DUV MQW structure emitting 280 nm was designed and grown on a relaxed AlGaN buffer. The HAADF-STEM image of the quantum wells shown in figure 5.2 (a) confirms the presence of MQWs with abrupt interfaces. The barriers thickness is measured to be 10 ~11 nm from intensity profiles and the wells thickness is of 1.6 ~1.8 nm. This structure reduces the strain in the wells enhancing the optical emission and consequently maximizes the oscillator strength of the optical transition for TE polarization as demonstrated in the figure 5.2(b) & (c). The structure exhibits an emission peak at 286 nm with a sharp linewidth at 77 K. Transmission measurements combined with simulations confirm a sufficient oscillator strength leading to an optical absorption coefficient in the wells as high as 3×10^5 cm^{-1}. The results represent an important step towards the development of DUV light sources, especially surface-emitting LEDs and lasers.

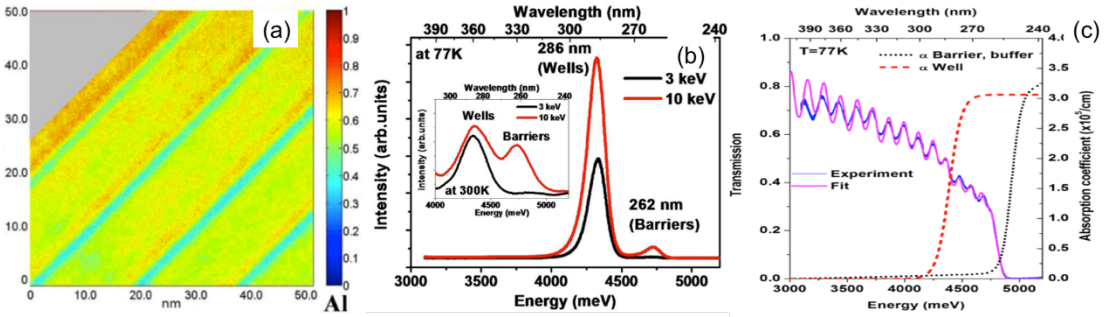

Figure 5.2: (a) Al composition map obtained from high magnification of HAADF-STEM images taken along the <1 1 −2 0> zone axis for AlGaN/AlGaN MQWs. (b) Cathodoluminescence (CL) spectra at 77 K (and at 300 K in the inset) for two different values of excitation power. (c) Macro-transmission measurements and transfer-matrix simulation of MQWs together with absorption coefficients (αwell , αbarrier, buffer) used in the simulation. Ref [Li15a]

Further the optical influences of the defects like threading dislocations and V-shape pits in AlGaN MQWs grown on AlGaN buffer on AlN templates were also studied and reported [Li15].

5.3 AlGaN/AlGaN based MQWs on h-BN

Applying similar strategy as in previous chapters to grow III-nitride wafers on h-BN, wafer-scale growth and mechanical exfoliation of 20 period $Al_{0.58}Ga_{0.42}N/Al_{0.37}Ga_{0.63}N$ multiple quantum wells (MQWs) on relaxed buffer with AlN layers as interfacial buffers to h-BN sacrificial layers were realized. This structure is used to study further the application of the van der Waals epitaxial growth technology and also to study the mechanical exfoliation characteristics of the UV emitting structures that can be beneficial for improving the light extraction efficiency. The same structure grown on AlN templates were compared with the one on BN buffered templates as reference.

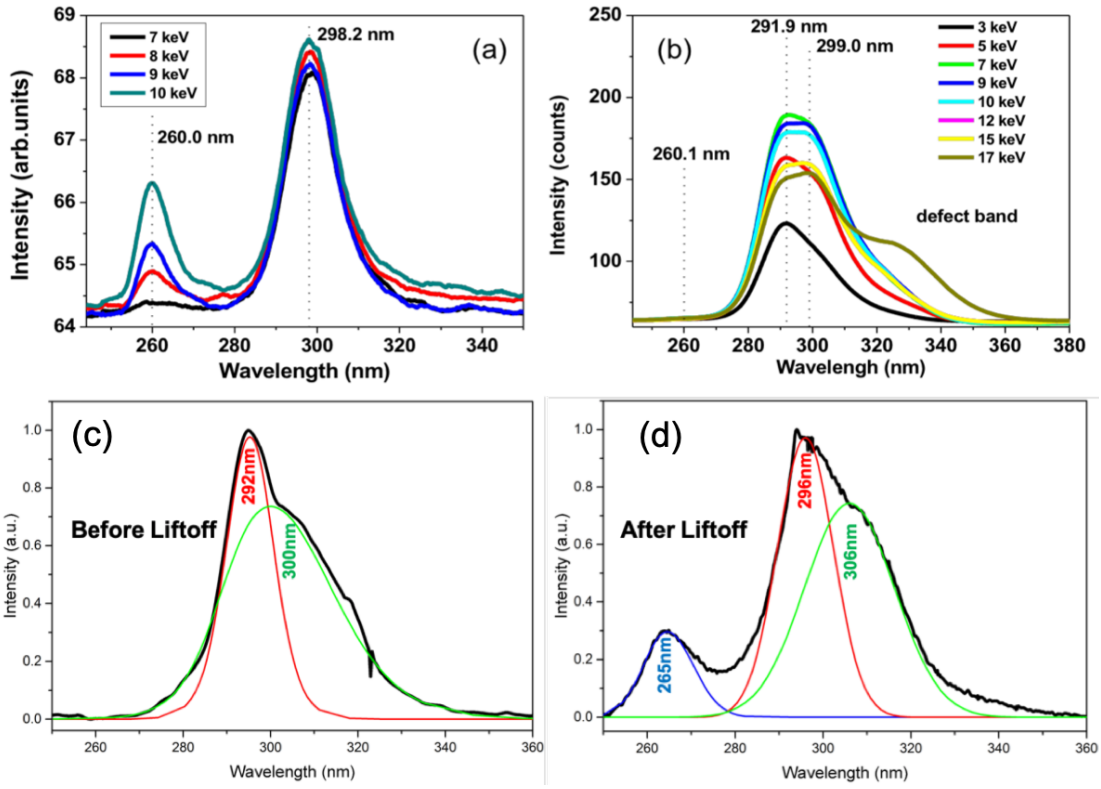

Figure 5.3: Depth-resolved cathodoluminescence emission from the (a) AlGaN/AlGaN MQWs on AlN buffered sapphire substrates and (b) AlGaN/AlGaN MQWs on h-BN buffered sapphire substrates showing emission around 292 nm. Room temperature cathodoluminescence emission from AlGaN/AlGaN MQWs on h-BN buffered sapphire substrates (c) before liftoff and (d) after lift-off. The black curve is the raw data, red, green and blue curves are deconvoluted individual peaks. Ref [Sun19].

Emission characteristics of the MQW structures on AlN and h-BN templates were shown in figure 5.3(a & b) respectively. As shown in figure 5.3 (a) a single MQW emission peak is observed at 298 nm for the structures on AlN templates while the peak around 260 nm originates from the thick AlGaN buffer. On h-BN templates, double MQWs emission peaks were observed, at 299 nm and 292 nm as shown in figure 5.3(b). Emission inhomogeneities observed on these samples are due to a high density of threading dislocations that form surface V-pits with {1 0−1 1} facets or sidewalls where the MQWs grows slower and gives rise to broader or shoulder peaks. Following emission studies, the AlGaN/AlGaN MQW structures on h-BN templates were lifted off from the sapphire substrates using copper metallic tapes. To study the variation in emission characteristics before and after exfoliation from the sapphire substrate, CL emission from the MQW structure were recorded under an electron beam excitation energy of 3 keV, which is shown in Fig. 5.3(c) and (d) respectively. As previously discussed, before lift-off, the emission from the MQW structure exhibits double emission peaks, for the sake of comparison, the normalized deconvoluted peaks along with raw data recorded under 3 keV excitation energy are shown in Fig. 5.3(c). After exfoliation, under same excitation conditions, we observed similar double MQW peaks along with the broad AlGaN buffer peak at 265 nm as shown in Fig. 5.3(d). The peak position is shifted by few nm confirming the residual strain relief during liftoff. This residual strain relaxation is due to the exfoliation process which does not affect the structural and optical integrity of the AlGaN/AlGaN MQWs or the relaxed buffer and even maintains the two MQWs emission peak intensity ratio. Hence it is believed that the overall emission efficiency of the AlGaN/AlGaN MQWs on the relaxed buffer will be unaffected by this strain variation induced by the exfoliation process. The difference in AlGaN buffer peak intensity is due to its proximity to the exciting electron beams,

this is because, after liftoff, the sample is probed from the back side, yielding a larger intensity. This series of studies confirm that the optical characteristics of the AlGaN/AlGaN MQW on AlN/h-BN templates are preserved during this exfoliation process. Further experiments are needed to study the improvement in light extraction efficiency and realization of RCLEDs/VCSELs structures using this technology [Sun19].

5.4 AlGaN/GaN HEMTs for sensor applications

AlGaN/GaN based HEMTs devices are robust sensors with catalytically active gate electrodes that are attractive for automotive exhaust applications where exhaust gas temperatures are elevated (2000 °C) due to their many advantageous material properties, such as high thermal and chemical stability [Bis16] [Hal16] . In the context of automobile exhaust applications, there is strong interest in selectively achieving NO, NO2 and NH_3 detection. AlGaN/GaN HEMT-based NO, NO_2 and NH_3 exhaust gas sensors for automotive antipollution systems has been developed.

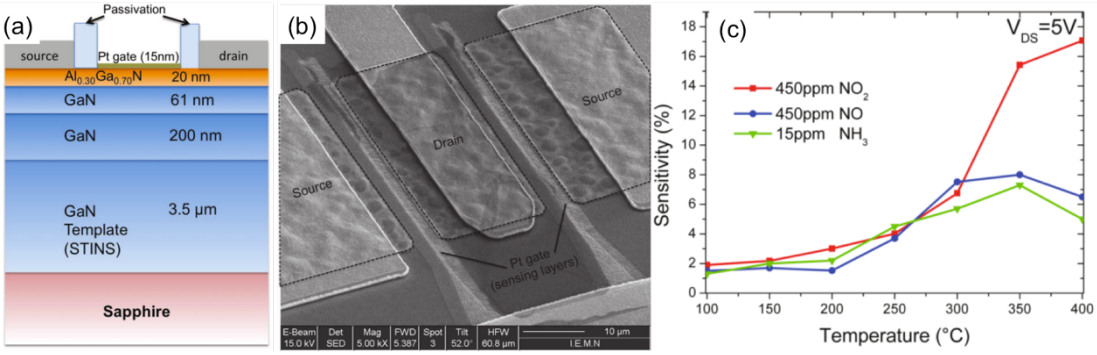

Figure 5.4: (a) AlGaN/GaN HEMT structure (b) SEM image of processed sensor device and (c) Sensitivity of 450ppm NO and NO2 and 15ppm NH3 from 100-400°C with 0V gate bias. Ref. [Bis16]

The structure and the SEM image of the fabricated HEMT devices are shown in figure 5.4 (a) and (b). High sensitivity of the devices and selectivity for the NO, NO_2 and NH_3

at elevated temperatures up to 400°C were demonstrated in collaboration with our industrial partners [Hal16].

5.5 AlGaN/GaN HEMTs on h-BN with better sensing

The transfer of AlGAN/GaN based gas sensors to foreign substrates provides a pathway to enhance sensor performance, lower the cost and extend the applications to wearable, mobile or disposable systems. The main keys to unlocking this pathway is to grow and fabricate the sensors on large h-BN surface and to transfer them to the flexible substrate without any degradation of the performances as shown in the figure 5.5. To realize this dream applications, AlGaN/GaN gas sensors structures were grown on 2-inch sapphire wafers with a sacrificial 2D layered h-BN by MOVPE in wafer scale using van der Waals epitaxy discussed in chapter 2 and devices were fabricated.

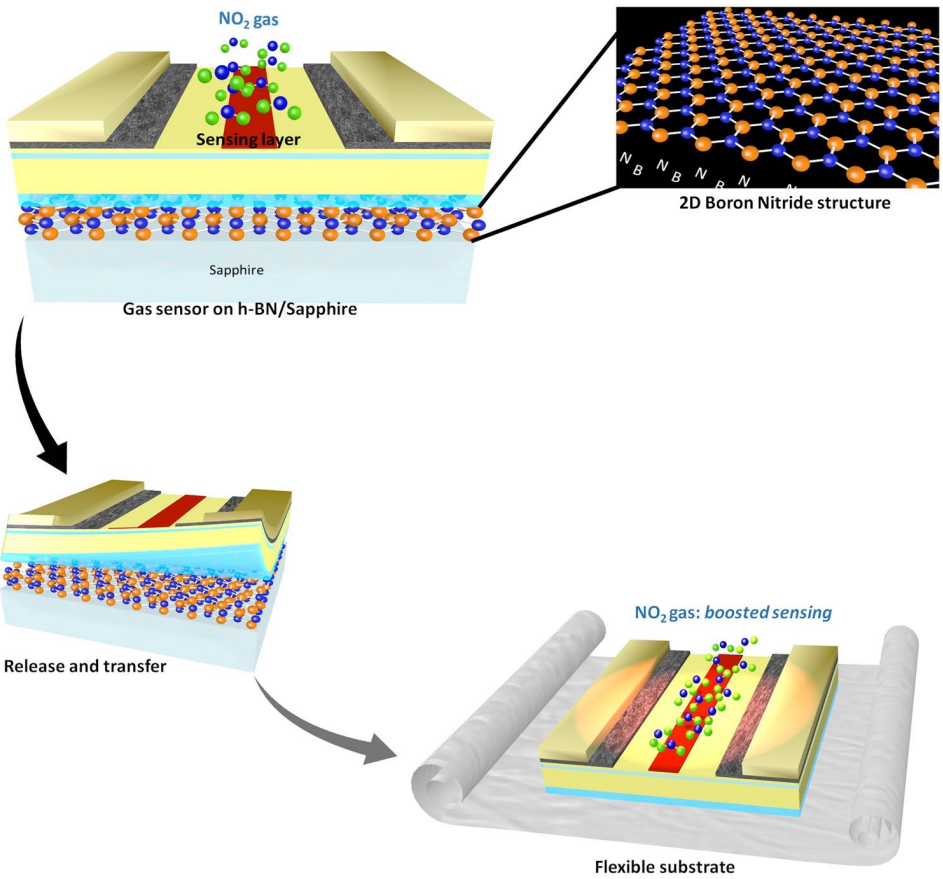

Figure 5.5. Our approach for the growth, fabrication, release and transfer of boosted AlGaN/GaN gas sensor to a flexible sheet using h-BN as a buffer and release layer. Ref. [Aya17]

AlGaN/GaN based high electron mobility transistor (HEMT) structures with $Al_{0.25}Ga_{0.75}N$ top barrier layers were realized on the h-BN/sapphire templates using van der Waals epitaxy. AlGaN interfacial buffer layers similar to that used in chapter 2 was employed. Full front-end process was applied to the device structure to fabricate transistor as shown in the figure 5.6(a). The transistors I_{DS}-V_{DS} characteristic is as shown in the figure 5.6 (b). The 2D electron gas density was around 1.0586E+13 cm^{-2} with 300 $cm^2.V^{-1}.s^{-1}$ mobility, average sheet resistance was found to be higher (2.0632E+03 Ω/square) with 60% of the processed devices have more than 40% pinching as shown in the figure 5.6(c). The mobility is quite low when compared to standard devices on GaN templates due to the AlGaN barrier and GaN interface quality. Using AlN interfacial buffer on h-BN-buffered sapphire substrates may improve the mobility to state of art, AlGaN/GaN heterostructure with electron mobility of 1,100 $cm^2.V^{-1}.s^{-1}$ was already reported [Gla17] .

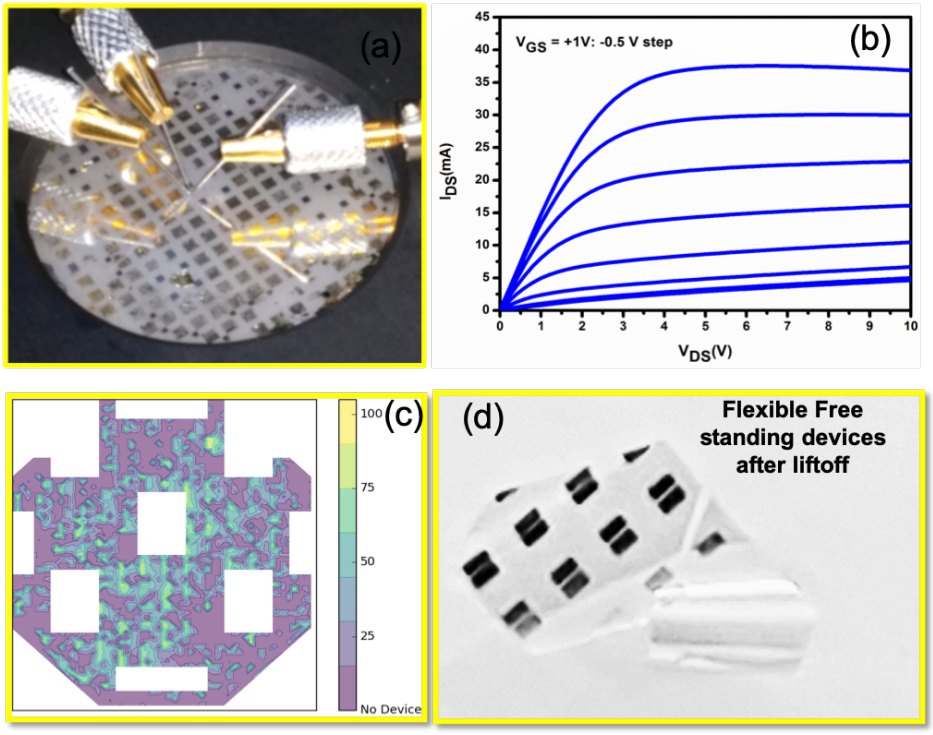

Figure 5.6: (a) Photo of the wafer-scale processed AlGaN/GaN sensors, (b) IDS-VDS characteristic of an AlGaN/ GaN device with 2 µm gate length (c) Wafer mapping of the gate pinching, with white areas representing masked-off regions that include TLM patterns (d) Free standing GaN structures from the similar device stacks demonstrating high flexibility and crack free liftoff. Ref. [Aya17].

In addition to transferring HEMT based sensor devices to a flexible substrate we obtained freestanding devices also as shown in the figure 5.6 (d). We also demonstrate an enhancement in gas sensing performance of these devices. This is in part due to the effect of foreign substrate choice on the temperature in the two-dimensional gas (2DEG) channel of the AlGaN/GaN heterostructure which is validated by thermal modeling and Raman spectroscopy. The sensors are tested before and after transfer to the flexible substrate with significant improvements in both sensitivity and response time after the transfer. This approach for engineering of GaN-based sensors is a key step in the pathway towards economically viable, flexible sensors with improved performances that could be integrated into wearable applications.

Summary

AlGaN based heterostructures were grown and explored in device application such as RCLEDs, UVLEDs and GaN sensors. Apart from associated structural challenges, Al rich AlGaN has been shown to have the potential to be used in devices. Because of the issues associated with Al rich AlGaN more innovative approaches have been employed for realizing device structures. Again, application of van der Waals epitaxy to given dramatic results in terms of boosted performances in gas sensors and also paving a way to solve light extraction efficiency issue in the UVLEDs. These studies show that considerable progress has been made but there is still a lot of room for improvement. Further deep investigation is under way in our group to optimize AlGaN UVLEDs structures on BN templates and also employ them as a effective p-layer. Both these approaches if successful will increase the efficiency of the UVLEDs structures considerably. Research on this AlGaN based UV emitters and sensors have been published in more than 10 peer reviewed journal articles and led to many international collaborations and funded projects.

6 Conclusion and perspectives

This habilitation manuscript summarizes my research on MOVPE growth technologies related to III-nitride materials, resulting in innovative and novel device designs for next generation devices.

Progress in Boron Nitride

First, high-quality layered h-BN was grown on sapphire substrates with pleats and pleat-free surface morphology which was a huge bottle neck a decade ago. This growth and related technology pioneered new opportunities in heteroepitaxy and heterogeneous integration. The structural, optical and electrical characteristics of these layers were deeply investigated and exploited further in various growth technologies mainly van der Waals epitaxy and remote epitaxy and other device applications. Subsequently, various III-nitride device structures were grown on this layered platform without degrading the potential characteristics.

Separation of active device structures of III-nitrides from rigid substrates, preserving the quality and in a cost-effective way, can lead to application in flexible electronics. Mechanical liftoff is a preferred solution, where device structures are grown on 2D materials like graphene and h-BN by van der Waals epitaxy and separated just by applying a shear force. Especially, h-BN is preferred as it is another III-nitride material and can be grown in the same reactor. Most III-nitride device structures have been lifted off and transferred to a variety of platform.

In addition, a fundamental mechanism controlling the transfer of atomic registry through these 2D layer (*remote epitaxy*) has been studied, the polarity of the 2D layers was found to be governing remote epitaxy.

Controlled separation of these high-quality multilayered h-BN layers resulting in precise wafer-scale monolayers of h-BN has been demonstrated using Ni sticker [11].

This wafer-scale layer resolved lift-off may lead to realization of reliable 2D-2D van der Waals heterostructures assembly for novel device applications.

Progress in Novel boron containing alloys

Hexagonal phase, boron rich BAlN alloys were grown with layered characteristics and its properties were explored. Single crystalline wurtzitic phase of Al rich BAlN alloys were also grown and periodic heterostructures were formed with $Al_XGa_{(1-X)}N$ and explored for Distributive Bragg Reflector (DBR) applications. Even tough interesting, these boron containing alloys are difficult to grow maintaining phase purity and high quality. Nevertheless, nanoheteroepitaxy has been adapted to form single crystalline, thick and high quality BGaN nanostructures. This promising route to mitigate strain related degradation further opens the new research avenues.

Progress in InGaN alloys

Innovative, multijunction III-nitride solar cells need thick high-quality In rich InGaN to absorb maximum of sun light which is hard to realize. Thick In rich InGaN absorbers can been achieved by controlling the strain in InGaN using a novel semibulk and nanoheteroepitaxy approaches. In semibulk approach, very thin GaN layers are periodically inserted between thick InGaN layers which dramatically resets the effects of strain and results in good quality thick InGaN alloys. In nanoheteroepitaxy, the strain energy saturates because of the availability of the lateral free surface leading to mitigation of strain related degradation resulting in dislocation free InGaN nano-pyramidal structures. Using these approaches, device structures with InGaN have been realized and its characteristics were explored.

Progress in AlGaN alloys

AlGaN based high electron mobility transistor (HEMT) devices were investigated for sensing applications. The performance of the sensors were enhanced at a temperature of 600 °C which indicate that these HEMT based sensors could be used in a harsh environment with the ability to control an anti-pollution system in real time. Furthermore, in UV light emitting devices, it was found that the oscillator strength can be enhanced, preserving the transverse electric (TE) mode emission by using the relaxation-controlled Al rich AlGaN buffer.

Perspectives:

Still there is lot of room for research and innovation in all the avenues of this futuristic III-nitride materials. Emerging growth technologies such as Van der Waals epitaxy and remote epitaxy offers numerous opportunities, where the epilayers can be grown without misfit dislocations and strain that may lead to ground breaking device performances. Preliminary Investigation on this area yield very encouraging results with many open questions that needs extensive research to achieve further progress. For example, Improving the overall quality of 2D layers, control of coalescence of grains of BN, the substrate orientation and polarity effect on the growth of 2D layers, control of lateral quality of 2D layers, doping and alloying induced variation in structural and optical characteristics.

Apart from this, many applications for boron nitride and related alloys materials in innovative III-nitride device designs can be envisaged for exotic new functions. On one hand, BN quality in large scale on different compatible substrates has to be improved for buffer, sacrificial and protective layer applications. Already BN as buffer works well eliminating unwanted ramps and thick materials in the growth GaN which

can benefit the LED industry also if improved the process can lead to GaN buffers with lower density of defects. This can improve the quality of heterostructures and contribute to transfer to flexible or other beneficial platforms in view of the "on chip" systems for the future niche applications. On the other hand, robust BN and its alloys along with reliable conductivity control can extend the application of h-BN in UV optoelectronics as an alternative electron blocking layer, hole injector and also as a active detector material. Hence these materials and its alloys are currently under intense investigation for UV-LEDs, neutron detectors and sensing applications. In-addition, defect free InGaN nanopyramidal structures will be exploited for solar cells applications combining SAVWE and innovative transfer process for realizing tandem solar cells with higher efficiency. Furthermore, AlN and Al rich AlGaN alloys will be explored for UV LEDs and microelectronics applications.

Each of these studies may allow us to better understand this class of materials and increase the available degrees of freedom in the III-nitrides for novel device design that may lead to futuristic, low cost and high-performance device prototypes.

References:

[Abi11] M. Abid, T. Moudakir, Z. Djebbour, G. Orsal, S. Gautier, A. En Naciri, A. Migan-Dubois, A. Ougazzaden, J. Cryst. Growth 315, 283 (2011).

[Abi12] M. Abid, T. Moudakir, G. Orsal, S. Gautier, A. En Naciri, Z. Djebbour, J.-H. Ryou, G. Patriarche, L. Largeau, H. J. Kim, Z. Lochner, K. Pantzas, D. Alamarguy, F. Jo- mard, R. D. Dupuis, J.-P. Salvestrini, P. L. Voss, and A. Ougazzaden, Appl. Phys. Lett. 100, 051101, (2012).

[Aka06] T. Akasaka and T. Makimoto, Appl. Phys. Lett. 88, 041902, (2006).

[Aka07] T. Akasaka, Y. Kobayashi and T. Makimoto, J. Cryst. Growth 298, 320 (2007).

[Ala09] H. R. Alaei and H. Eshghi, Phys. Lett. A 374(1), 66 (2009).

[Ama89] H. Amano, M. Kito, K. Hiramatsu and I. Akasaki, M. Senoh, N. Iwasa, Jpn. J. Appl. Phys. 28, L2112 (1989).

[Ari16] M.Arif, J. P.Salvestrini, J. Streque, M. B. Jordan, Y. El Gmili, S. Sundaram, X. Li, G. Patriarche, P. L. Voss, and A. Ougazzaden, Appl. Phys. Lett. 109, 133507 (2016).

[Ari17] M. Arif, W. Elhuni, J. Streque, S. Sundaram, S. Belahsene, Y. El Gmili, M. Jordan, X. Li, G. Patriarche, A. Slaoui, A. Migan, R. Abderrahim, Z. Djebbour, P.L. Voss, J.P. Salvestrini, A. Ougazzaden, Solar Energy Materials & Solar Cells, 159, 405 (2017).

[Ats14] K. Atsumi, APL Mater. 2, 032106 (2014).

[Aya16] T. Ayari, S. Sundaram, X. Li, Y. El Gmili, P. L. Voss, J. P. Salvestrini, A. Ougazzaden, Appl. Phys. Lett., 108, 171106 (2016).

[Aya17] T. Ayari, C. Bishop, M. B. Jordan, S. Sundaram, X. Li, S. Alam, Y. ElGmili, G. Patriarche, P. L. Voss, J. P. Salvestrini, and A. Ougazzaden, Sci. Rep. 7, 15212 (2017).

[Aya18] T. Ayari, S. Sundaram, X. Li, S. Alam, C. Bishop, W. El Huni, M. B. Jordan, Y. Halfaya, S. Gautier, P. L. Voss, J. P. Salvestrini, and A. Ougazzaden, ACS Photonics 5, 3003 (2018).

[Aya19] T. Ayari, S. Sundaram, C. Bishop, A. Mballo, P. Vuong, Y. Halfaya, S. Karrakchou, S. Gautier, P. L. Voss, J. P. Salvestrini, and A. Ougazzaden, Adv. Mater. Technol. 4, 1900164 (2019).

[Bag09] T. Baghdadli, S. Ould Saad Hamady, S. Gautier, T. Moudakir, B. Benyoucef, A. Ougazzaden, Phys. Status Solidi c 6, S1029 (2009).

[Ber05] M. Berneburg, M. Ro¨cken, and F. Benedix, Acta Derm.-Venereol., 85, 98 (2005).

[Bis14] M. A. Bissett, M. Tsuji, and H. Ago, Phys. Chem. Chem. Phys. 16, 11124–11138 (2014).

[Bis15] C. Bishop, J. P. Salvestrini, Y. Halfaya, S. Sundaram, Y. El Gmili, L. Pradere, J. Y. Marteau, M. B. Assouar, P. L. Voss, and A. Ougazzaden, Appl. Phys. Lett. 106, 243504 (2015)

[Bis16] C. Bishop, Y. Halfaya, A. Soltani, S. Sundaram, X. Li, J. Streque, Y. El Gmili, P. L. Voss, J. P. Salvestrini, A. Ougazzaden, *IEEE Sens. J.*, 16, 6828 (2016).

[Cas16] G. Cassabois, P. Valvin, B. Gil, Nat. Photonics 10, 262 (2016).

[Chu10] K. Chung, C.-H. Lee, G. C. Yi, Science 330, 655 (2010).

[Chu14] K. Chung, H. Beak, Y. Tchoe, H. Oh, H. Yoo, M. Kim, and G.-C. Yi, APL Mater. 2, 092512 (2014).

[Chu18] D. Chugh, J. Wong-Leung, L. Li, M. Lysevych, H.H. Tan, and C. Jagadish, 2D Mater. **5**, 045018 (2018).

[Con13] H. J. Conley, B. Wang, J. I. Ziegler, R. F. Haglund, S. T. Pantelides, and K. I. Bolotin, Nano Lett. 13, 3626–3630 (2013).

[Cos13] A. Castellanos-Gomez, R. Roldán, E. Cappelluti, M. Buscema, F. Guinea, H. S. J. Van Der Zant, and G. A. Steele, Nano Lett. 13, 5361 (2013).

[Dab20] A.K. Dąbrowska, M. Tokarczyk, G. Kowalski, J. Binder, R. Bozek, J. Borysiuk, R. Stępniewski, and A. Wysmolek, 2D Mater. **8**, 015017 (2020).

[Dah11] R. Dahal, J. Li, S. Majety, B.N. Pantha, X.K. Cao, J.Y. Lin, H.X. Jiang, Appl. Phys. Lett. 98, 211110 (2011).

[Dai15] X. Dai, A. Messanvi, H. Zhang, C. Durand, J. Eymery, C. Bougerol, F. H. Julien, and M. Tchernycheva, Nano Lett. 15, 6958 (2015).

[Dea10] C.R. Dean, A.F. Young, I. Meric, C. Lee, L. Wang, S. Sorgenfrei, K. Watanabe, T. Taniguchi, P. Kim, K.L. Shepard, J. Hone, Nat. Nanotechnol. 5, 722 (2010).

[Den98] S. P. DenBaars and S. Keller, in "Gallium Nitride (GaN) I." Semicon- ductors and Semimetals (J. I. Pankove, T. D. Moustakas, Eds.), Vol. 50. Academic Press, New York, 1998.

[Dia01] M. Diagne, Y. He, H. Zhou, E. Makarona, A. V. Nurmikko, J. Han, K. E. Waldrip, J. J. Figiel, T. Takeuchi, and M. Krames, Appl. Phys. Lett., 79, 3720 (2001).

[Elg13] Y.E lGmili, G. Orsal, K. Pantzas, T. Moudakir, S. Sundaram, G. Patriarche, J. Hester, A. Ahaitouf, J.P. Salvestrini, A. Ougazzaden, Acta Materialia, 61, 17, 6587 (2013).

[Elh19] W. El Huni, S. Karrakchou, Y. Halfaya, M. Arif, M. B Jordan, R. Puybaret, T. Ayari, H.Ennakrachi, C. Bishop, S. Gautier, A.Ahaitouf, P. L Voss, J. P.Salvestrini, A. Ougazzaden, Solar Energy, 190, 93 (2019).

[Fie08] A. Fiedler, J. Rehdorf, F. Hilbers, L. Johrdan, C. Stribl, and M. Benecke, Open Forensic Sci. J., 1, 12, (2008).

[Fuj14] A. Fujioka, K. Asada, H. Yamada, T. Ohtsuka, T. Ogawa, T. Kosugi, D. Kishikawa, and T. Mukai, Semicond. Sci. Technol. 29(8), 084005 (2014).

[Gau08] S. Gautier, T. Aggerstam, A. Pinos, S. Marcinkevičius, K. Liu, M. Shur, S.M. O'Malley, A.A. Sirenko, Z. Djebbour, A. Migan-Dubois, T. Moudakir, A. Ougazzaden, J. Crystal Growth, 310, 4927 (2008).

[Gau11] S. Gautier, G. Patriarche, T. Moudakir, M. Abid, G. Orsal, K. Pantzas, D. Troadec, A. Soltani, L. Largeau, O. Mauguin, A. Ougazzaden, J. Cryst. Growth 315, 288 (2011)

[Gei13] A.K. Geim, I.V. Grigorieva, Nature 499, 419 (2013).

[Gei66] R. Geick, C. Perry, G. Rupprecht, Phys. Rev., 146, 543 (1966).

[Gib04] P. Gibart, Rep. Prog. Phys. **67,** 667 (2004).

[Gig20] J. Gigliotti, X. Li, S. Sundaram, D. Deniz, V. Prudkovskiy, J. P. Turmaud, Y. Hu, Y. Hu, F. Fossard, J. S. Mérot, A. Loiseau, G. Patriarche, B. Yoon, U. Landman, A. Ougazzaden, C. Berger, and Walt A. de Heer, ACS Nano, 14, 12962 (2020).

[Gla17] N. R. Glavin, K. D. Chabak, E. R. Heller, E. A. Moore, T. A. Prusnick, B. Maruyama, D. E. Walker, D. L. Dorsey, Q. Paduano, M. Snure, Adv. Mater., 29, 1701838 (2017).

[Gor99] P. M. Gordon, B. L. Diffey, J. N. Matthews, and P. M. Farr, J. Amer. Acad. Dermatol., 41, 728 (1999).

[Hal16] Y. Halfaya, C. Bishop, A. Soltani, S. Sundaram, V. Aubry, P. L. Voss, J. P. Salvestrini and A. Ougazzaden, Sensors, 16, 273 (2016).

[Hoo04] S. E. Hooper, M. Kauer, V. Bousquet, K. Johnson, J. M. Barnes, and J. Heffernan, Electron. Lett. 40, 33 (2004)

[Hor02] M. Hori, K. Kano, T. Yamaguchi, Y. Saito, T. Araki, Y. Nanishi, N. Teraguchi, and A. Suzuki, "Phys. Stat. Soli. B: Basic Solid State Physics, 234, 750, (2002)

[Hor09] M. Horie, K. Sugita, A. Hashimoto, and A. Yamamoto, Sol. Energ. Mat. Sol. C., 93, 1013, (2009).

[Hu11] X. L. Hu, J. Y. Zhang, W. J. Liu, M. Chen, B. P. Zhang, B. S. Xu, and M. Wang, Electron. Lett., 47, 986 (2011).

[Isl09] M. Islam, K. Sugita, M. Horie, A. Hashimoto, and A. Yamamoto, Journal of Crystal Growth, 311, 2817, (2009).

[Jme13] V. N. Jmerik, E. V. Lutsenko, and S. V. Ivanov, Phys. Status Solidi A 210(3), 439 (2013).

[Jon16] E.A. Jones, F. Wang, D. Costinett, IEEE J. Emerg. Sel. Top. Power Electron. 4, 707 (2016).

[Kar20] S. Karrakchou, S. Sundaram, T. Ayari, A. Mballo, P. Vuong, A. Srivastava, R. Gujrati, A. Ahaitouf, G. Patriarche, T. Leichlé, S. Gautier, T. Moudakir, P. L. Voss, J. P. Salvestrini, and A. Ougazzaden, Sci. Rep. 10, 21709 (2020).

[Kim14] J. Kim, C. Bayram, H. Park, C. W. Cheng, C. Dimitrakopoulos, J. A. Ott, K. B. Reuter, S. W. Bedell, D. K. Sadana. Nat. Commun. 5, 4836 (2014).

[Kim17] Y. Kim, S. Cruz, K. Lee, B. O. Alawode, C. Choi, Y. Song, J. M. Johnson, C. Heidelberger, W. Kong, S. Choi, K. Qiao, I. Almansouri, E. A. Fitzgerald, J. Kong, A. M. Kolpak, J. Hwang and J. Kim., Nature 544, 340 (2017).

[Kne16] M. Kneissl, J. Rass (Eds.), Springer Series in Materials Science, 227, (2016).

[Kob08] Y. Kobayashi, T. Akasaka, J. Cryst. Growth, 310, 5044 (2008),

[Kol10] T. Kolbe, A. Knauer, C. Chua, Z. Yang, S. Einfeldt, P. Vogt, N. M. Johnson, M. Weyers, and M. Kneissl, Appl. Phys. Lett. 97(17), 171105 (2010).

[Kom84] A. Koma, K. Sunouchi, T. Miyajima, Microelectronic Engineering 2, 129 (1984).

[Kon18] W. Kong, H. Li, K. Qiao, Y. Kim, K. Lee, Y. Nie, D. Lee, T. Osadchy, RJ. Molnar, DK. Gaskill, RL. Myers-Ward, KM. Daniels, Y. Zhang, S. Sundram, Y. Yu, SH Bae, S. Rajan, Y. Shao-Horn, K. Cho, A. Ougazzaden, JC. Grossman, J. Kim, Nat Mater. 11 999-1004 (2018).

[Koy12] Y. Kobayashi, K. Kumakura, T. Akasaka, T. Makimoto, Nature 484, 223 (2012).

[Lal17] D.A. Laleyan, S. Zhao, S.Y. Woo, H.N. Tran, H.B. Le, T. Szkopek, H. Guo, G.A. Botton, Z. Mi, Nano Lett. 17, 3738 (2017).

[Lan11] J. Lang, C. Neufeld, C. Hurni, S. Cruz, E. Matioli, U. Mishra, and J. Speck, Applied Physics Letters, 98, 131115, (2011).

[Ler02] M. Leroux, S. Dalmasso, F. Natali, S. Helin, C. Touzi, S. Laügt, M. Passerel, F. Omnes, F. Semond, J. Massies, and P. Gibart, Phys. Status Solidi B 234(3), 887 (2002).

[Ler04] M. Leroux, F. Semond, F. Natali, D. Byrne, F. Cadoret, B. Damilano, A. Dussaigne, N. Grandjean, A. Le Louarn, S. Vézian, and J. Massies, Superlattices Microstruct. 36(4-6), 659 (2004).

[Li12] J. Li, S. Majety, R. Dahal, W. P. Zhao, J. Y. Lin, and H. X. Jiang, Appl. Phys. Lett. 101, 171112 (2012).

[Li12] Q. Li, J. B. Wright, W. W. Chow, T. S. Luk, I. Brener, L. F. Lester, and G. T. Wang, Opt. Express 20, 17873 (2012).

[Li15] X. Li, S. Sundaram, Y. El Gmili, F.Genty, S.Bouchoule, G.Patriache, P.Disseix, F.Réveret, J. Leymarie, J.-P.Salvestrini, R.D.Dupuis, P.L.Voss, A.Ougazzaden, J. Cryst. Growth 414, 119 (2015).

[Li15] X. Li, G. Le Gac, S. Bouchoule, Y. El Gmili, G. Patriarche, S. Sundaram, P. Disseix, F. Réveret, J. Leymarie, J. Streque, F. Genty, J.-P. Salvestrini, R.D. Dupuis, X.-H. Li, P.L. Voss, A. Ougazzaden, J. Cryst. Growth 432 (2015) 37.

[Li15a] X. Li, S. Sundaram, P. Disseix, G. Le Gac, S. Bouchoule, G. Patriarche, F. Réveret, J. Leymarie, Y. El Gmili, T. Moudakir, F. Genty, J.-P. Salvestrini, R.D. Dupuis, P.L. Voss, A. Ougazzaden, Opt. Mater. Express 5, 380 (2015).

[Li16] X. Li, S. Sundaram, Y. El Gmili, T. Ayari, R. Puybaret, G. Patriarche, P. L. Voss, J. P. Salvestrini, A. Ougazzaden, Cryst. Growth Des. 16, 3409 (2016).

[Li17] X. Li, M. B. Jordan, T. Ayari, S. Sundaram, Y. El Gmili, S. Alam, M. Alam, G. Patriarche, P. L. Voss, J. Paul Salvestrini, and A. Ougazzaden, Sci. Rep. 7, 786 (2017).

[Liu11] X. L. Liu, F. W. Qin, J. M. Bian, D. Zhang, W. J. Chen, Z. F. Zhou, A. B. Zhi, B. Yu, A. M. Wu, and X. Jiang, “Chinese Phys. Lett. 28, 108104, (2011).

[Liu18] H. Liu, J. Meng, X. Zhang, Y. Chen, Z. Yin, D. Wang, Y. Wang, J. You, M. Gao, and P. Jin, Nanoscale 10, 5559 (2018).

[Loc13] Z. Lochner, X.-H. Li, T.-T. Kao, M. M. Satter, H. J. Kim, S.-C. Shen, P. D. Yoder, J.-H. Ryou, R. D. Dupuis, K. Sun, Y. Wei, T. Li, A. Fischer, and F. A. Ponce, Phys. Status Solidi A 210(9), 1768 (2013).

[Lu07] T. Lu, T. Kao, C. Kao, J. Chu, K. Yeh, L. Lin, Y. Peng, H.-W. Huang, H.-C. Kuo, and S.C. Wang, IEEE Trans. Electron Device Lett., 28, 884 (2007).

[Maa02] P. Maaskant, M. Akhter, B. Roycroft, E. O. Carroll, and B. Corbett, Phys. Stat. Sol. (A), 192, 348 (2002).

[Mai18] A. Maity, S.J. Grenadier, J. Li, J.Y. Lin, H.X. Jiang, J. Appl. Phys. 123, 044501 (2018).

[Man71] H. M. Manasevit, F. M. Erdmann, W. I. Simpson, J. Electrochm. Soc. 118, 1864 (1971).

[Mar69] H. P. Maruska, J. J. Tietjen, Appl. Phys. Lett. 15, 327 (1969).

[Mat11] E. Matioli, C. Neufeld, M. Iza, S. Cruz, A. Al-Heji, X. Chen, R. Farrell, S. Keller, S. Denbaars, U. Mishra, S. Nakamura, J. Speck, and C. Weisbuch, Appl. Phys. Lett., 98, 021102, (2011).

[Mba21] A. Mballo, A. Srivastava, S. Sundaram, P, Vuong, S, Karrakchou, Y. Halfaya, S. Gautier, P. L. Voss, A. Ahaitouf, J. P. Salvestrini and Abdallah Ougazzaden, Nanomaterials, 11, 211(1–12) (2021).

[Mir89] A.Mircea, A.Ougazzaden, and R.Mellet,"Very uniform epitaxy,"*Progress in Crystal Growth and Characterization of Materials*, vol. 19, no. 1-2, pp. 39–49, 1989.

[Moh14] T. M. G. Mohiuddin, A. Lombardo, R. R. Nair, A. Bonetti, G. Savini, R. Jalil, N. Bonini, D. M. Basko, C. Galiotis, N. Marzari, K. S. Novoselov, A. K. Geim, and A. C. Ferrari, Phys. Rev. B 79, 205433 (2009).

[Mol99] R. Molnar, in "Gallium Nitride (GaN) II." Semiconductors and Semimetals (J. I. Pankove and T. D. Moustakas, Eds.), Vol. 57. Academic Press, New York, 1999.

[Mos87] Moss, S. J.; Ledwith, A. (1987). The Chemistry of the Semiconductor Industry. Springer. ISBN 978-0-216-92005-7.

[Mou13] T. Moudakir, F. Genty, M. Kunzer, P. Bo¨ rner, T. Passow, S. Suresh, G. Patriarche, K. Ko¨ hler, W. Pletschen, J. Wagner, A. Ougazzaden, IEEE Photonics Journal, 5, 8400709 (2013).

[Nad98] N. A. El-Masry, E. L. Piner, S. X Liu, and S. M Bedair. Appl. Phys. Lett., 72 40 (1998).

[Nak00] S. Nakamura, S. Pearton, and G. Fasol, The Blue Laser Diode: the Complete Story, Springer, (2000).

[Nak92] H. Amano, M. Kito, K. Hiramatsu, I. Akasaki, Jpn. J. Appl. Phys. 28, L2112 (1989)

[Nak93] S. Nakamura, T. Mukai, M. Senoh, S. Nagahama, N. Iwasa, J. Appl. Phys. 74, 3911 (1993)

[Nak94a] S. Nakamura, T. Mukai, and M. Senoh, Appl. Phys. Lett. 64, 1687 (1994)

[Nak94b] S. Nakamura, T. Mukai, and M. Senoh, J. Appl. Phys. 76, 8189 (1994)

[Nak97] S. Nakamura, M. Senoh, S. Nagahama, N. Iwasa, T. Yamada, T. Mukai, T. Matsushita, Y. Sugimoto, and H. Kiyoko, Appl. Phys. Lett. 70, 868 (1997)

[Nam04] K. B. Nam, J. Li, M. L. Nakarmi, J. Y. Lin, and H. X. Jiang, Appl. Phys. Lett. 84(25), 5264 (2004).

[Ors14] G. Orsal, Y. E. Gmili, N. Fressengeas, J. Streque, R. Djerboub, T. Moudakir, S. Sundaram, A. Ougazzaden, and J. P. Salvestrini, Opt. Mater. Express 4, 1030 (2014).

[Oug08] A. Ougazzaden, S. Gautier, T. Moudakir, Z. Djebbour, Z. Lochner, S. Choi, H. J. Kim, J.-H. Ryou, R. D. Dupuis, and A. A. Sirenko, Appl. Phys. Lett. 93, 083118 (2008).

[Pad16] Q. Paduano, M. Snure, D. Weyburne, A. Kiefer, G. Siegel, J.J. Hu, J. Cryst. Growth, 449, 148 (2016).

[Pan09] B. Pantha, A. Sedhain, J. Li, J. Lin, and H. Jiang, Appl. Phys. Lett., 95, 261904, (2009).

[Pan10] B. N. Pantha, A. Sedhain, J. Li, J. Y. Lin, and H. X. Jiang, "Achieving P-$In_X Ga_{1-X}$ N Alloys with High In Contents," in: Gallium nitride materials and devices V, (2010).

[Pan13] K. Pantzas, Y. El Gmili, J. Dickerson, S. Gautier, L. Largeau, O. Mauguin, G. Patriarche, S. Suresh, T. Moudakir, C. Bishop, A. Ahaitouf, T. Rivera, C. Tanguy, P.L. Voss, A. Ougazzaden 370, 57 (2013).

[Pan16] K. Pantzas, D.J. Rogers, P. Bove, V.E. Sandana, F.H. Teherani, Y. El Gmili, M. Molinari, G. Patriarche, L. Largeau, O. Mauguin, S. Suresh, P.L. Voss, M. Razeghi, A. Ougazzaden, Journal of Crystal Growth 435, 105 (2016).

[Pan71] J. I. Pankove, E. A. Miller, J. E. Berkeyheiser, RCA Rev. 32, 383 (1971).

[Pol15] I. Polyzos, M. Bianchi, L. Rizzi, E. N. Koukaras, J. Parthenios, K. Papagelis, R. Sordan, and C. Galiotis, Nanoscale 7, 13033 (2015).

[Puy17] R. Puybaret, D. J Rogers, Y. El Gmili, S. Sundaram, M. B Jordan, X. Li, G. Patriarche, F. H Teherani, E. V Sandana, P. Bove, P. L Voss, R. McClintock, M. Razeghi, I. Ferguson, J.P. Salvestrini and A. Ougazzaden, *Nanotechnology 28, 195304 (2017)*.

[Raj04] S. Rajan, P. Waltereit, C. Poblenz, S. J. Heikman, D. S. Green, J. S. Speck, and U. K. Mishra, IEEE Electron Dev. Lett. 25, 247 (2004).

[Rav12] V. Ravindran, Appl. Phys. Lett. 100, 243503 (2012).

[Rei05] S. Reich, A. C. Ferrari, R. Arenal, A. Loiseau, I. Bello, J. Robertson, Phys. Rev. B: Condens. Matter Mater. Phys., 71, 205201 (2005).

[Ryu13] H.-Y. Ryu, I.-G. Choi, H.-S. Choi, and J.-I. Shim, Appl. Phys. Express 6(6), 062101 (2013).

[Sas11] K. Sasamoto, T. Hotta, K. Sugita, A. G. Bhuiyan, A. Hashimoto, A. Yamamoto, K. Kinoshita, and Y. Kohji, Journal of Crystal Growth, vol. 318, 492, (2011).

[Sch92] E. F. Schubert, Y. H. Wang, A. Y. Cho, L. W. Tu, and G. J. Zydzik, Appl. Phys. Lett., 60, 921 (1992).

[Shi09] T. Shioda, M. Sugiyama, Y. Shimogaki, and Y. Nakano, Journal of Crystal Growth, 311, 2809 (2009).

[Shi18] J. Shim, S.-H. Bae, W. Kong, D. Lee, K. Qiao, D. Nezich, Y. J. Park, R. Zhao, S. Sundaram, X. Li, H. Yeon, C. Choi, H. Kum, R. Yue, G. Zhou, Y. Ou, K. Lee, J. Moodera, X. Zhao, J. Hyun, A. Ougazzaden, J. Kim. Science 362, 665 (2018).

[Sin97] R Singh, D Doppalapudi, TD Moustakas, and LT Romano. Appl. Phys. Lett., 70, 1089 (1997).

[Son00] Y. K. Song, M. Diagne, H. Zhou, A. V. Nurmikko, R. P. Schneider, and T. Takeuchi, Appl. Phys. Lett., 77, 1744 (2000).

[Son10] L. Song, L. Ci, H. Lu, P. B. Sorokin, C. Jin, J. Ni, A. G. Kvashnin, D. G. Kvashnin, J. Lou, B. I. Yakobson, P. M. Ajayan, Nano Lett., 10, 3209 (2010).

[Str99] G. B. Stringfellow, *Organometallic Vapor-Phase Epitaxy*. Academic Press, 1999.

[Sun14] S. Sundaram, R. Puybaret, Y. El Gmili, X. Li, P. L. Bonanno, K. Pantzas, G. Orsal, D. Troadec, Z.-H. Cai, G. Patriarche, P. L. Voss, J. P. Salvestrini, and A. Ougazzaden, J. Appl. Phys. 116, 163105 (2014)

[Sun15] S. Sundaram, Y. El Gmili, R. Puybaret, X. Li, P. L. Bonanno, K. Pantzas, G. Patriarche, P. L. Voss, J. P. Salvestrini, A.Ougazzaden, Appl. Phys. Lett., 107, 113105 (2015).

[Sun15b] S. Sundaram, R. Puybaret, X Li, Y. El Gmili, J. Streque, K. Panztas, G. Orsal, Gilles Patriarche, P. L. Voss, J. P. Salvestrini, A. Ougazzaden, Phys. Status Solidi A 212, No. 4, 740 (2015).

[Sun16] S. Sundaram, X. Li, Y. El Gmili, P. L. Bonanno, R. Puybaret, C. Pradalier, K. Pantzas, G. Patriarche, P. L. Voss, J. P. Salvestrini and A. Ougazzaden, Nanotechnology, 27, 115602 (2016).

[Sun19] S. Sundaram, X. Li, S. Alam, T. Ayari, Y. Halfaya, G. Patriarche, P. L. Voss, J. P. Salvestrini, A. Ougazzaden, *J. Cryst. Growth*, 507, 352 (2019).

[Sun19a] S. Sundaram, X. Li, S. Alam, Y. Halfaya, G. Patriarche, A. Ougazzaden, *J. Cryst. Growth*, 509, 40 (2019)

[Sun19b] S. Sundaram, X. Li, Y. Halfaya, T. Ayari, G. Patriarche, C. Bishop, S. Alam, S. Gautier, P. L. Voss, J. P. Salvestrini, and A. Ougazzaden, Adv. Mater. Interfaces 6, 1900207 (2019).

[Tay14] R. Y. Tay, M. H. Griep, G. Mallick, S. H. Tsang, R. S. Singh, T. Tumlin, E. H. T. Teo, and S. P. Karna, Nano Lett. 14, 839–846 (2014).

[Van18] S. Vangala, G. Siegel, T. Prusnick, M. Snure, Sci. Rep. 8, 8842 (2018).

[Vuo20] P. Vuong, A. Mballo, S. Sundaram, G. Patriarche, Y. Halfaya, S. Karrakchou, A. Srivastava, K. Krishnan, N. Y. Sama, T. Ayari, S. Gautier, P. L. Voss, J. P. Salvestrini, and A. Ougazzaden, Appl. Phys. Lett. 116, 042101 (2020).

[Vuo20a] P. Vuong, S. Sundaram, A. Mballo, G. Patriarche, S. Leone, F. Benkhelifa, S. Karrakchou, T. Moudakir, S. Gautier, P. L. Voss, J. P. Salvestrini, and A. Ougazzaden, ACS Applied Materials & Interfaces 12, 49, 55460 (2020).

[Vur01] I. Vurgaftman, J. R. Meyer, and L. R. Ram-Mohan, J. Appl. Phys. 89, 5815 (2001).

[Wan04] X. Wang, A. Yoshikawa / Progress in Crystal Growth andCharacterization of Materials 48/49 42e103 (2004).

[Wat03] S. Watanabe, T. Takano, K. Jinen, J. Yamamoto, and H. Kawanishi, Physica Status Solidi (c), 7, 2691, (2003).

[Xu15] Z. Xu, R. Zheng, A. Khanaki, Z. Zuo, J. Liu, Appl. Phys. Lett. 107, 213103 (2015).

[Yan18] X. Yang, S. Nitta, M. Pristovsek, Y. Liu, K. Nagamatsu, M. Kushimoto, Y. Honda, and H. Amano, Appl. Phys. Express 11, 051002 (2018).

[Yos75] S. Yoshida, S. Misawa, and A. Itoh, Appl. Phys. Lett. 26, 461 (1975).

[Yos83] S. Yoshida, S. Misawa, and S. Gonda, Appl. Phys. Lett. 42, 427 (1983).

[Yu09] H. Yu, A. Melton, O. Jani, B. Jampana, S. Wang, S. Gupta, J. Buchanan, W. Fenwick, and I. Ferguson, Photovoltaic Materials and Manufacturing Issues, 1123, 89 (2009).

[Zha18] X. Zhang, T. H. Choudhury, M. Chubarov, Y. Xiang, B. Jariwala, F. Zhang, N. Alem, G.-C. Wang, J. A. Robinson, and J. M. Redwing, Nano Lett. 18, 1049 (2018).

[Zhu12] W. Zhu, T. Low, V. Perebeinos, A. A. Bol, Y. Zhu, H. Yan, J. Tersoff, and P. Avouris, Nano Lett. 12, 3431 (2012).

[Zub00] D. Zubia, S. H. Zaidi, S. R. J. Brueck and S. D. Hersee, Appl. Phys. Lett. 76, 858 (2000).

[Zuo15] Z. Zuo, Z. Xu, R. Zheng, A. Khanaki, J.-G. Zheng, and J. Liu, Sci. Rep. 5, 14760 (2015).

Resume

I obtained my Master's in applied sciences with a specialization in materials science degree from the faculty of Engineering at PSG College of Technology, India, in 2004. Since my research debut in January 2005, my research activities have focused on challenging semiconductor materials for novel optoelectronic and/or photonic applications. I completed my doctoral thesis in November 2010 on the "Effect of V/III ratio and Irradiation induced defects on structural, optical and electrical characteristics of gallium nitride", under the guidance of Prof. K. Baskar, at the Crystal Growth Centre, Anna University. Then, until June 2015, I was a post-doctoral researcher at the UMI2958-GT-CNRS in the group of Prof. Abdallah Ougazzaden, where I came to continue my research on technologies related to the MOVPE growth of all III-nitride materials, devices and its nanostructures. I joined Georgia Tech Lorraine on 1st July 2015 as a Research Professor and Adjunct Professor in the School of Electrical and Computer Engineering, Georgia Institute of Technology, Atlanta, USA, to continue my research on III-nitrides. Currently, I am leading the MOVPE growth group. Our group is equipped with two state of the art MOVPE systems. A new high temperature capable CCS MOVPE system (total cost - 2 million euros, funded by SILSEF EUROPE) was installed, commissioned and demonstrated process under my supervision in 2014-2015. I have contributed successfully to 14 funded projects (with 3 ongoing ANR projects) and more than 20 doctoral theses. I have published more than 72 research articles in peer-reviewed journals with total citations above 1700 and h-index of 23. I have presented our research results in 11 invited talks and had over 30 oral presentations in the international conferences. I received the industry-sponsored speaker award at the 18th European Workshop on Metal-Organic Vapor Phase Epitaxy. Also, I have organized two international workshop and a symposium.